DEFECT BEHAVIOR IN CERAMICS AND SEMICONDUCTORS

By
Jun Young Kim

A dissertation submitted in partial fulfillment of
the requirements for the degree of

Doctor of Philosophy
(Electrical Engineering)

at the
University of Wisconsin–Madison
2022

Date of final oral examination: 04/20/2022

The dissertation is approved by the following members of the Final Oral Committee:
Izabela Szlufarska, Professor, Materials Science and Engineering
Luke Mawst, Professor, Electrical and Computer Engineering
Irena Knezevic, Professor, Electrical and Computer Engineering
Dane Morgan, Professor, Materials Science and Engineering

ABSTRACT

I study defect behavior in transition metal borides (TMBs) and transition metal dichalcogenides (TMDs) by means of density functional theory. TMBs have been studied mainly for extreme environment applications, and TMDs, especially their two-dimensional (2D) forms, have been considered for promising materials in next-generation semiconductor applications. Here, I discuss defect properties that must be considered for the proper operation of applications of TMBs and TMDs.

First, I study a new class of layered TMBs, called MAB phases, focusing on the stability of point defects and its impact on the defect recovery processes in two MAB phases: MoAlB and Fe_2AlB_2. Combined with experiments, I find that the defect recovery process in Fe_2AlB_2 is more efficient than in MoAlB, attributed to the stability of metal interstitials. Next, I investigate the structure-dependent defect recovery processes in Cr-based binary TMBs (CrB, Cr_3B_4, Cr_2B_3) and MAB phases (Cr_2AlB_2, Cr_3AlB_4, Cr_4AlB_6). I demonstrate that both the type of B networks and the Al layers have crucial impacts on the defect kinetics and the defect recovery processes. Lastly, I generalize the findings from the Mo-, Fe-, and Cr-based TMBs to TMBs with different transition metals and develop design rules for TMBs with efficient defect recovery processes.

For TMDs, I combine state-of-the-art computational approaches with experiments to determine the formation energies and the charge-state transition levels (CTLs) of defects in bulk and 2D TMDs (MoS_2, $MoSe_2$, $MoTe_2$, WS_2, WSe_2, WTe_2). I calculate the formation energies and the CTLs of native point defects in bulk TMDs, resulting in good agreement with our experimental CTLs measured by deep level transient spectroscopy (DLTS). The good agreement allows the identification of the nature of the CTLs observed in DLTS, while validating the computational approach. I apply the validated method to determine the CTLs in 2D TMDs, for which DLTS is very challenging. By comparing the CTLs in bulk and 2D TMDs, I find that the reduction of the dimensionality from bulk to 2D has a significant impact on the defect properties.

TABLE OF CONTENTS

LIST OF FIGURES

LIST OF TABLES

ACKNOWLEDGEMENTS

I am genuinely grateful to my research advisor Prof. Izabela Szlufarska for all the lessons and continual support during my PhD studies. I am thankful that she provided me with the freedom to pursue my ideas and the opportunities to contribute to the projects. I would like to thank my academic advisor Prof. Luke Mawst for motivating me to achieve academic success in the diverse fields of study. I would like to extend my gratitude to Prof. Dane Morgan and Prof. Irena Knezevic for being on my dissertation committee and providing many invaluable insights.

I would also like to express my gratitude to my parents Jong Sung Kim and Mikyung Seo, my sister Jin Young Kim, and all my friends both in Madison and South Korea for their continuous support.

CHAPTER 1

INTRODUCTION

1.1 Defects in materials

Mankind has developed capitalizing largely on the discovery and development of new materials. The production of iron tools helped the farming process easier and more efficient during the Iron Age, and the use of silicon in electronics accelerated the information technologies. The benefits of materials are attributed to materials' unique properties, which are determined by the atomic structure of materials. A periodic arrangement of nuclei establishes a periodic potential wherein the electrons form a unique band structure, which determines the physical, chemical, and electrical properties of the material. This ordered arrangement of atoms, called crystal structure, almost always contains interruption in its periodic pattern, and thus the material properties are deformed. Here, interruption in a crystal structure is called crystallographic defect, or shortly, defect.

Different types of defects are classified into point defects (0-dimensional (0D)), line defects (1D), planar defects (2D), and bulk defects (3D). First, point defects are lattice flaws that occur only at or near a single lattice point, and they include vacancy, interstitial, and antisite. Line defects are mainly dislocations, around which the atoms of the crystal structure are misaligned. Planar defects include stacking faults and grain boundaries where the orientation of the crystal structure abruptly changes. Bulk defects include voids, precipitates, and macroscopic defects such as pores and cracks.

Defects are everywhere and affect materials properties in various manners. First, there is always a chance that a lattice site is unoccupied by an atom at a finite temperature, and the likelihood increases with temperature. Besides defects naturally formed, defects can be often created unwantedly. For example, defect creation is significant in the materials for nuclear reactors. Reactor materials are exposed to radiation damage by high energy radiative particles such as ions and neutrons. At the initial stage of

radiation, the material undergoes radiation-induced displacement cascades, which involve the production and accumulation of a considerable amount of point defects, especially Frenkel pairs. Then, these point defects can be recovered through migration and recombination of mobile defects, or they can also interact with each other and evolve as clusters such as dislocation or precipitates. The accumulation of defects causes mechanical deformation and strength weakening, and if not well addressed, the material loses its stability and is amorphized. Defects have considerable effects on the performance of semiconductor devices as well. During semiconductor fabrication processes, unwanted defects can form, so annealing steps are often performed in order to recover the unwanted defects. In semiconductors, even a point defect can create multiple charge states inside the bandgap. The transitions between charge states, referred to as charge-state transition level (CTL), act as electron traps that diminish the carrier mobilities and thus the performance of electronic devices, or cause non-radiative emission in photonic devices. Lastly, defects can be also deliberately introduced. During semiconductor fabrication processes, ions can be deliberately implanted into a target crystal, thereby becoming impurities and altering the electronic properties as intended. Given considerable effects of defects on the properties of materials and the performance of applications, understanding defect behavior is critical for the proper operation of applications and the design of novel materials.

In this dissertation, I discuss defect behavior in two types of layered materials, focusing on the defect recovery processes in ceramics and the electronic properties of defects in semiconductors.

1.2 Layered materials

Layered materials are crystal solids with anisotropic bonding, wherein 2D layers are strongly bonded internally but weakly bonded to adjacent layers[1]. Due to their distinctive structures, layered materials have many interesting properties and thus have been studied in diverse fields of materials research, including ultra-high temperature ceramics (UHTCs) and semiconductors. My focus lies on two types of layered materials: transition metal borides (TMBs)[2,3] and transition metal dichalcogenides (TMDs)[4–6].

1.2.1 Transition metal borides

TMB can be classified as a sub-group of UHTC[7], a class of refractory materials that possess outstanding properties at high temperature[8–12], and its applications include high-temperature crucibles, wear resistance coating, and aerospace materials[2]. Although many binary TMBs[13–21] have been widely studied along with the other types of UHTCs such as carbides[22,23], nitrides[24,25], and oxides[26,27], it is recent that layered ternary TMBs, called MAB phases[27], began to draw attention. Prior to discussion about MAB phases, it is worth introducing MAX phases, ternary layered carbides and nitrides that attracted attention first[28]. The general formula of MAX phases is $M_{n+1}AX_n$ (M = transition metal; A = group A element; X = C or N), and they consist of strongly bonded M-X units and A layers interleaving the M-X layers, wherein the M-X layers and the A layers are weakly bonded. MAX phases exhibit good properties[29–33] including excellent resistance to radiation-induced amorphization[34]. It has been suggested that the extraordinary resistance to radiation-induced amorphization of MAX phases is attributed to the A layers, where defect recovery processes are efficient[35,36]. MAB phases[27], the new type of layered ternary TMBs, have attracted great attention more recently, owing to the structural similarity to MAX phases as well as outstanding properties, including electrocatalytic properties[37,38], oxidation resistance[13,39–42], magnetic properties[43–47], hardness[27,41,48–52], and thermal and electrical conductivities[41,53–61]. MAB phases with different formulas have been reported, including $M_1A_1B_1$, $M_2A_1B_2$, $M_3A_2B_2$, $M_3A_1B_4$, and $M_4A_1B_6$ (M = transition metal; A = mostly Al; B = B)[62], wherein the A layers interleave the M-B layers and the transition metals are bonded to different types of B networks depending on the composition. Despite the outstanding properties and extensive studies on MAB phases[63–70], defect properties have been rarely studied in MAB phases. In this dissertation, I study defect behavior in TMBs, focusing on structure-dependent defect properties in MAB phases. The structural diversity with the different types of B networks and the different numbers of A layers enables to study structural effects on the defect behavior in TMBs. Throughout this dissertation, I discuss the stability, chemistry, kinetics and recovery processes of defects, in the context of applications that require efficient defect recovery processes, by means of density functional theory (DFT). I study the stability of defects in Mo- and Fe-based MAB phases in

Chapter 3 and investigate the defect chemistry and the recovery processes in Cr-B binary TMBs and Cr-Al-B MAB phases in Chapter 4 and Chapter 5. Based on the findings from the Mo-, Fe-, and Cr-based TMBs, in Chapter 6, I develop design rules for TMBs with efficient defect recovery processes.

1.2.2 Transition metal dichalcogenides

Since the successful synthesis of graphene[71], many other layered materials and their 2D forms have been widely studied, especially for semiconductor applications. TMD is one of the well-known layered materials in semiconductor applications along with graphene[71], hexagonal boron nitride[72], MXenes[73] and MBenes[74,75] (2D forms of MAX and MAB phases with the A layers intercalated, respectively). The general formula of TMDs is MX_2 (M = transition metal; X = S, Se, or Te), wherein one layer of M atoms is sandwiched between two layers of X atoms, and for bulk MX_2 the M-X layers are bonded to one another by van der Waals (vdW) interaction. Like graphene, TMDs exhibit new physical properties when a bulk crystal of macroscopic dimension is thinned down to a 2D crystal[76]. In particular, the indirect bandgaps of some bulk TMDs are transitioned to the direct bandgaps when the bulk TMDs are thinned down to 2D TMDs[76], which makes 2D TMDs promising in diverse semiconductor applications[12,77–82], including transistors in electronics and emitter and detectors in photonics[76,79,81]. In addition, their 2D structure makes them more promising in novel applications such as flexible devices and vdW heterostructures[83]. Due to the excellent properties and wide ranges of applications, recent efforts have been focused more on 2D TMDs. However, despite the considerable effects of defects on the performance of TMD-based devices[84,85], it has been challenging to accurately determine relevant defect properties, particularly CTLs in 2D TMDs. It is nearly impossible to measure the CLTs of defects in 2D crystals using such a direct measurement system as deep level transient spectroscopy (DLTS). Moreover, although theoretical CTLs have been reported[86–88], there have been discrepancies in the reported values, and in many cases the predictions have not been validated experimentally. In Chapter 7, I develop a joint computational and experimental strategy to accurately determine the CTLs in 2D systems and discuss the effects of the reduction in dimensionality (i.e., bulk to 2D) on the CTLs in TMDs.

CHAPTER 2

METHODS

2.1 Density functional theory

Material properties originate from its atomic structure, the arrangement of nuclei and their electrons sitting on the potential of the nuclei. Such a system at the scale of atoms and subatomic particles has to be described by quantum mechanics. The probability of finding a particle at a given space ($\boldsymbol{r}$) and a given time (t) can be expressed as a wave function, $\Psi(\boldsymbol{r}, t)$, which can be obtained by solving the Schrödinger equation,

$$i\hbar\frac{\partial\Psi}{\partial t} = H\Psi \tag{2.1}$$

where H is the Hamiltonian of the quantum system. This time-dependent form can be reduced to the non-relativistic time-independent Schrödinger equation (2.2),

$$H\psi = E\psi \tag{2.2}$$

where E is the total energy of the system, and the wave function is now independent of time, $\psi = \psi(\boldsymbol{r})$.

Studying properties of a material requires all the nuclei and electrons in the material to be taken into account. Therefore, one has to solve the Schrödinger equation for a wave function that is a function of the positions of all the nuclei ($\{\boldsymbol{R}_i\}$) and of all the electrons ($\{\boldsymbol{r}_i\}$), i.e., $\psi = \psi(\{\boldsymbol{R}_i\}, \{\boldsymbol{r}_i\})$. Since it is impractical to solve such a complex system, approximations are introduced. First, the Born-Oppenheimer approximation[89] assumes that nuclei are much heavier than the electrons, and hence the dynamics of nuclei and electrons can be separated, resulting in a decoupled wavefunction, $\psi = \psi_N(\{\boldsymbol{R}_i\})\psi_e(\{\boldsymbol{r}_i\})$. Now, one can solve the Schrödinger equation for electrons separately,

$$\left[-\frac{\hbar^2}{2m_e}\sum_i^{N_e}\nabla_i^2 + \sum_i^{N_e}V(\boldsymbol{r}_i) + \sum_i^{N_e}\sum_{j>i}U(\boldsymbol{r}_i, \boldsymbol{r}_j)\right]\psi_e = E\psi_e \tag{2.3}$$

where V is the potential energy of electrons, and U is the interaction between electrons. Once the wavefunction and the energy eigenvalues are obtained, the forces on atoms can be calculated, and then classical dynamics can be applied to calculate the dynamics of atoms.

However, it is still impractical to solve many-body problems. For instance, the Hartree-Fock method, one of the well-known traditional ways, produces a reasonable description of many body quantum systems[90,91], but its use has been limited. In particular, the Hartree-Fock method does not deal with electron correlations, resulting in poor accuracy for such calculations as dissociation energies or reaction energies[92]. Moreover, the Hartree-Fock and other methods that deal with electron correlations, such as perturbation theory (e.g., MP2)[93], suffer from computational costs[94]. This issue is especially considerable in systems that contain transition metals, because the number of electrons in transition metals further increases the computational cost, which exponentially increases with the size of system.

Density functional theory (DFT) has been successfully used in computational physics, providing satisfactory results at relatively inexpensive computational costs. The main idea of DFT is to describe a many-body quantum system with its particle density rather than the wavefunctions of all the particles. Hence, the degree of freedom of a *N*-body system (3*N*) is reduced to the three-dimension of its particle density. In DFT, instead of wavefunctions, the electron density, $n(\boldsymbol{r})$, describes the system as follows,

$$n(\boldsymbol{r}) = \psi_e^*(\{\boldsymbol{r}_i\})\psi_e(\{\boldsymbol{r}_j\}) = 2\sum_i \psi_e^*(\{\boldsymbol{r}_i\})\psi_e(\{\boldsymbol{r}_i\}). \quad (2.4)$$

In DFT, the *j*-th electron is considered to be in the density of all the other electrons, which simplifies a "many-electron" problem into many non-interacting "one-electron" problems. Here, the electron wavefunction is defined as $\psi_e = \psi_1(\boldsymbol{r}_1)\psi_2(\boldsymbol{r}_2)\ldots\psi_{Ne}(\boldsymbol{r}_{Ne})$, called Hartree product, where $\psi_{\boldsymbol{k}}$ represents the one electron wavefunction, $\psi_{\boldsymbol{k}}(\boldsymbol{r}) = \sum_{\boldsymbol{G}} c_{\boldsymbol{k}+\boldsymbol{G}} \exp(i(\boldsymbol{k}+\boldsymbol{G})\cdot\boldsymbol{r})$. Next, the total energy of a system can be also expressed as a function of electron density. The Hohenberg-Kohn theorems[95] state that the total energy is a unique functional of the electron density (Theorem 1) and that the electron density that minimizes the energy functional is the true ground state electron density (Theorem 2). The electron energy functional can be expressed as,

$$E[\{\psi_i\}] = -\frac{\hbar^2}{2m_e}\sum_i \int \psi_i^* \nabla^2 \psi_i d\boldsymbol{r} + \int V(\boldsymbol{r}) n(\boldsymbol{r}) d\boldsymbol{r} + \frac{e^2}{2}\int\int \frac{n(\boldsymbol{r}) n(\boldsymbol{r}')}{|\boldsymbol{r}-\boldsymbol{r}'|} d\boldsymbol{r} d\boldsymbol{r}' + E_{\mathrm{XC}}[\{\psi_i\}] \quad (2.5)$$

where E_{XC} is the exchange-correlation functional, which will be discussed in detail in the following section.

Now, in order to solve non-interacting single-electron problems, the non-interacting Schrödinger equation, called Kohn-Sham (KS) equation[96], is devised as follows,

$$\left[-\frac{\hbar^2}{2m_e}\nabla^2 + V_{\mathrm{eff}}(\boldsymbol{r})\right]\psi_i(\boldsymbol{r}) = E_i \psi_i(\boldsymbol{r}) \quad (2.6)$$

where V_{eff} is the KS potential and can be expressed as,

$$V_{\mathrm{eff}} = V(\boldsymbol{r}) + e^2 \int \frac{n(\boldsymbol{r}')}{|\boldsymbol{r}-\boldsymbol{r}'|} d\boldsymbol{r}' + V_{\mathrm{XC}}(\boldsymbol{r}). \quad (2.7)$$

Here, the second term is called the Hartree potential, which describes the interaction of the electron with the electron density, and the last term, V_{XC}, is the exchange-correlation potential defined as $\delta E_{\mathrm{XC}}(n)/\delta n(\boldsymbol{r})$.

Now, the original "many-electron" problem can be expressed as a set of "one-electron" problems. Starting from a trial electron density, the KS equations for each electron can be iteratively solved in a self-consistent scheme to find the ground state energy and the electron density that minimizes the energy functional. When the true electron density, i.e., ground state, is found, the dynamics of nuclei can be classically solved, by calculating the forces acting on the nuclei. By moving atoms along the ionic forces, the ionic ground state can be finally calculated along with the electron ground state.

2.2 Exchange correlation functional

In order to solve the KS equation, the exchange-correlation functional, E_{XC}, must be specified. Although the exact form of E_{XC} is unknown (except for homogeneous electron gas), approximations can be made. The simplest approximation is the local density approximation (LDA)[97,98], where the functional depends only on the local density and is approximated by the exchange-correlation energy of the

homogeneous electron gas density at a given point. The other simple and effective approximation is generalized gradient approximation (GGA)[97,98], where the functional is approximated using the information about the local electron density and the local gradient in the electron density. There are a number of GGA functionals, which differ by the way how the information about the local gradient is included, and Perdew–Burke–Ernzerhof[99] is one of the most widely used functionals.

Although the conventional LDA and GGAs have been effectively used in many fields of computational physics, they do not always describe systems satisfactorily. The conventional functionals cannot describe dispersion interactions, namely van der Waals (vdw) interactions. Without including the contribution of vdW interactions to the intermolecular forces in materials, considerable errors are made when predicting crystal structures and the properties of materials[100]. vdW interactions arise directly as a consequence of electron correlation, and one simple solution is to add a dispersion-like contribution to the total energy (e.g., DFT-D)[101]. In DFT-D, the total energy of a system can be defined as,

$$E_{\mathrm{DFT-D}} = E_{\mathrm{DFT}} - S\sum_{i\neq j}\frac{C_{ij}}{r_{ij}^{6}} f_{\mathrm{damp}}(r_{ij}) \tag{2.8}$$

where E_{DFT} is the total energy calculated in DFT, and the second term is the vdW contribution. Here, S is an empirical scaling factor applied uniformly to all pairs of atoms, r_{ij} is the distance between atoms, C_{ij} is the dispersion coefficient for atoms *i* and *j*, and f is a damping function to remove unphysical dispersion terms for small distances[92]. There are many DFT-D functionals[101–103], which differ by how the damping function and/or the dispersion coefficient are included.

The other solution to describe vdW interactions is non-local functionals. vdW interactions are long-range, and conventional LDA or GGAs, which rely on the local density, cannot describe the long-range electron correlation. Thus, long-range non-local functionals in which vdW interactions are included as a density-density interaction term have been developed. Depending on how the correlation term is optimized, many non-local vdW functionals have been proposed[104,105]. Among different non-local functionals, rev-vdW-DF2[106] is known for the accuracy in describing layered vdW solids, including TMDs[104].

The other important limitation of DFT is significant underestimation of bandgaps that stem from inaccurate band structures[107]. This issue has been effectively addressed by combining a conventional functional with the Hartree-Fock method in which the calculated bandgap is overestimated. Because the systematic errors of DFT and the Hartree-Fock method are in the opposite (i.e., underestimation vs. overestimation), the accurate bandgaps of semiconductors can be hybridly calculated by mixing a fraction of the Hartree-Fock exchange with DFT. This way, hybrid functionals provide electronic structures that well describe experiments[108]. Therefore, in studies where accurate bandgaps are desired, such as electronic properties of defects, hybrid functionals are used. In this dissertation, a hybrid functional called Heyd, Scuseria, and Ernzerhof[99] (HSE) is used to calculate the band structures of semiconductors. In HSE, a fraction of the conventional functional (e.g., GGA) is replaced by a short range Hartree-Fock exchange[109], and the HSE functional $E_{\mathrm{XC}}^{\mathrm{HSE}}$ can be described as,

$$E_{\mathrm{XC}}^{\mathrm{HSE}} = E_{\mathrm{XC}}^{\mathrm{GGA}} + a\left(E_{\mathrm{X}}^{\mathrm{HF}} - E_{\mathrm{XC}}^{\mathrm{GGA}}\right) \tag{2.9}$$

where $E_{\mathrm{XC}}^{\mathrm{GGA}}$ is the GGA exchange functional, $E_{\mathrm{X}}^{\mathrm{HF}}$ is the Hartree-Fock exchange, and a is the fraction of the Hartree-Fock exchange[99].

2.3 Vienna Ab-initio Simulation Package

In my studies, the Vienna Ab-initio Simulation Package (VASP) is used to perform DFT calculations[110]. VASP is a planewave-based DFT code for atomic scale materials modelling, from first principles, and it supports hybrid functionals that combine DFT and Hartree-Fock as well. In order to run a DFT calculation, four input files are required: POSCAR, POTCAR, KPOINTS, and INCAR. POSCAR contains information about the size and the geometry of the unitcell/supercell, the type of chemical element(s), and the position of each atom in the cell. POTCAR contains the pseudopotentials for each type of chemical element(s) specified in POSCAR. KPOINS defines the size of the *k*-point mesh and the number of total *k*-points in the Brillouin zone. INCAR contains specific settings for a DFT calculation,

including the fraction of the Hartree-Fock exchange (for hybrid calculations) and the parameters for DFT-D or non-local functionals, if applied.

2.4 Nudged elastic band method

Understanding materials properties often requires kinetic quantities such as migration energies or reaction energy barriers. In order to calculate such kinetic quantities, the transition states between the initial and the final states (i.e., reactant and product) must be defined along with their energy landscape. The transition states lie on the energy saddle points, and therefore define the minimum energy path (MEP) between the two end points. While initial and final states can be obtained by performing DFT calculations, finding the transition states and the MEP requires extra steps, for which one of widely used methods is nudged elastic band (NEB). In NEB, several intermediate atomic images between the two end points are initially defined, wherein the images are considered to be connected by fictitious springs. The images are optimized by minimizing the energy of all the images by concurrently performing a set of independent DFT calculations. During the optimization, the transition states are found by iteratively calculating $F = -\nabla E(\boldsymbol{r})$, the forces of the images defined by the energy surface, until the forces are aligned with the MEP. In the meantime, the elastic energy from the fictitious springs is minimized in order to keep the spacings between the images as equal as possible. The accuracy of the NEB method can be improved by climbing up the highest energy image to the exact saddle point. In this scheme, called climbing image NEB (CI-NEB)[111], the image does not feel the spring forces along the path, instead the image tries to maximize its energy along the path (i.e., locate itself on the exact saddle point), wherein the inverted tangent component of the true force drives up the image. In my research, the CI-NEB method was used.

CHAPTER 3

DEFECT STABILITY

The study in this chapter has been published as: "Defect behavior and radiation tolerance of MAB phases (MoAlB and Fe_2AlB_2) with comparison to MAX phases" *Acta Materialia* 196, 505–515 (2020), and the experimental part in this chapter was carried out by Dr. Hongliang Zhang.

3.1 Introduction

Layered ternary materials[27,28,112] are known for many outstanding properties, including thermal shock resistance[113,114], oxidation resistance[39,115], hardness, strength, and radiation resistance[34,116]. Radiation resistance have been studied primarily in MAX phases (M = transition metal; A = group A element in the periodic table; X = C or N), which in some cases can maintain their crystalline structures up to a very high radiation dose[34,116]. For instance, $Ti_3(Si/Al)C_2$ was shown to resist radiation-induced amorphization up to 25 displacements per atom (dpa) at room temperature (RT). Radiation resistance arises from the ability of the material to efficiently anneal non-equilibrium defects introduced during the bombardment of the lattice with neutrons, ions or electrons. Although it is generally agreed upon that the layered structure of MAX phases plays an important role in the defect recovery processes, specific mechanisms are still being debated[35,117,118]. It has been proposed that the radiation tolerance of MAX phases could be correlated with the radiation tolerance of M-X binary, M-A bonding characteristics, A/MX layer ratio, or low antisite formation energy. The question of whether low antisite formation energy is advantageous is particularly interesting. Specifically, while antisites provide an alternative pathway for accommodating defects, they can also lead to undesirable phase transformation, as in the case for $Ti_3(Si/Al)C_2$, which transforms from a hexagonal structure to a cubic structure during the irradiation at RT[119]. Moreover, radiation has been shown to lead to surface cracks in many MAX phases, such as

Ti_2AlC and Ti_3AlC_2, even at high temperatures[116]. The aforementioned radiation-induced phase transformation and microcracking may limit the applications of MAX phases in nuclear reactors.

In this chapter, we consider another class of layered ternary materials labeled as MAB (M = transition metal; A = Al; B = B) phases. Many MAB phases have been predicted theoretically[62] and some of them have already been synthesized (M = Mo, W, Cr, Mn, Fe, and Ru)[27]. In this chapter, we focus on two MAB phases: MoAlB and Fe_2AlB_2. A schematic view of the atomic structures of the two phases is shown in Fig. 3.1. MoAlB is orthorhombic with the space group of *Cmcm*, and Fe_2AlB_2 is orthorhombic with the space group of *Cmmm*. Similarly to the layered structure of MAX phases, MAB phases have transition metal boride sublattices interleaved by Al layers. MoAlB has been shown to have good oxidation resistance thanks to the formation of a protective layer of Al_2O_3[39], and Fe_2AlB_2 has been shown to be resistant to cracking[120] and to have a magnetocaloric effect with the ordering temperature of 307 K[43]. Moreover, MoAlB and Fe_2AlB_2 have the high decomposition temperatures of 1708 K[60] and 1500 K[114], respectively.

Borides have been already considered for applications that involve radiation, such as neutron shielding in both fusion and fission reactors[121,122] and neutron absorbers (e.g., as absorbers of thermal neutrons for long-term and compacted storage of spent nuclear fuel)[123]. In order to explore the potential of MAB phases for use in radiation environments, in this chapter we performed irradiation of the two MAB phases at RT and 300 °C, and the radiation effects were analyzed using transmission electron microscopy (TEM). The trends are explained based on density functional theory (DFT) calculations of defect formation, reaction, and migration energies. The performance of MAB phases under the radiation is compared to that of MAX phases as well as SiC, which is known to have good radiation resistance and is already being considered for cladding applications in nuclear reactor applications. The two MAX phases used for the comparison are: Ti_2AlC (which contains Al, just like the MAB phases considered in this chapter) and Ti_3SiC_2 (which so far has shown the highest resistance to radiation-induced amorphization among MAX phases).

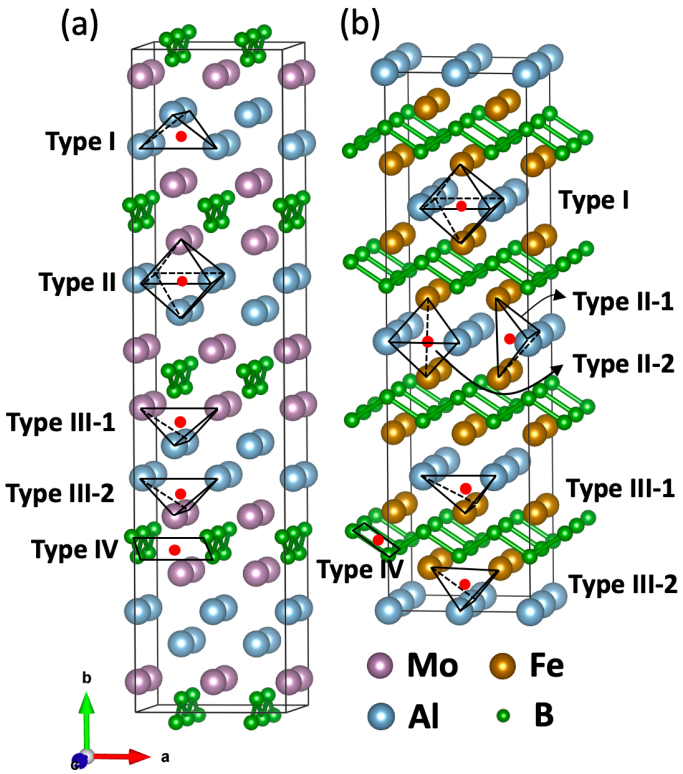

Figure 3.1 Schematic view of a supercell (2×2×2) for (a) MoAlB and (b) Fe_2AlB_2. Different interstitial sites are indicated as red dots.

3.2 Methods

The materials studied in this chapter were polycrystalline bulk Fe_2AlB_2, MoAlB, Ti_3SiC_2 and Ti_2AlC, prepared by reactive hot press sintering. The polycrystalline 3C-SiC for this research was purchased from Rohm and Haas Company and it had an average grain size of 5 μm.

The Fe_2AlB_2 sample was made from Fe_2AlB_2 powder (particle sizes of <45 μm) synthesized in a tube furnace (MTI GSL-1800X-S60). The powder was placed in a 12.7 mm inner diameter graphite die, lined with a graphite foil, and pressed at a maximum temperature and a pressure of 1200 °C and 50 MPa in a hot-press furnace (MTI OTF-1500X-VHP4 containing a mullite tube) under flowing argon to prevent oxidation. The sample was held at the maximum temperature and pressure for 30 min, using a heating and cooling rate of 10 °C/min. The sample was ground using a SiC paper to remove graphite from the surface and resulted in a pellet of 11 mm tall and 12 mm in diameter. The density of the sample determined by Archimedes principle was >95% of theoretical density.

The MoAlB sample was synthesized using MoB powder (particle sizes of <45 μm) and Al powder (>99.7%, particle sizes of <45 μm). The MoB powder was mixed with the Al powder in an atomic ratio of 1:1.3 (MoB:Al). The mixed powder was placed in a 15 mm inner diameter graphite die, lined with graphite foil, and pressed at a maximum temperature and a pressure of 1400 °C and 50 MPa in the hot-press furnace (MTI OTF-1500X-VHP4 containing a mullite tube) under flowing argon to prevent oxidation. The sample was held at the maximum temperature for 1 hour, using a heating and cooling rate of 10 °C/min. The sample was ground using a SiC paper to remove graphite from the surface and resulted in a pellet with the theoretical density of 95.5%, determined by Archimedes principle. The sample was sliced into ~1.5mm thick disks using a diamond blade.

Polycrystalline bulk Ti_2AlC and Ti_3SiC_2 were synthesized by the reactive hot-press sintering method[124]. For Ti_2AlC, stoichiometric mixtures of Ti + TiAl + C were prepared in argon by hand-grinding a fine powder mixture of Ti (99.5 %, average particle size of 48 μm), Al (99.0 % , average particle size of 48 μm), TiC (99.0 %, average particle size of 5 μm) and C graphite (99.5 %, average particle size of 48 μm) at a molar ratio of 0.5:1.5:1:0.5. The powder mixture was loaded into a cylindrical die and sintered via hot pressing under flowing argon gas, by heating to 1400 °C at 10 °C/min and holding at the temperature for 1 hour with an applied pressure of 35 MPa. For Ti_3SiC_2, stoichiometric mixtures of 3Ti + SiC + C were prepared by hand-grinding a fine powder mixture of Ti (99.9%), SiC (99.9%), and C (graphite, 99.99%) under argon, followed by cold pressing in a hardened steel die at 180 MPa. The powders contained ~2 wt.% Al to assist with reactivity. The pressed cylindrical samples were sintered under flowing argon gas by heating to 1600 °C at 10°C/min, holding for 4 hours, and returning to RT. During the sintering, a small amount of Al_2O_3 was formed in the sample.

The as-sintered specimens and the purchased CVD SiC were all characterized using X-ray diffraction (XRD) analysis (Rigaku D/max 2500, Cu Kα source with the wavelength of 0.154 nm, the step size of 0.02°, 1.0 sec per step, and a 2-theta range of 20-80º). As shown in Fig. 3.2, no impurity phase was found in Fe_2AlB_2, MoAlB, Ti_2AlC, or SiC, whereas a small amount of Al_2O_3 (<2% wt.%) was found in Ti_3SiC_2. All specimens were polished using fine metallographic abrasive papers and Al_2O_3

suspensions, cleaned by rinsing in ultrasonic baths of acetone and ethanol and annealed at 600 °C in a vacuum environment of 5 $\times 10^{-5}$ Pa for 1 hour to release the residual stress.

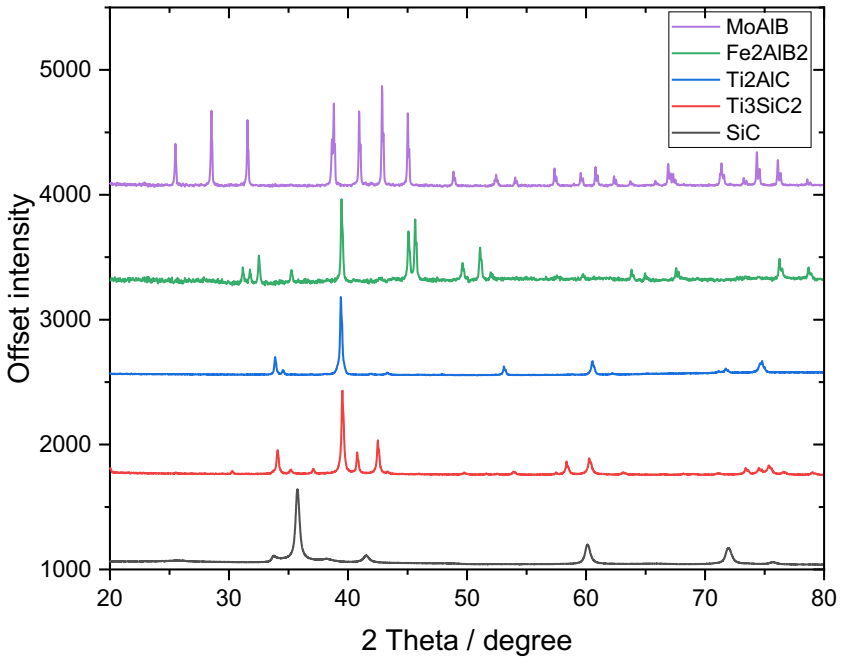

Figure 3.2 XRD spectra of the unirradiated MoAlB, Fe_2AlB_2, Ti_2AlC, Ti_3SiC_2, and SiC.

The final bulk samples of Fe_2AlB_2, MoAlB, Ti_2AlC, Ti_3SiC_2 and CVD SiC bulk were irradiated with a 3.15 MeV carbon ion beam incident at 0° to the normal using the tandem accelerator at the Ion Beam Lab in the Department of Engineering Physics, University of Wisconsin-Madison. The irradiation was performed at RT and 300 °C. Here, the RT corresponds to the sample temperature of about 150 °C due to the heating effects of the ion implantation. The typical irradiation flux was kept at ~7.0×10^{11} ions·cm^{-2}·s^{-2}. The irradiation fluence delivered to the samples was 1.5×10^{17} ions·cm^{-2} for the high dose case and 7.5 $\times10^{16}$ ions·cm^{-2} for the low dose case. The background pressure during the irradiation was <5×10^{-4} Pa. The total damage, measured in dpa, was simulated using SRIM-2013[125]. The displacement energies were 25 eV, 25 eV, and 28 eV, respectively for Fe, Al, and B in Fe_2AlB_2; 25 eV, 25 eV, and 28 eV, respectively for Mo, Al, and B in MoAlB; 25 eV, 15 eV and 28 eV, respectively for Ti, Al, and C in

Ti_2AlC; 25 eV, 15 eV, and 28 eV, respectively for Ti, Si, and C in Ti_3SiC_2; and 15 eV for both Si and C in SiC. The damage levels obtained from the SRIM-2013 simulation were estimated to be 1.0 dpa at the surface, rising up to ~23 dpa for Fe_2AlB_2 and MoAlB at the depth of ~1800 nm, ~26 dpa for Ti_2AlC, ~28 dpa for Ti_3SiC_2 and ~30 dpa for SiC at the depth of 2200 nm (see Fig. 3.3). The experimental ranges for the irradiation obtained from the TEM images were 2.2 μm for Fe_2AlB_2 and MoAlB, 2.4 μm for Ti_3SiC_2, and 2.6 μm for Ti_2AlC and CVD SiC.

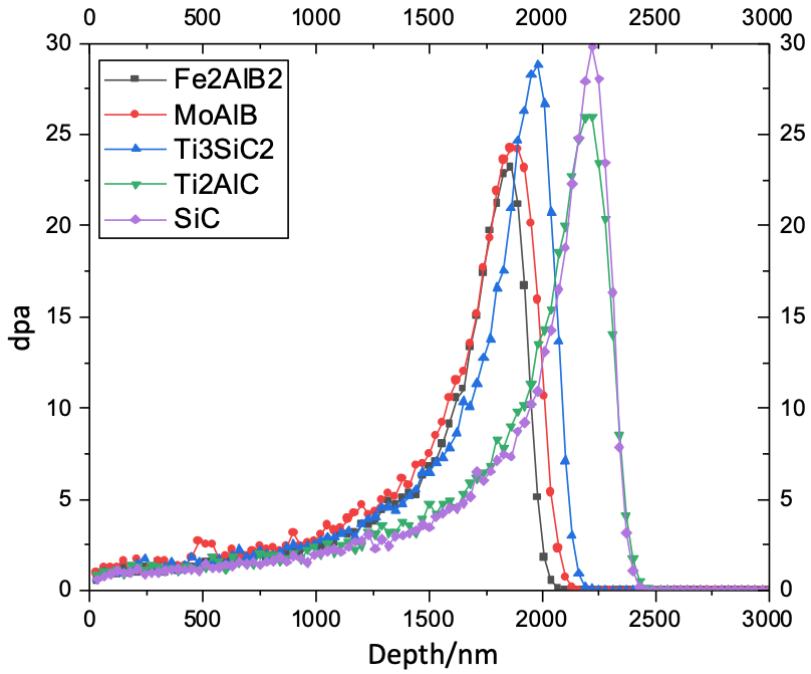

Figure 3.3 Depth profiles of dpa for Fe_2AlB_2, MoAlB, Ti_2AlC, Ti_3SiC_2 and SiC at the fluence of 1.5×10^{17} ions·cm^{-2}.

Scanning electron microscopy (SEM) images and samples for TEM analysis were obtained using standard lift-out techniques by FEI Helios PFIB G4 FIB/FESEM Focused Ion Beam (FIB) instrument in the Materials Science Center at the University of Wisconsin-Madison[126]. To protect the sample surfaces from damages during the FIB preparation, a 3.0 μm Pt protective layer was deposited on the surface of the indented region by two steps: (i) a low-energy electron beam (2 kV) was used to deposit a 1.0 μm Pt layer to avoid damages from high-energy ion deposition; (ii) an ion beam (12 kV) was used for the

deposition of another 2.0 μm Pt layer. The thinning process was accelerated using a high-energy ion beam (30 kV) at the beginning and a low-energy ion beam (2 kV) at the end to carefully remove the amorphous area generated in the former stage. FEI Tecnai F30 with a field emission gun (FEG) TEM and a high resolution TEM were used to analyze the damage and microstructural changes before and after thee irradiation.

DFT calculations were performed using the Vienna Ab-initio Simulation Package[110] with the projector augmented wave[127] and the generalized gradient approximation by Perdew, Burke and Ernzerhof[99]. The plane-wave cutoff energy of 400 eV and Monkhorst-Pack *k*-point mesh of 8×2×8 were set with the energy tolerance of 0.7 meV/atoms[128]. The calculated lattice parameters (LPs) of the two MAB phases were: MoAlB ($a = 3.215$ Å, $b = 14.035$ Å, $c = 3.109$ Å) and Fe_2AlB_2 ($a = 2.913$ Å, $b = 11.007$ Å, $c = 2.861$ Å), both in good agreement with the experimentally determined LPs[27]. The total energies of perfect structures as well as those containing either a vacancy or an antisite were calculated in 2×2×2 supercells. Interstitial calculations required larger supercells, which were determined based on the results of a convergence test. The reported values were calculated in the following supercells: 4×2×4 (Mo_I and Al_I in MoAlB and B_I in Fe_2AlB_2), 4×1×4 (B_I in MoAlB), 6×1×6 (Fe_I in Fe_2AlB_2), and 6×2×6 (Al_I in Fe_2AlB_2). Here, we use the Kröger-Vink notation to label point defects.

The defect formation energy (E_f) was calculated using the following equation,

$$E_f = E_{\text{defective}} - E_{\text{perfect}} + n_i\mu_i \qquad (i = \text{Mo, Fe, Al or B}) \tag{3.1}$$

where $E_{\text{defective}}$, E_{perfect}, n_i, and μ_i represent the total energy of a defective supercell, the total energy of a perfect supercell, the number of defect atoms, and the chemical potential of the defect atom, respectively. In addition to the formation energies, the migration energies of vacancies and interstitials were calculated. Also, the reaction energies and their energy barriers were calculated to consider possible reactions between defects. The migration energies and reaction energy barriers were calculated using the climbing image nudged elastic band method[111]. The interlayer binding energies between M and A layers were calculated by subtracting the total energy of the perfect unit cell from the total energy of a unit cell

where a gap of 1 nm is inserted between a M layer and the nearest A layer and by dividing the calculated value by the number of surface atoms.

3.3 Results and discussion

3.3.1 Radiation performance of MoAlB and Fe_2AlB_2

The damage introduced during the irradiation was analyzed using cross-sectional TEM and high-resolution (HR) TEM images shown in Fig. 3.4. The top and bottom rows correspond to MoAlB and Fe_2AlB_2, respectively. In Fig. 3.4, the left, center, and right columns correspond to the irradiation of 7.5 $\times 10^{16}$ ions·cm^{-2} at RT (RT-low), 1.5×10^{17} ions·cm^{-2} at RT (RT-high), and 1.5×10^{17} ions·cm^{-2} at 300 °C (300 °C-high), respectively. The images show that MoAlB irradiated at RT (both low and high dose) becomes entirely amorphous (Fig. 3.4(a)), as the selected area electron diffraction (SAED) pattern in Fig. 3.4(a) shows the diffusion rings without any indication of diffraction spots anywhere in the irradiated region and contrast in the dark field imaging, which is a typical result of amorphous materials. The amorphized structure was further confirmed by the HR TEM images as shown in Fig. 3.4(d). The 300 °C-high irradiation also led MoAlB to complete amorphization of the structure (Figs. 3.4(c) and (f)).

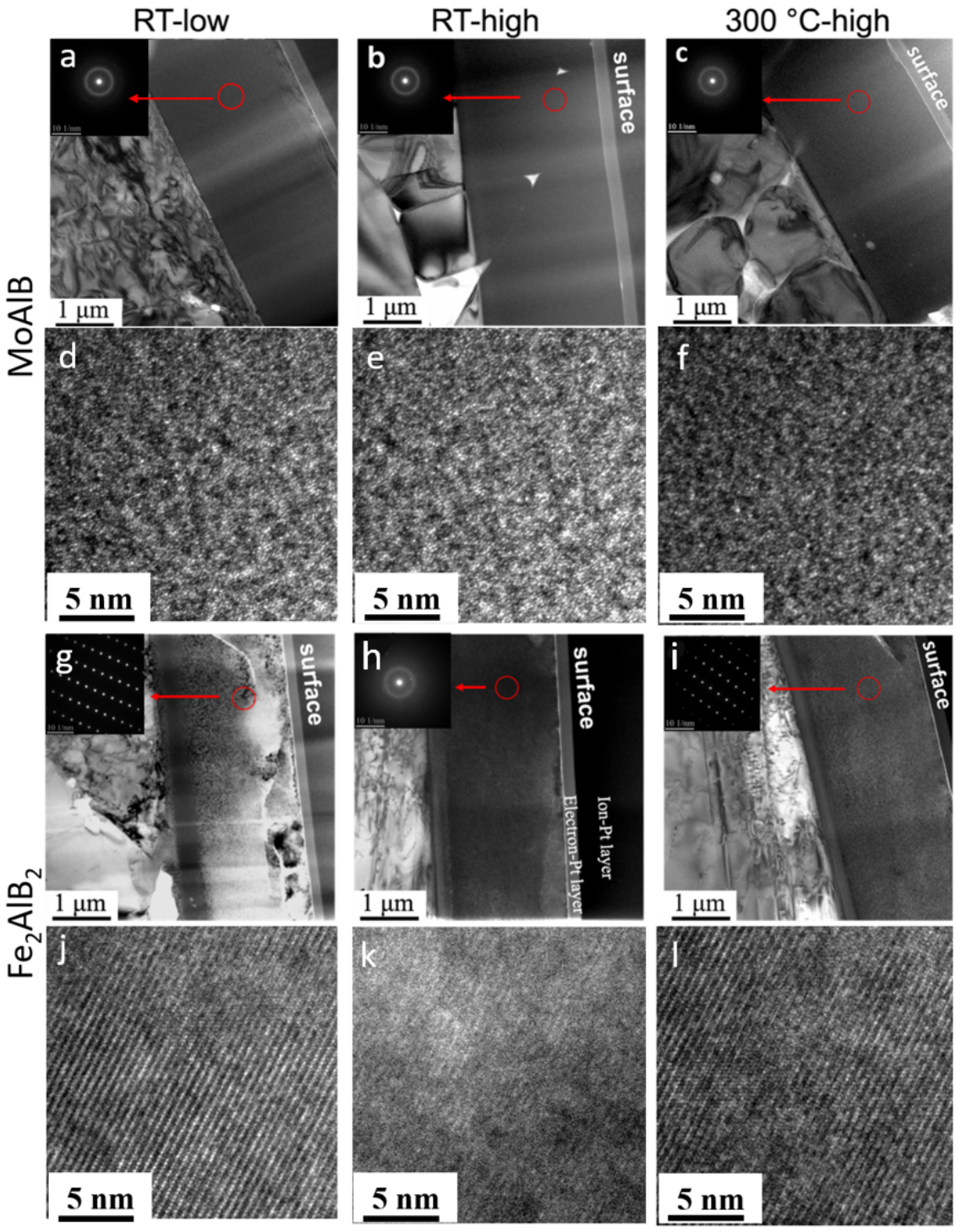

Figure 3.4 TEM and HR TEM images from [010] direction of MoAlB (top) and Fe_2AlB_2 (bottom), irradiated at 7.5 $\times 10^{16}$ ions·cm^{-2} at RT (left), at 1.5 $\times 10^{17}$ ions·cm^{-2} at RT (center), and at 1.5 $\times 10^{17}$ ions·cm^{-2} at 300 °C (right). The light-colored thin band on the top of the surface is the Pt protective layer deposited by the electron deposition, followed by the thicker and dark colored Pt protective layer deposited by the ion deposition during FIB.

Fe_2AlB_2 showed a much better resistance to radiation-induced amorphization under the same irradiation conditions. Specifically, after the RT-low irradiation Fe_2AlB_2 remained crystalline as evidenced by the SAED patterns shown in the inset of Fig. 3.4(g) and the HR TEM image shown in Fig. 3.4(j). The irradiation produced many black spot defects (corresponding to defect clusters), and the density of black spot defects is relatively higher in the region exposed to a higher dose in Fig. 3.4(g). However, there is no evidence of amorphization in most parts of the sample except for the damage peak region where there is an amorphous band with the width of ~0.2 μm, corresponding to the damage level of ~11 dpa. As the irradiation fluence increased up to 1.5×10^{17} ions·cm^{-2} at RT (RT-high), most parts of Fe_2AlB_2 were significantly damaged but there were still some crystalline structures, as shown in the HR TEM image of Fig. 3.4(k) and as indicated by the weak diffraction spots of the SAED pattern in the inset of Fig. 3.4(h). There is an obvious amorphization band with the width of 0.3 μm around the damage peak area, corresponding to the peak damage level of ~23 dpa. After the 300 °C-high irradiation, Fe_2AlB_2 remained crystalline, as evidenced by both the HR TEM image in Fig. 3.4(l) (which shows a highly ordered structure with some black spot defects) and the SAED pattern in the inset of Fig. 3.4(f) (which shows clear diffraction spots without rings). This result indicates that the dose to amorphization is larger at 300 °C than at RT. The width of the amorphous band is ~0.2 μm and the edge of the band in the near surface direction corresponds to a damage level of ~10 dpa. Combining our experimental results and the SRIM calculations, for 3.15 MeV carbon ions, the fluence to amorphize the flat region of Fe_2AlB_2 can be roughly estimated as 2.0×10^{17} ions·cm^{-2} at RT and 3.5×10^{17} ions·cm^{-2} at 300 °C. The dose to amorphization for Fe_2AlB_2 is about 10 dpa at RT and 16 dpa at 300 °C. Since MoAlB became amorphous at all the fluences, it was difficult to obtain the accurate fluence to amorphization. The fluence to amorphize the flat region of MoAlB is less than 7.5×10^{16} ions·cm^{-2}.

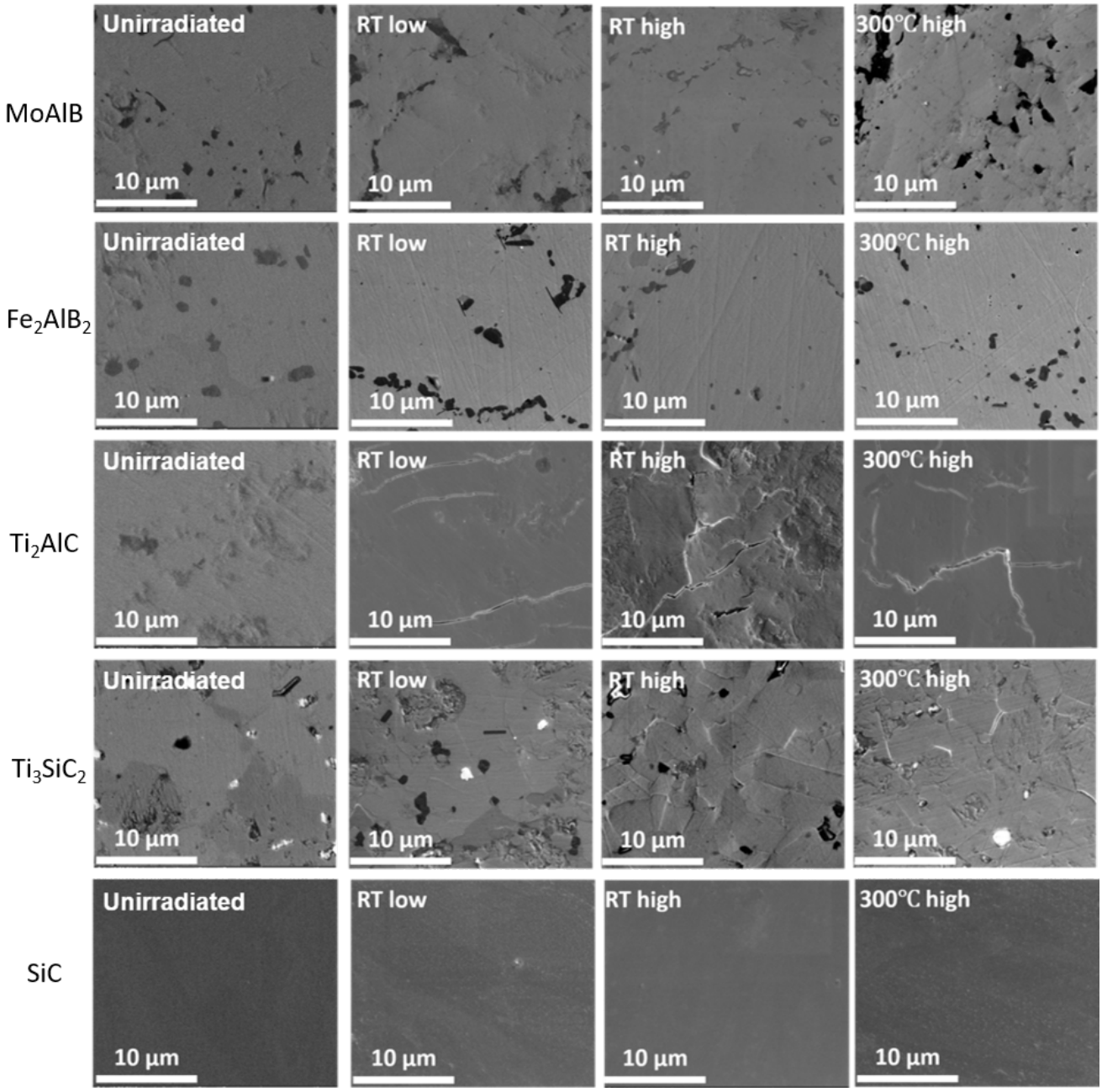

Figure 3.5 SEM images of MoAlB, Fe_2AlB_2, Ti_2AlC and Ti_3SiC_2 MAX phases, and CVD SiC. From left to right, before the irradiation, after the irradiation of RT-low, RT-high, and 300 °C-high.

The SEM images of all the irradiated MoAlB and Fe_2AlB_2 samples showed that the surface is free of cracks after the irradiation (see Fig. 3.5). In contrast, there are many radiation-induced cracks on the surfaces of Ti_2AlC and Ti_3SiC_2 irradiated at the same conditions. The cracks were quantified by drawing randomly oriented lines across the surface images, following the procedure outlined in a previous

study[116]. The number of crack intersections was counted for 10 lines, and it was divided by the total line length to provide a quantitative measure of the number of cracks per unit volume (S_v), using the formula $S_v = 2N$. Here, N is the average number of cracks per unit length of the randomly drawn surface lines. In our analysis we found obvious irradiation-induced cracks with the length of more than 10 μm on the surface of Ti_2AlC, even for the RT-low irradiation. The crack density for the RT-low irradiated Ti_2AlC was found to be 0.21 /μm. As the dose increased, the number of cracks observed on the surface also increased. The crack density for the RT-high irradiated sample was found to be 0.35 /μm. The cracking problems for the RT-high samples were significant enough to cause some bulging on the surface. For the 300 °C-high irradiated Ti_2AlC, the crack density dropped to 0.27/μm. In the case of Ti_3SiC_2, there were no cracks visible on the surface for the RT-low irradiation. As the dose increased, some small cracks with the lengths of 5-10 μm were found in both the RT-high and 300 °C-high irradiated samples. The length and the width of the cracks were much smaller than those in Ti_2AlC. The crack densities were found to be 0.29/μm and 0.18/μm for the RT-high and 300 °C-high irradiated Ti_3SiC_2 samples, respectively.

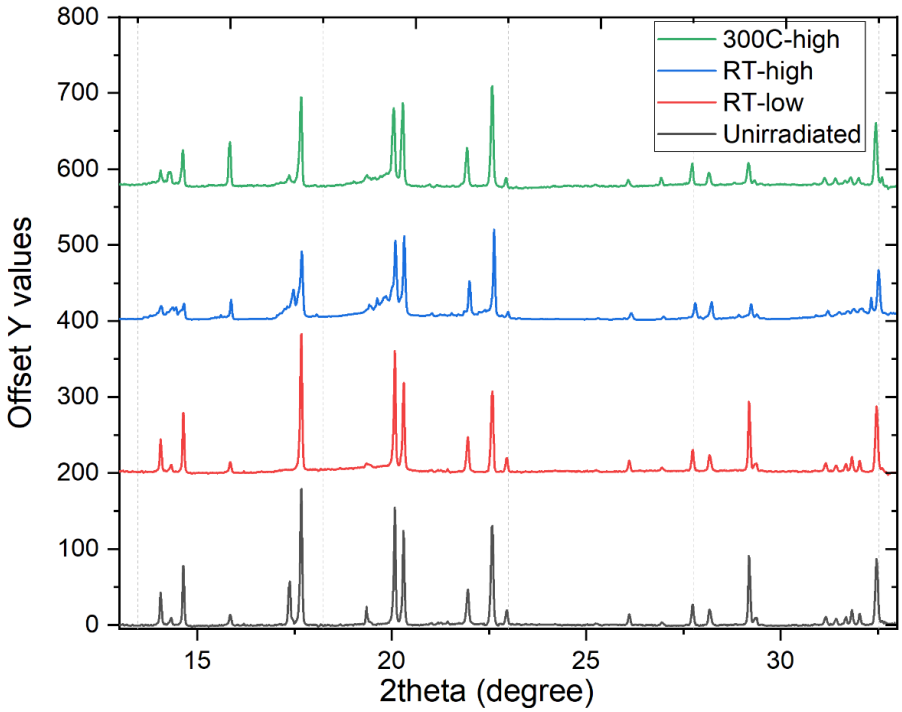

Figure 3.6 GI XRD spectra of Fe_2AlB_2 measured with the incident angle of 1.0° for unirradiated, RT-low irradiated, RT-high irradiated, and 300 °C-high irradiated samples.

The radiation-induced cracks in Ti_2AlC and Ti_3SiC_2 are believed to be caused by the anisotropic swelling, i.e., the lattice swelling along the *c* axis and contraction along the *a* axis[129,130]. To determine if there is radiation-induced anisotropic swelling in Fe_2AlB_2 (MoAlB was fully amorphized after the irradiation, so we did not analyze it), grazing incidence (GI) XRD spectra at the incident angle of 1.0° were collected and shown in Fig. 3.6. Unlike the GI XRD results of the irradiated MAX phases[129], where a significant shift of peaks has been reported, in this work, no obvious shift of peaks' positions was found in the spectra of the irradiated Fe_2AlB_2, indicating the changes in the LPs were very small. The refinement results of the GI XRD also showed that the irradiation-induced LP change in Fe_2AlB_2 was minimal (*a*-LP increased by 1.2%, *b*-LP decreased by 0.9 %, and *c*-LP decreased by 0.9%) compared with that of the MAX phase (*a*-LP decreased by ~1.0%, and *c*-LP increased by ~4%[129]). For the RT-high irradiated Fe_2AlB_2 sample, *a*-LP increased from 2.913 to 2.949 Å (1.2%), whereas *b*-LP decreased from 11.00 to 10.90 Å (0.9%) and *c*-LP decreased from 2.861 Å to 2.836 Å (0.9%). The LP changes in the RT-low and 300 °C-high irradiated samples were even smaller (increase in *a*-LP by <0.7% and decreases in *b*- and *c*-LPs by <0.3%). The results show that although there are slight anisotropic changes in the LPs of Fe_2AlB_2, these changes are much smaller than those reported in Ti_3SiC_2 and Ti_2AlC. Moreover, for the MAX phases, *a*-LP decreased and *c*-LP increased after the irradiation, whereas for Fe_2AlB_2, *a*-LP increased, and *b*- and *c*-LPs decreased after the irradiation. The lower swelling anisotropy as well as the lower overall swelling in Fe_2AlB_2 could be the reason for the lack of radiation-induced cracks in Fe_2AlB_2. SiC was found to be free of radiation-induced cracks for all the irradiation conditions considered in this chapter.

We have not found any radiation-induced phase transformation in Fe_2AlB_2. Such phase transformation has been reported in irradiated MAX phases[119,131]. Specifically, GI XRD spectra collected from Fe_2AlB_2 (see Fig. 3.6) show that no new peak was generated after the irradiation. Also, the SAED results from [010] direction show that there is no diffraction spot from other crystal structures, and the HR TEM results from the same direction show that the structure is the same except for the difference in the

defect densities and the level of disorder in the samples irradiated at the different conditions. These results support the conclusion that there is no radiation-induced phase transformation in Fe_2AlB_2.

3.3.2 Defect energetics: types of defects and formation energies

The experimentally observed trends in the tolerance to radiation-induced amorphization of the two MAB phases can be rationalized based on first-principles calculations. First of all, to calculate the defect formation energy using Eq. 3.1, I determined the chemical potentials of the constituent elements (Mo, Fe, Al, and B) in the two MAB phases, as shown in Fig. 3.7. The yellow lines are the precipitation lines of the binary phases, and the highlighted areas indicate the chemical potential ranges where MAB phases can form without precipitating other phases (see Section 3.5.1 for details). The line EF was chosen first to reflect the precipitated binaries Al_8Mo_3 and $Al_{13}Fe_4$, which are the predominant precipitates found in experiments[113,132], and then the line XY was selected in order to compare the two MAB phases at the same reference points; the two lines share the same chemical potential of Al, μ(Al).

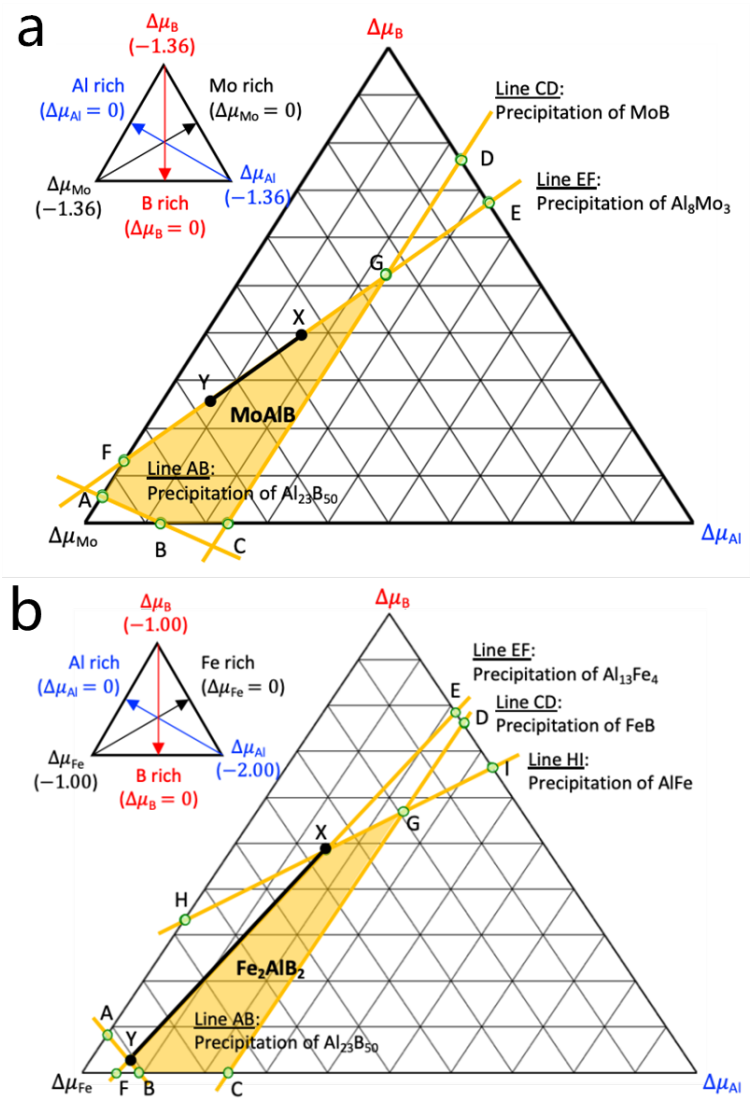

Figure 3.7 Chemical potential map of (a) MoAlB and (b) Fe_2AlB_2 with the highlighted area indicating the chemical potential ranges where MAB phases can form without precipitating other phases.

While each of the vacancy and antisite defects has only one possible equivalent site in MoAlB and Fe_2AlB_2, interstitials can potentially occupy several different positions. The potential interstitial sites investigated in this chapter are depicted in Fig. 3.1. The positions explored for MoAlB are Type I (center of a tetrahedron with four Al neighbors), Type II (center of an octahedron with five Al and one Mo neighbors), Type III (center of a tetrahedron with two Al and two Mo neighbors, having two cases depending on the orientation of the tetrahedron), and Type IV (center of a rectangle with four B neighbors). These interstitial sites were tested by placing an atom (Mo, Al, or B) near the center of the

potential interstitial site with a slight (0.15 Å) displacement from the symmetric point[133]. My calculations show that Al_I forms on Type I only. When an Al atom is placed on Type II or Type III positions, the configuration is unstable and spontaneously relaxes into Type I. Type IV was also found to be unstable. Specifically, the Al atom placed as an interstitial kicked out a Mo atom from its lattice site and formed an antisite, Al_{Mo}. Simultaneously, the displaced Mo atom kicked out another nearby Al atom from its lattice site, which finally resulted in the second Al atom taking an interstitial position of Type I. For B_I in MoAlB, the most stable position (lowest formation energy) is also found on Type I, followed by Type II (E_f higher than Type I by 1.29 eV), Type III-1 (E_f higher than Type I by 1.35 eV), and Type IV (E_f higher by 2.26 eV). B_I is not stable on Type III-2, and instead it relaxes into Type I. Interestingly, Mo has no stable site for its interstitial. Testing Type I-IV revealed that a Mo atom placed as an interstitial kicks out an Al atom and becomes an antisite, Mo_{Al}, making the kicked-out Al atom Al_I of Type I.

Similar types of interstitials were considered in Fe_2AlB_2 (see Fig. 3.1). These were Type I (center of an octahedron with four Al and two Fe neighbors), Type II (center of a tetrahedron with two Al and two Mo neighbors, having two cases depending on the orientation of the tetrahedron), Type III (center of a tetrahedron with two Al and two Fe neighbors, having two cases depending on the orientation of the tetrahedron), and Type IV (center of a rectangle with four B neighbors). I found that Al does not form any of these types of interstitial defects. Specifically, when an Al atom is placed on Type I-III positions, it spontaneously relaxes into the Al layer and forms a dumbbell-like interstitial with another Al atom. An Al atom placed on Type IV kicks out a Fe atom and becomes an antisite, Al_{Fe}. The displaced Fe atom forms Fe_I of Type II-1. For B_I in Fe_2AlB_2, the most stable position is Type I, followed by Type III-2 (E_f higher by 1.22 eV), Type IV (E_f higher by 1.58 eV), and Type III-1 (E_f higher by 8.20 eV). Placing a B atom on Type II revealed that B_I is not stable on these sites, and instead it relaxes to the configuration of Type I. Lastly, Fe_I forms only on Type II; the most stable is the Type II-1 configuration, followed by Type II-2 (E_f higher by 0.63 eV). A Fe atom placed on the other sites relaxes into Type II-1.

In summary, the most stable interstitials in MoAlB and Fe_2AlB_2 are all located in the Al layer (see Section 3.5.2 for details), which has been observed in MAX phases as well[35]. Note that Mo_I does not form because Mo_I is unstable and instead forms Mo_{Al} and Al_I. The defect configuration found in this study implies that most Frenkel Pairs (FPs) likely form in Al layers, which play a crucial role in accommodating defects, similarly to what has been reported in MAX phases. Therefore, in this study I focus only on the interstitials in the Al layers along with the other point defects.

In Table 3.1, I report the formation energies calculated using Eq. 3.1 on the line XY from Fig. 3.7. The formation energies of vacancies, interstitials, and antisites vary depending on the chemical potentials, whereas that of FPs is independent of the chemical potentials. As mentioned earlier, Mo_I does not form in MoAlB, and instead it relaxes to Mo_{Al} and Al_I, thus Mo_{FP} is labeled as "unstable."

Table 3.1 Formation energies of point defects in MoAlB and Fe_2AlB_2. The energies are referenced to the chemical potentials along the XY line in Fig. 3.5.

M = Mo, Fe	Formation energy (eV)	
	MoAlB	Fe_2AlB_2
V_M	1.94-2.26	0.55-1.05
V_{Al}	1.00-1.12	2.11-2.23
V_B	0.56-0.76	0.07-0.51
M_I	$Mo_I \rightarrow Mo_{Al} + Al_I$	4.86-5.36
Al_I	6.42-6.54	5.59-5.71
B_I	3.06-3.26	2.26-2.70
M_{Al}	2.13-2.57	0.85-1.47
M_B	6.97-7.49	3.47-4.41
Al_M	1.77-2.21	1.34-1.96
Al_B	2.44-2.52	2.84-3.16
B_M	3.92-4.44	2.78-3.72
B_{Al}	1.66-1.74	2.66-2.98
M_{FP}	unstable	2.96
Al_{FP}	3.77	3.91
B_{FP}	1.91	1.39

3.3.3 Defect kinetics: migration energies and reaction energy barriers

Table 3.2 shows the calculated migration energies. I report only the migration energies for vacancies and interstitials, because the direct migration of an antisite would involve an exchange with a neighboring atom on the lattice, which is energetically prohibitive. The tabulated migration energies are the lowest energies among the possible migration paths. V_{Al} in MoAlB has the lowest migration energy (0.46 eV) when migrating into the nearest diagonal site within an Al layer, whereas the migration along the *a*-axis and *c*-axis (see Fig. 3.1) have the migration energies of 3.45 eV and 2.98 eV, respectively. V_B migrating along the *c*-axis has the migration energy of 0.68 eV. The migration of V_{Mo} is very unlikely; the lowest energy (5.27 eV) is obtained when V_{Mo} moves along the *c*-axis in the same Mo plane, whereas the migration along the *a*-axis in the same Mo plane and into another Mo plane through the B layers have the energies of 5.54 eV and 6.67 eV, respectively. The migration energy of V_{Mo} can decrease when there are nearby Mo_{Al} that exert a repulsive force on V_{Mo} (i.e., attractive force to the migrating Mo atom). When Mo_{Al} is located at the nearest site to V_{Mo}, the migration energy of V_{Mo} is calculated to be 4.84 eV, while that of V_{Mo} with Mo_{Al} located at the 2nd nearest site is 5.03 eV.

Table 3.2 Migration energies of vacancies and interstitials in MoAlB and Fe_2AlB_2.

M = Mo, Fe	Migration energy (eV)					
	V_M	V_{Al}	V_B	M_I	Al_I	B_I
MoAlB	5.27	0.46	0.68	×	0.37	1.40
Fe_2AlB_2	3.34	1.17	0.50	1.07	0.25	0.92

In the case of interstitials, I only consider the migration of the most stable interstitial into equivalent positions, namely, these are migrations within the Al layer. Al_I in MoAlB has three migration paths: along the *a*-axis, the *c*-axis, and a diagonal line within the Al layer, with the energy barriers of 0.37 eV, 1.25 eV, and 2.43 eV, respectively. Next, B_I in MoAlB has the same three migration paths: along the *a*-axis, the *c*-axis, and a diagonal line within the Al layer, with the energy barriers of 1.40 eV, 1.65 eV, and 2.22 eV, respectively.

As for the defect migration in Fe_2AlB_2, V_{Al} has two migration paths: along the *a*-axis (1.17 eV) and along the *c*-axis (1.51 eV) in the same Al plane. V_B can migrate along the *a*-axis with the energy of 0.50 eV, and V_{Fe} has three possible migration paths: along the *a*-axis (4.42 eV), the *c*-axis (5.02 eV), and into another Fe plane through the B layers (3.34 eV). Al_I can migrate by transitioning from one dumbbell position to another: along the *c*-axis (0.25 eV) and along the *a*-axis (0.36 eV). B_I has two paths of migration into another octahedral site: along the *a*-axis (1.20 eV) and along the *c*-axis (0.92 eV). Lastly, Fe_I has two paths of migration into another tetrahedral site: along the *a*-axis and the *c*-axis, with the migration energies of 1.42 eV and 1.07 eV, respectively.

Previous theoretical studies have rationalized the radiation tolerance of ternary MAX phases based on such parameters as the radiation stability of the corresponding M-X binaries (i.e., TiC for Ti_3SiC_2), M-A bonding characteristics (i.e., the weaker the bond, the better the radiation resistance), the ratio of the number of A and MX layers (i.e., the higher the ratio, the better the radiation resistance), and the formation energy of a M_A-A_M antisite pair (i.e., the lower the formation energy of the pair, the better the radiation resistance)[35,117,118]. Similar analysis in the MAB phases is not possible at this point, because of the limited research to date on the radiation effects in MAB phases. It is, however, still instructive to ask if the criteria proposed for MAX phases are consistent with our observation that Fe_2AlB_2 has shown a better resistance to radiation-induced amorphization than MoAlB. First of all, rationalizing the radiation resistance of the ternary MAB phases based on radiation studies of the corresponding M-B binaries cannot be tested here because studies on radiation-induced amorphization of MoB or FeB have not been reported yet, except for Fe_3B. Fe_3B irradiated at 385 K showed partial amorphization at the fluence of 10^{19} ions/cm^2 and full amorphization at the fluence of 2×10^{19} ions/cm^2 [134]. Although Mo_2B_5 was studied with the irradiation of 10^{19} ions/cm^2 [135], the focus of this study was on radiation-induced swelling and fracturing, not on radiation-induced amorphization. Secondly, I tested the hypothesis related to the M-A bonding energy, calculated to be 1.67 eV and 1.12 eV, for MoAlB and Fe_2AlB_2 respectively. Thus, the lower bonding energy of Fe_2AlB_2 possibly contributes to the tolerance to radiation-induced amorphization. However, it is still difficult to conclude whether the M-A bonding energy is indeed

responsible for the observed trend in radiation resistance. For instance, Ti_3SiC_2 is known to be more tolerant to radiation-induced amorphization than Ti_2AlN, but the M-A bonding energy of the latter is weaker[35]. Next, the density of A layers is 1/3 in MoAlB and 1/5 in Fe_2AlB_2, so the higher density of the A layers in MoAlB is consistent with the hypothesis that the fraction of A layers correlates with the tolerance to radiation induced amorphization. As for the last criterion, the lower M_A-A_M pair formation energy in Fe_2AlB_2 (2.81 eV) compared with that in MoAlB (4.34 eV) could potentially contribute to the tolerance to radiation-induced amorphization, but it cannot be solely used to determine the tolerance trends because of counter examples. For instance, the M_A-A_M pair formation energies in Ti_3SiC_2 and Cr_2AlC are 3.52 eV and 2.40 eV, respectively, but the former is known to be more tolerant to radiation-induced amorphization.

To summarize, some of the criteria proposed for the radiation resistance of MAX phases are consistent with the results of our experimental studies on MAB phases (i.e., formation energies of the antisite pair and the bond characteristics), some are not (i.e., the ratio of the number of A and MB layers), and in some cases there is no data (i.e., there are no consistent studies of the corresponding binaries). Therefore, more extensive studies on multiple MAB phases will be needed to determine whether there exist simple correlations between fundamental defect properties and the radiation resistance across different MAB phases. There are also some key differences between MAX and MAB phases. For instance, if other MAB phases do not undergo phase transformation driven by antisites (consistently with what I found for Fe_2AlB_2), then perhaps the formation energies of antisites are not the determining factor in resistance to radiation-induced amorphization of these materials.

To rationalize the observations from our experiments on the MAB phases and to understand how radiation-induced damages can be annealed, I have analyzed the defect energetics in more detail, including the defect migration and reactions.

Table 3.3 Reaction energies and energy barriers for reactions between point defects in MoAlB and Fe_2AlB_2. "Diff" means a diffusion-limited reaction and the number in parenthesis is the lower of the migration energies of the reactant defects. A negative reaction energy means that the reaction is energetically favorable, and "unstable" means that those reactions cannot occur because they involve Mo_I, which is unstable and spontaneously transforms into Mo_{Al} and Al_I (see Table 3.1).

#	Reaction (M = Mo, Fe)	Reaction energy (eV)		Reaction energy barrier (eV)	
		MoAlB	Fe_2AlB_2	MoAlB	Fe_2AlB_2
1	$Al_B + V_{Al} \rightarrow V_B + Al_{Al}$	−2.89	−4.88	Diff (0.46)	Diff (1.17)
2	$Al_M + V_{Al} \rightarrow V_M + Al_{Al}$	−0.95	−3.02	0.19	Diff (1.17)
3	$B_{Al} + V_B \rightarrow V_{Al} + B_B$	−1.30	−0.94	Diff (0.68)	0.12
4	$B_M + V_B \rightarrow V_M + B_B$	−2.74	−2.74	Diff (0.68)	0.07
5	$M_{Al} + V_M \rightarrow V_{Al} + M_M$	−3.39	+0.21	1.36	1.81
6	$M_B + V_M \rightarrow V_B + M_M$	−8.67	−4.45	Diff (5.27)	Diff (3.34)
7	$Al_I + V_{Al} \rightarrow Al_{Al}$	−6.82	−7.82	Diff (0.37)	Diff (0.25)
8	$M_I + V_M \rightarrow M_M$	unstable	−5.91	unstable	Diff (1.07)
9	$B_I + V_B \rightarrow B_B$	−3.82	−2.77	1.33	1.02
10	$M_I + V_{Al} \rightarrow M_{Al}$	unstable	−6.12	unstable	Diff (1.07)
11	$B_I + V_{Al} \rightarrow B_{Al}$	−2.52	−1.83	Diff (0.46)	Diff (0.92)
12	$Al_I + M_{Al} \rightarrow M_I + Al_{Al}$	unstable	−1.71	unstable	Diff (0.25)
13	$Al_I + B_{Al} \rightarrow B_I + Al_{Al}$	−4.30	−6.00	Diff (0.37)	Diff (0.25)
14	$M_B + V_{Al} \rightarrow M_{Al} + V_B$	−5.39	−4.60	Diff (0.46)	Diff (1.17)

In order to determine how different defect recovery processes can lead to the radiation resistance of MAB phases, ideally one would build a detailed rate theory model[136–138]. However, the development of such a model is beyond the scope of this project. Instead, I consider specific reactions between point defects to determine if the radiation resistance of the two MAB phases can be explained by the presence of defects that are difficult to anneal out. Possible reactions between different point defects are listed in Table 3.3 with the reaction energy and the reaction energy barrier. "Diff" denotes a diffusion-limited reaction, in which the reaction occurs spontaneously when the reactants are near each other. Note that the

reactions involving Mo_I do not occur because Mo_I is unstable and spontaneously transforms into Mo_{Al} and Al_I (see Table 3.1).

On the basis of Tables 3.1-3.3, I identified defect species that are easily annealed by reactions and defects that cannot be removed and likely remain in the lattice at the temperature of our experiments – RT (150 °C) and 300 °C. By calculating the hopping rate, I define the energy range in which the reaction can occur rapidly at a given temperature and therefore the defects can be removed.

In order to determine whether a defect is able to be annealed (e.g., by reacting with other defects), I assume that it has to move at least 1 nm over a reasonable time period (here assumed to be 100 s). Taking this criterion and the pre-exponential factor to be 10^{13} s^{-1} one can estimate that defects with the energy barrier of 1.17 eV (82 s) can be annealed. I assume that defects with the migration energy or reaction energy barrier higher than 1.33 eV (104 min) will take much longer to anneal – 76 times longer than reactions with the barrier of 1.17 eV. Note, that there is no reaction whose migration or reaction energy barrier is in the range between 1.17 and 1.33 eV. At the higher temperature (300 °C), the reactions whose migration energy or reaction energy barrier is 1.40 eV can occur within 2.82 s, while the migration or reaction energy barrier of 3.34 eV or higher is still too high for the reaction to occur on the time scales of experiments. Note, that there is no reaction whose migration or reaction energy barrier is in the range between 1.40 and 3.34 eV. Using the above criteria, I have analyzed possible reactions between defects, summarized in Table 3.3.

First of all, it is known that FPs are introduced as the direct consequence of radiation, so how they are recovered significantly affects the tolerance to radiation-induced amorphization. In the two MAB phases studied here, most vacancies and interstitials in the two MAB phases can be removed through the FP recombination. V_{Al} and Al_I in MoAlB can be removed through the reaction #7 in Table 3.3 with the aid of the negative reaction energy, the low energy barrier (barrierless), and the low migration energy of Al_I (0.37 eV). V_{Al} and Al_I in Fe_2AlB_2 can also be removed through the reaction #7 with the aid of the negative reaction energy, the low energy barrier (barrierless), and the low migration energy of Al_I (0.25 eV). As for V_B and B_I, they can be removed through the FP recombination (#9) in MoAlB (negative

reaction energy, V_B migration energy of 0.68 eV, and energy barrier of 1.33 eV) and in Fe_2AlB_2 (negative reaction energy, V_B migration energy of 0.50 eV, and energy barrier of 1.02 eV). In addition, V_B and B_I can recombine through the other path, i.e., via the formation of B_{Al}. In MoAlB, B_I can easily become B_{Al} through the reaction #11 (negative reaction energy, V_{Al} migration energy of 0.46 eV, and barrierless reaction), and then B_{Al} easily reacts with V_B through the reaction #3 (negative reaction energy, V_B migration energy of 0.68 eV, and barrierless reaction). In Fe_2AlB_2, B_I can become B_{Al} through the reaction #11 (negative reaction energy, B_I migration energy of 0.92 eV, and barrierless reaction), and then B_{Al} reacts with V_B through the reaction #3 (negative reaction energy, V_B migration energy of 0.50 eV, and low energy barrier of 0.12 eV). As discussed earlier, Mo_I is not stable in MoAlB, and instead it forms Mo_{Al}, hence we do not consider the FP recombination of Mo. Meanwhile, Fe_I in Fe_2AlB_2 can be removed through the reaction #8 with the negative reaction energy, Fe_I migration energy of 1.07 eV, and barrierless reaction.

Al_B in both MAB phases can be removed through the reaction #1. In MoAlB, the reaction energy is negative, V_{Al} migration energy is 0.46 eV, and the reaction is barrierless, whereas in Fe_2AlB_2, the reaction energy is negative, V_{Al} migration energy is 1.17 eV, and the reaction is barrierless. Al_M in the two MAB phases can be removed through the reaction #2 in MoAlB (negative reaction energy, V_{Al} migration energy of 0.46 eV and low energy barrier of 0.19 eV), and Fe_2AlB_2 (negative reaction energy, V_{Al} migration energy of 1.17 eV and barrierless reaction). Next, B_M in both MAB phases can be removed through the reaction #4 with the aid of the negative reaction energies, low energy barriers (barrierless in MoAlB and 0.07 eV in Fe_2AlB_2) and/or the low migration energies of V_B (0.68 eV in MoAlB and 0.50 eV in Fe_2AlB_2). And as mentioned above, B_{Al} can be removed through the reaction #3 while providing an intermediate site for the recombination of V_B and B_I.

Before looking into Mo_{Al} in MoAlB, I should note that a significant number of Mo_{Al} can form due to the unstable Mo_I as well as from the direct consequence of radiation. However, Mo_{Al} cannot be easily removed in MoAlB even at the high temperature (300 °C) because of the high migration energy of V_{Mo} (5.27 eV), which is still too high for the migration to occur. Recall that we assume that the reactions

whose migration or energy barrier is higher than 3.34 eV cannot occur at 300 °C. As discussed earlier, although the existence of Mo_{Al} near V_{Mo} can decrease the migration energy down to 4.84 eV, it is still too high for the migration to occur. Finally, the only reaction which can remove this defect (#5) cannot occur. There are other potential reactions that could anneal Mo_{Al} (e.g., $B_I + Mo_{Al} \rightarrow B_{Al} + Mo_I$ or $Mo_{Al} + Al_{Mo} \rightarrow Al_{Al} + Mo_{Mo}$). However, the former reaction does not occur due to the formation of an unstable Mo_I, and the latter, which is the exchange of antisites, is energetically prohibitive.

In contrast, Fe_{Al} in Fe_2AlB_2 can be removed through the reaction #12 with the aid of the negative reaction energy, low migration energy of Al_I (0.25 eV), and the barrierless reaction. Although this process creates Fe_I, this interstitial can be removed through the reaction #8 as discussed earlier.

Lastly, M_B in both MAB phases can be removed through the reaction #14 with the aid of the negative reaction energies, low migration energies in MoAlB (0.46 eV) and in Fe_2AlB_2 (1.17 eV), and low reaction energy barriers (barrierless). This reaction path creates V_B with M_{Al} antisites, whose behavior is distinct in the two MAB phases as discussed earlier, i.e., Mo_{Al} cannot be removed whereas Fe_{Al} can be removed. Therefore, this reaction creates the defect species (Mo_{Al}) that cannot be removed in MoAlB, whereas it can contribute to the recovery process in Fe_2AlB_2. Changing the energy criterion to the higher temperature (300 °C) does not change the aftermath of defect behavior in the two MAB phases. We assumed that at 300 °C reactions with the migration energy or reaction energy barrier that is lower or equal to 1.6 eV can occur within a few minutes, while the migration or reaction energy barrier of 3.34 eV or higher is too high for the reaction to occur. The migration energy of V_{Mo} (5.27 eV) in the reaction #8 for removing Mo_{Al} is still too high in this energy range, whereas all the defects in Fe_2AlB_2 can be annealed out.

In summary, the better tolerance to radiation-induced amorphization of Fe_2AlB_2 as compared with MoAlB can be rationalized by the increased production of and the difficulty in annealing out antisites in MoAlB. In MoAlB, unstable Mo_I (and therefore unstable Mo FP) is expected to lead to a larger production of Mo_{Al}, which are difficult to anneal out due to the high migration energy of V_{Mo}. In addition, Mo_{Al} in MoAlB is difficult to anneal out even at 300 °C, whereas Fe_2AlB_2 has no such defects.

In Fe_2AlB_2, all the defects are expected to anneal out in a reasonable period of time at both RT and 300 °C.

3.3.4 Comparison with MAX phases

Since Fe_2AlB_2 and MoAlB MAB phases are both layered ternary borides, which have similar structures to the MAX phases, it is instructive to compare the radiation resistance of MAB phases to that of selected MAX phases. We specifically chose Ti_3SiC_2 and Ti_2AlC, since Ti_3SiC_2 is a MAX phase with an unusually high resistance to radiation-induced amorphization, and Ti_2AlC contains Al, just like the MAB phases considered here. We also compare the MAB phases with SiC, which is considered to have excellent radiation resistance[139] and is a promising material for cladding applications in nuclear reactors. Cross-sectional TEM images of SiC, Ti_2AlC, and Ti_3SiC_2 irradiated simultaneously with the MAB phases are shown in Fig. 3.8.

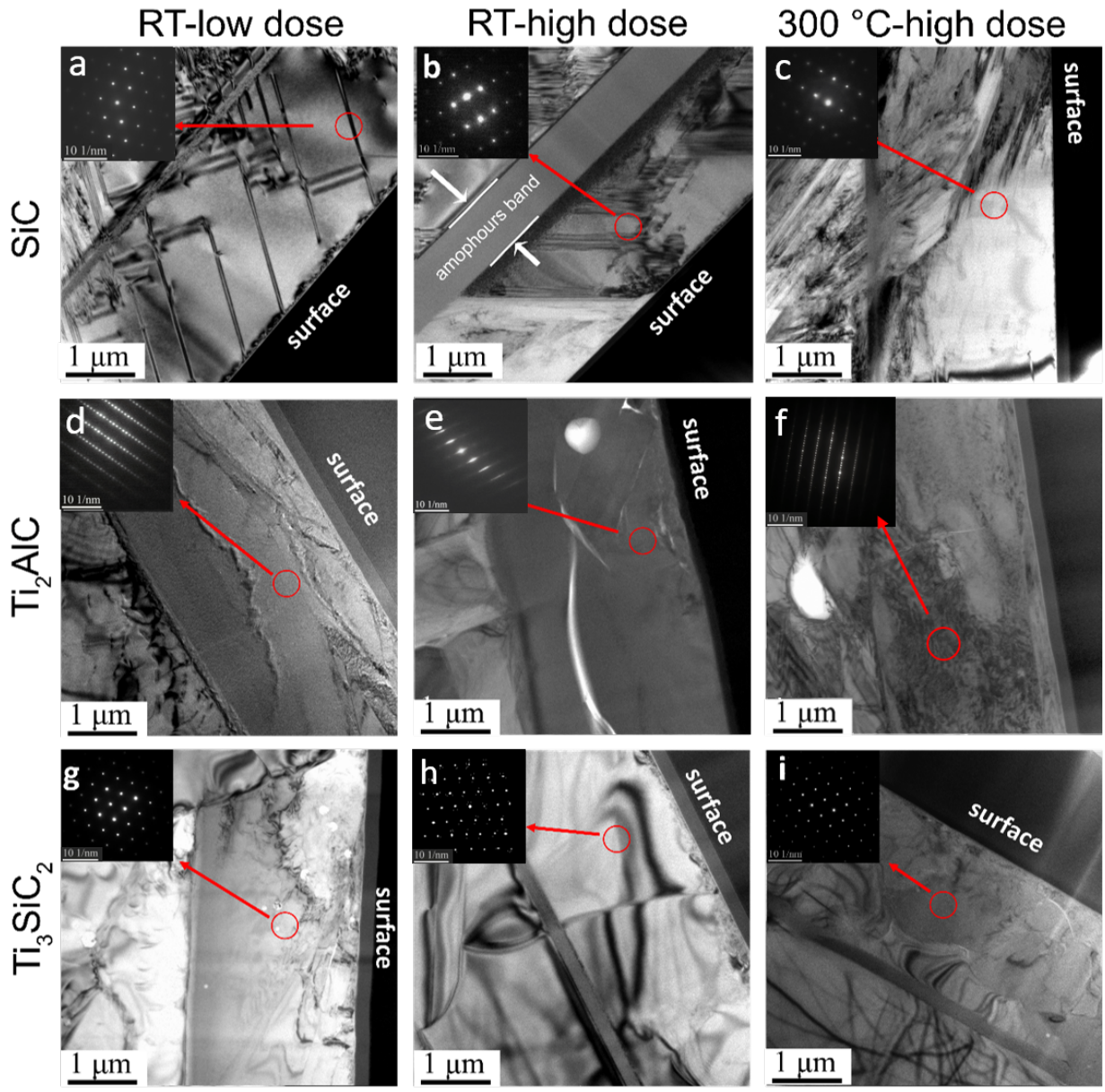

Figure 3.8 TEM images of SiC (top) from [001] direction, MAX phases Ti_2AlC (center) from [11-20] direction and Ti_3SiC_2 (bottom) from [0001] direction, irradiated at 7.5 $\times 10^{16}$ ions·cm^{-2} at RT (left), at 1.5 $\times 10^{17}$ ions·cm^{-2} at RT (center), and at 1.5 $\times 10^{17}$ ions·cm^{-2} at 300 °C (right). The incident beam is perpendicular to the surface of the sample. The light-colored thin band on the top of the surface is the Pt protective layer deposited by electron deposition followed by the thicker and dark colored Pt protective layer deposited by ion deposition during FIB.

All the samples irradiated at RT-low remained crystalline after the irradiation as evidenced by clear diffraction spots in the SAED patterns shown in the insets of Fig. 3.8. In all the samples, the irradiation produced many small defect clusters throughout the irradiated regions visible as black spot defects, but no amorphization in the flat damage region was found (see Figs. 3.8(a), (d), and (g)). A very

thin (~0.1 μm) amorphous band formed in the implanted region (at the depth of 2.5-2.6 μm) in the CVD SiC as shown in Fig. 3.8(a). There is no obvious amorphous band in Ti_2AlC and Ti_3SiC_2, but there are many radiation-induced cracks on the surface of Ti_2AlC as shown in Fig. 3.6. The cracks are longer than 10 μm and they extend throughout the entire irradiation range confirmed by TEM. No obvious crack was found on the surface of Ti_3SiC_2 at this dose.

For the RT-high irradiated samples, there was an obvious amorphous band (wider than 0.9 μm) which formed around the implantation peak in the CVD SiC. According to Fig. 3.3, the damage level in that region is ~8 dpa at the edge of this band closer to the sample surface, rising up to 30 dpa at the peak region. The region where the dose was relatively flat (approximately 1.0 to 2.1 dpa (see Fig. 3.3)) remained crystalline. The density of the black spot defects appears to be very high near the amorphous band region. Under the same irradiation conditions, Ti_2AlC and Ti_3SiC_2 still exhibit crystallinity, as evidenced by clear diffraction spots in the SAED patterns. Some of the diffraction spots disappeared in the SAED pattern of Ti_2AlC (Fig. 3.8(e)), which means that the damage was significant at this dose. Many radiation-induced cracks concentrated in the irradiated region were found in Ti_2AlC, as shown in Fig. 3.8(e). An obvious void as well as a rougher surface was observed in the irradiated region of Ti_2AlC, as shown in Fig. 3.8(e), which should correspond to the bulges on the surface from the SEM images (Fig. 3.5). There is no amorphous band at all, even at the peak region. Based on the SRIM results in Fig. 3.3, the radiation dose in the peak region is ~26 dpa for Ti_2AlC and ~29 dpa for Ti_3SiC_2. More radiation-induced cracks were found on the surface of the RT-high irradiated Ti_2AlC, as shown in the SEM images of Fig. 3.5. These cracks are larger than those observed in the RT-low irradiated sample and tend to connect with each other to form a crack network. There are also some small cracks on the surface of Ti_3SiC_2 as shown in Fig. 3.5, but they were not observed in the deeper region from TEM results.

For the 300 °C-high irradiated samples, the diffraction patterns from all the samples showed clear diffraction spots, indicating the samples were still crystalline after the irradiation. A small amorphous band with the width of only ~0.1 μm was found in SiC (Fig. 3.8(c)), indicating the dose to amorphization increases from ~8 dpa to ~20 dpa at 300 °C, compared with the RT-high result. For Ti_2AlC, no obvious

radiation-induced cracks were found in the TEM image (Fig. 3.8(f)), indicating there were fewer cracks than the RT-high case. However, many radiation-induced cracks can still be observed in the SEM images as shown in Fig. 3.5. An obvious void with the diameter of about 1 μm can be seen in the near peak region. The surface roughness is also smoother than in the RT-high case. Even though the irradiation dose was relatively high, no obvious phase transformation was found in either Ti_2AlC or Ti_3SiC_2, which have been observed in ion-irradiated MAX phases in earlier studies[140,141]. However, partial phase transformation might have occurred in some areas, and it requires higher magnification TEM or HR TEM to detect.

Our experiments have shown that the resistance to radiation-induced amorphization of Fe_2AlB_2 is comparable to that of SiC. One should note that the resistance of Ti_2AlC and Ti_3SiC_2 to radiation-induced amorphization is better than that of the two MAB phases, but the MAX phases show radiation-induced cracking whereas the MAB phases do not. In addition, Fe_2AlB_2 has already shown to have a high decomposition temperature[114] and cracking resistance[120], which are beneficial for nuclear reactor applications.

3.4 Conclusions

TEM analysis showed that Fe_2AlB_2 remains fully crystalline under the irradiation of 7.5×10^{16} ions·cm^{-2} at RT and 1.5×10^{17} ions·cm^{-2} at 300 °C, while showing partial amorphization under the irradiation of 1.5×10^{17} ions·cm^{-2} at RT. In contrast, MoAlB became amorphous under the identical irradiation conditions. On the basis of first-principle calculations, I rationalized our experimental results. In MoAlB, Mo_I cannot form in the lattice and instead it is expected to create many antisites, Mo_{Al}. These antisites cannot be easily removed due to the high migration energy (5.27 eV) of V_{Mo}. In contrast, all the defects in Fe_2AlB_2 are expected to anneal out at both RT and 300 °C. We also performed radiation studies on CVD SiC, MAX phase Ti_2AlC and Ti_3SiC_2 with the same irradiation conditions used in the MAB phases. The MAX phases showed that they are tolerant to radiation-induced amorphization under all the irradiation conditions, whereas CVD SiC showed similar trends to Fe_2AlB_2. Specifically, SiC got

amorphized under the irradiation of 1.5×10^{17} ions·cm^{-2} at RT and remained crystalline under the other conditions. Our experiments also revealed that the MAX phases showed radiation-induced cracking, which was not found in the MAB phases.

Our study points to MAB phases as a promising class of materials for applications in environments that involve radiation and potentially corrosion (as explained in the introduction of this chapter). Numerous MAB phases have been predicted theoretically, and further studies are needed to explore the full potential of these materials for applications in harsh environments.

3.5 Supplementary Information

3.5.1 Determination of chemical potentials

In order to MoAlB to form, its formation energy is required as below,

$$E_{\mathrm{Total}}(\mathrm{MoAlB}) = \sum \mu_i^{\mathrm{MoAlB}} \quad (i = \mathrm{Mo, Al, B}) \tag{3.S1}$$

$$E_f(\mathrm{MoAlB}) = E_{\mathrm{Total}}(\mathrm{MoAlB}) - \sum \mu_i^{\mathrm{Bulk}} \tag{3.S2}$$

$$= \sum \Delta\mu_i \qquad (i = \mathrm{Mo, Al, B}), \tag{3.S3}$$

where E_{Total} is the calculated total energy, E_f is the formation energy, μ_i^{MoAlB} is the chemical potential of constituent element in MoAlB, and μ_i^{Bulk} is the chemical potential from its bulk. The calculated $E_f(\mathrm{MoAlB})$ is -1.36 eV. Next, to prevent the formation of competing binary phases, following conditions are required:

$$E_f(\mathrm{Al_8Mo_3}) > 8\Delta\mu_{\mathrm{Al}} + 3\Delta\mu_{\mathrm{Mo}} \tag{3.S4}$$

$$E_f(\mathrm{MoB}) > \Delta\mu_{\mathrm{Mo}} + \Delta\mu_{\mathrm{B}} \tag{3.S5}$$

$$E_f(\mathrm{Al_{23}B_{50}}) > 23\Delta\mu_{\mathrm{Al}} + 50\Delta\mu_{\mathrm{B}}. \tag{3.S6}$$

The binaries Al_8Mo_3 and MoB were selected because they are found in synthesized MoAlB samples, while $Al_{23}B_{50}$ is chosen because that is the most stable phase (i.e., the lowest formation energy) of Al-B system. The calculated formation energies of Al_8Mo_3, MoB, and $Al_{23}B_{50}$ are -3.59 eV, -1.04 eV, and -4.27 eV, respectively. Finally, preventing the precipitation of elemental solids from MoAlB requires the following equation:

$$\mu_i^{\mathrm{Bulk}} > \mu_i^{\mathrm{MoAlB}} \quad (i = \mathrm{Mo,\ Al,\ B}). \tag{3.S7}$$

Using Eq. 3.S1-7 and the calculated formation energies, the chemical potential map of MoAlB was determined and shown in Fig. 3.7. Following the same process, the chemical potential map of Fe_2AlB_2 was determined, with the calculated formation energies of Fe_2AlB_2 (-2.00 eV) and of the binaries found in synthesized Fe_2AlB_2 ($Al_{13}Fe_4$: -5.67 eV, AlFe: -0.66 eV, and FeB: -0.76 eV). The chemical potential set ($\mu_{\mathrm{Mo/Fe}}$, μ_{Al}, μ_{B}) for the characteristic points (A-I, X, and Y) are tabulated in Table 3.S1.

Table 3.S1 Chemical potential set ($\mu_{Mo/Fe}$, μ_{Al}, μ_B) for the characteristic points (A-I, X, and Y) indicated in Fig. 3.7.

eV	MoAlB			Fe_2AlB_2		
	μ_{Mo}	μ_{Al}	μ_B	μ_{Fe}	μ_{Al}	μ_B
A	–12.20	–3.75	–6.79	–9.15	–3.75	–6.79
B	–12.10	–3.94	–6.70	–9.15	–3.94	–6.70
C	–11.96	–4.08	–6.70	–9.00	–4.23	–6.70
D	–10.92	–4.08	–7.74	–8.24	–4.23	–7.47
E	–10.92	–4.20	–7.62	–8.24	–4.19	–7.49
F	–12.12	–3.75	–6.87	–9.16	–3.91	–6.70
G	–11.26	–4.06	–7.41	–8.43	–4.23	–7.27
H	N/A	N/A	N/A	–8.90	–3.75	–7.04
I	N/A	N/A	N/A	–8.24	–4.41	–7.37
X	–11.48	–3.99	–7.27	–8.64	–3.99	–7.18
Y	–11.80	–3.87	–7.07	–9.13	–3.87	–6.74

3.5.2 Configuration of the most stable interstitials in MoAlB and Fe_2AlB_2

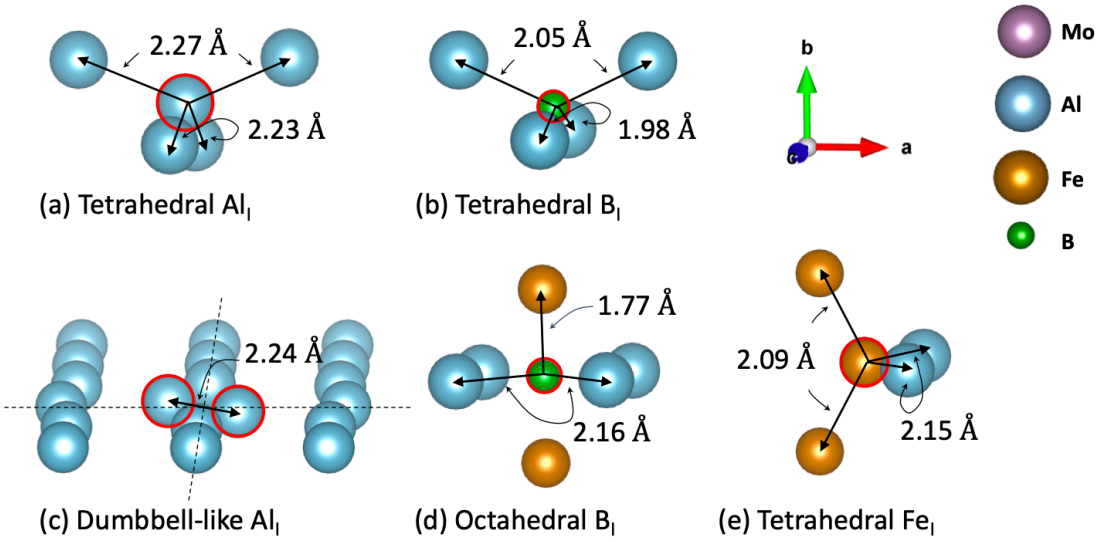

Figure 3.S1 Schematics of the most stable interstitial sites in MoAlB and Fe_2AlB_2 with the interatomic distances shown: (a) Al_I in MoAlB, (b) B_I in MoAlB, (c) Al_I in Fe_2AlB_2, (d) B_I in Fe_2AlB_2, (e) Fe_I in Fe_2AlB_2. Note that Mo_I does not exist because Mo_I is unstable and forms Mo_{Al} and Al_I (see Table 3.1).

CHAPTER 4

DEFECT CHEMISTRY

The study in this chapter has been published as: "Defect chemistry of Cr-B binary and Cr-Al-B MAB phases: effects of covalently bonded B networks" *Physical Review Materials* 5, 113603 (2021).

4.1 Introduction

Binary transition metal borides (TMBs) have been shown to exhibit many outstanding properties due to the presence of covalently bonded B networks bonded to transition metals. These properties include high melting point, high decomposition temperature, and high hardness and strength[13,14]. However, applications of binary TMBs have been limited because of their poor tolerance to oxidation and thermal shock as well as intrinsic brittleness and poor machinability[142]. Recently, layered ternary TMBs called MAB phases (M: transition metal, A: group III-A elements, B: B) have been found to exhibit excellent properties such as hardness[27,48], thermal and electrical conductivities[53,54], magnetocaloric effect[43], oxidation resistance[39,143], and radiation tolerance[144]. Moreover, MBenes, exfoliated from bulk MAB phases, have emerged as promising two-dimensional materials in applications such as spintronic devices[74].

To make use of and to control the outstanding properties of the TMBs, one has to take into account defects because a finite concentration of defects always exists and often governs material properties. For instance, the deintercalation of Al, a proposed pathway to the exfoliation of MBenes from MAB phases, involves the formation of stacking faults[145]. In the field of nuclear reactor applications, it has been recently reported that unstable Mo_I in MoAlB creates Mo_{Al} antisites that cannot be recovered easily and lead to the poor tolerance of this particular MAB phase to radiation-induced amorphization[144]. In integrated circuits, where Cr-B binaries can be used as diffusion barriers[146], understanding defect

behavior is also critical since impurity diffusion is often vacancy mediated[147].

The goal of this chapter is to bring insights into how the stability and concentrations of defects depend on the atomic structure in TMBs. In particular, I have chosen three binary Cr-B systems (CrB, Cr_3B_4, Cr_2B_3) and three Cr-Al-B MAB phases (Cr_2AlB_2, Cr_3AlB_4, Cr_4AlB_6). These TMBs have been chosen for a few different reasons. First of all, Cr-B systems have been used for high-temperature applications, including diffusion barriers in integrated circuits[146] and wear-resistant coatings[127]. Secondly, varying the composition while keeping the elements the same allows me to study how the defect stability depends on the different B networks, with the goal of extracting more general rules. Specifically, as depicted in Fig. 4.1, B atoms in CrB and Cr_2AlB_2 form one-B-chain layers, Cr_3B_4 and Cr_3AlB_4 contain one-B-ring layers (two B chains bonded), whereas Cr_2B_3 and Cr_4AlB_6 have two-B-ring layers (three B chains bonded). Cr_2AlB_2, Cr_3AlB_4, and Cr_4AlB_6 are similar to CrB, Cr_3B_4, and Cr_2B_3, respectively, except for the addition of the Al layers interleaving the Cr-B units. This set of the six TMBs provides a testbed for understanding the effects of the type of B network (i.e., one-B-chain vs. one-B-ring vs. two-B-ring) on the formation of defects. In this chapter, I use density functional theory (DFT) to investigate the defect chemistry in the six TMBs and the effects of the atomic structure on the formation energies and concentrations of defects.

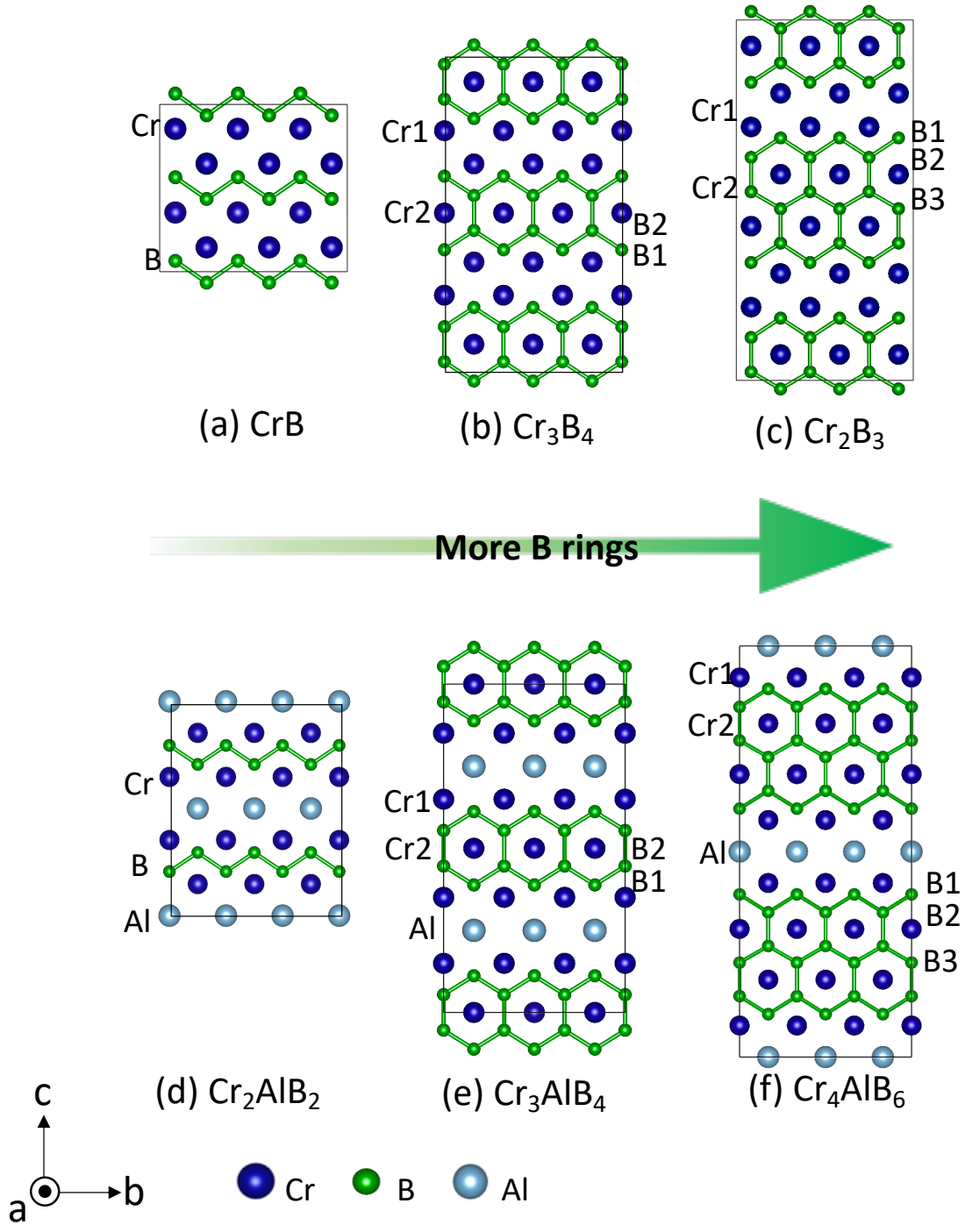

Figure 4.1 Supercell for (a) CrB, (b) Cr_3B_4, (c) Cr_2B_3, (d) Cr_2AlB_2, (e) Cr_3AlB_4, and (f) Cr_4AlB_6.

4.2 Methods

DFT calculations were performed using the Vienna Ab-initio Simulation Package[110] with the projector augmented wave[127] and the generalized gradient approximation by Perdew, Burke, and Ernzerhof[99]. The plane-wave cutoff energy of 400 eV and the energy tolerance of 0.5 meV/atoms were used. For the six systems, different Monkhorst-Pack *k*-point mesh sizes were used to optimize the geometry[128]: CrB, Cr_3B_4, Cr_2AlB_2 (7×7×5) and Cr_2B_3, Cr_3AlB_4, Cr_4AlB_6 (9×9×3). The total energies of perfect structures as well as the energies of structures containing either a vacancy or an antisite were calculated in 3×3×2 supercells for CrB, Cr_3B_4, Cr_2AlB_2, and Cr_3AlB_4 and 3×3×1 supercells for Cr_2B_3 and Cr_4AlB_6. Interstitial calculations required bigger supercells, which were determined based on the results of convergence tests. To take into account the magnetic properties of Cr-(Al)-B systems[148], magnetic moment was included in the DFT calculations.

The enthalpy of formation H_f for a defect is calculated as

$$H_f = [E_d + \Delta H_d(T, p^0)] - \left[E_p + \Delta H_p(T, p^0)\right] - \sum_i n_i \mu_i\,(T), \tag{4.1}$$

where the subscripts *d* and *p* denote defective and perfect crystals, respectively, and E is the total energy at 0 K. ΔH is the change in enthalpy at the standard pressure, which is approximately identical in a defective system and a perfect system and thus assumed to be canceled out. In addition, the change in volume due to the formation of a defect is assumed to be negligible. In Eq. (4.1), n_i is the number of atoms removed or added when introducing a defect, and the chemical potential μ_i is calculated using the following equation:

$$\mu_i(T) = \mu_i^{\mathrm{ref}} + \Delta\mu_i + \Delta H_i(T, p^0). \tag{4.2}$$

Here, μ^{ref} is the reference chemical potential obtained from a bulk system at 0 K, ΔH is the change in enthalpy at the standard pressure obtained from the JANAF thermochemical tables[149], and $\Delta\mu$ is the change in the chemical potential with respect to its reference state. I provided $\Delta\mu$ values for Cr- and B-rich conditions in Section 4.5.1 and I also fixed $\Delta\mu$ of Al at the Al-rich condition ($\Delta\mu_{\mathrm{Al}} = 0$), based on the

information that MAB phases are synthesized in Al-rich conditions[27]. The enthalpy of formation H_f is used to calculate the defect concentration (c) using the following equation,

$$c = N_d \exp\left(-\frac{G_f}{k_B T}\right) = N_d \exp\left(-\frac{H_f - TS_f}{k_B T}\right), \quad (4.3)$$

where N_d is the number of available sites for the formation of a given defect per unit volume, k_B is the Boltzmann constant, and S_f is the entropy of formation. The entropy calculation is costly, especially for the large systems (e.g., Cr_2B_3 and Cr_4AlB_6) and for the calculation of interstitials, which require large supercell sizes based on the convergence tests. Previous studies have shown that experimental and theoretical results for the entropy of formation of a point defect typically range from 0 to $10k_B$, and therefore the entropy term S_f has been often neglected when calculating the concentrations of point defects[150–154]. In addition, here, I compared the Gibbs free energy of formation and the enthalpy of formation for selected defects and I found the difference between the Gibbs free energy and the enthalpy to be smaller than 0.03 eV. In my calculation, I also found that the entropy contribution is negligible relative to the enthalpy difference even at elevated temperatures. For the entropy calculations, I used *phonopy*, an open source package for phonon calculations[155–157].

To investigate the role of the strength of chemical bonds, in this chapter I calculate the bond separation energy at 0 K. This is done by subtracting the energy of a perfect unit cell from the energy of a unit cell where a vacuum region of 2 nm thickness is inserted between the layers and finally by dividing the energy difference by the number of surface atoms. For the bond separation energy calculations, atoms were not relaxed. Using a finite-displacement scheme, I also calculated dynamical matrices, from which I extracted interatomic force constants.

4.3 Results and discussion

4.3.1 Types of defects and formation energies

The calculated lattice constants (a, b, c) of each system are: CrB (2.90 Å, 2.89 Å, 7.72 Å), Cr_3B_4 (2.88 Å, 2.92 Å, 12.88 Å), Cr_2B_3 (2.90 Å, 2.93 Å, 17.98 Å), Cr_2AlB_2 (2.91 Å, 2.90 Å, 10.86 Å), Cr_3AlB_4

(2.91 Å, 2.92 Å, 7.98 Å), and Cr_4AlB_6 (2.91 Å, 2.93 Å, 21.01 Å). All of these are in good agreement with reported experiments[27,158]. The formation enthalpy of each system was calculated to be: CrB (−1.72 eV/f.u.), Cr_3B_4 (−5.67 eV/f.u.), Cr_2B_3 (−3.95 eV/f.u.), Cr_2AlB_2 (−3.95 eV/f.u.), Cr_3AlB_4 (−6.16 eV/f.u.), and Cr_4AlB_6 (−8.69 eV/f.u.). These values were used to determine the change in the chemical potential with respect to its reference state at Cr- and B-rich conditions.

While vacancy and antisite defects are located at lattice sites, several different off-lattice sites are found for stable interstitials. Figure 4.2 shows the types of the most stable interstitials. The interstitial types that are less stable are depicted in Section 4.5.2, and the defect formation energies are provided in Section 4.5.3. In CrB, the only stable site for Cr_I was found at the center of a tetrahedron composed of four Cr atoms outside B-chain layers (Type 1 in Fig. 4.2). B_I in CrB forms two types of B bridges: the more stable type (Type 2 in Fig. 4.2) involves the interstitial connecting two different B chains and the other interstitial type (Type 9 in Section 4.5.2) bonds with two B atoms within a B chain. In Cr_3B_4 and Cr_2B_3, as shown in Fig. 4.1, there are different inequivalent lattice sites within a unit cell where V_{Cr} and V_B can form (Cr1, Cr2, B1, B2, and/or B3). Both V_{Cr} and V_B are found to have lower formation energies when forming within B-ring layers. The most stable V_{Cr} and V_B, respectively, are V_{Cr2} and V_{B2} in Cr_3B_4 and V_{Cr2} and V_{B3} in Cr_2B_3. For Cr_I in Cr_3B_4 and Cr_2B_3, the most stable interstitials were found within B-ring layers. As shown in Fig. 4.2, the most stable Cr_I in Cr_3B_4 forms a Cr dumbbell aligned along the *b*-axis within B-ring layers (Type 7), and the most stable Cr_I in Cr_2B_3 forms in-between two B3 atoms (Type 8 in Fig. 4.2). In Cr_3B_4 and Cr_2B_3, Type 2 was found as the most stable B_I in each system, while Type 9 (see Section 4.5.2) was found only in Cr_3B_4. B_I is also found to form within B-ring layers of Cr_3B_4 and Cr_2B_3, but their formation energies are higher than the most stable B_I in the respective system, at least by 0.7 eV (see Section 4.5.3).

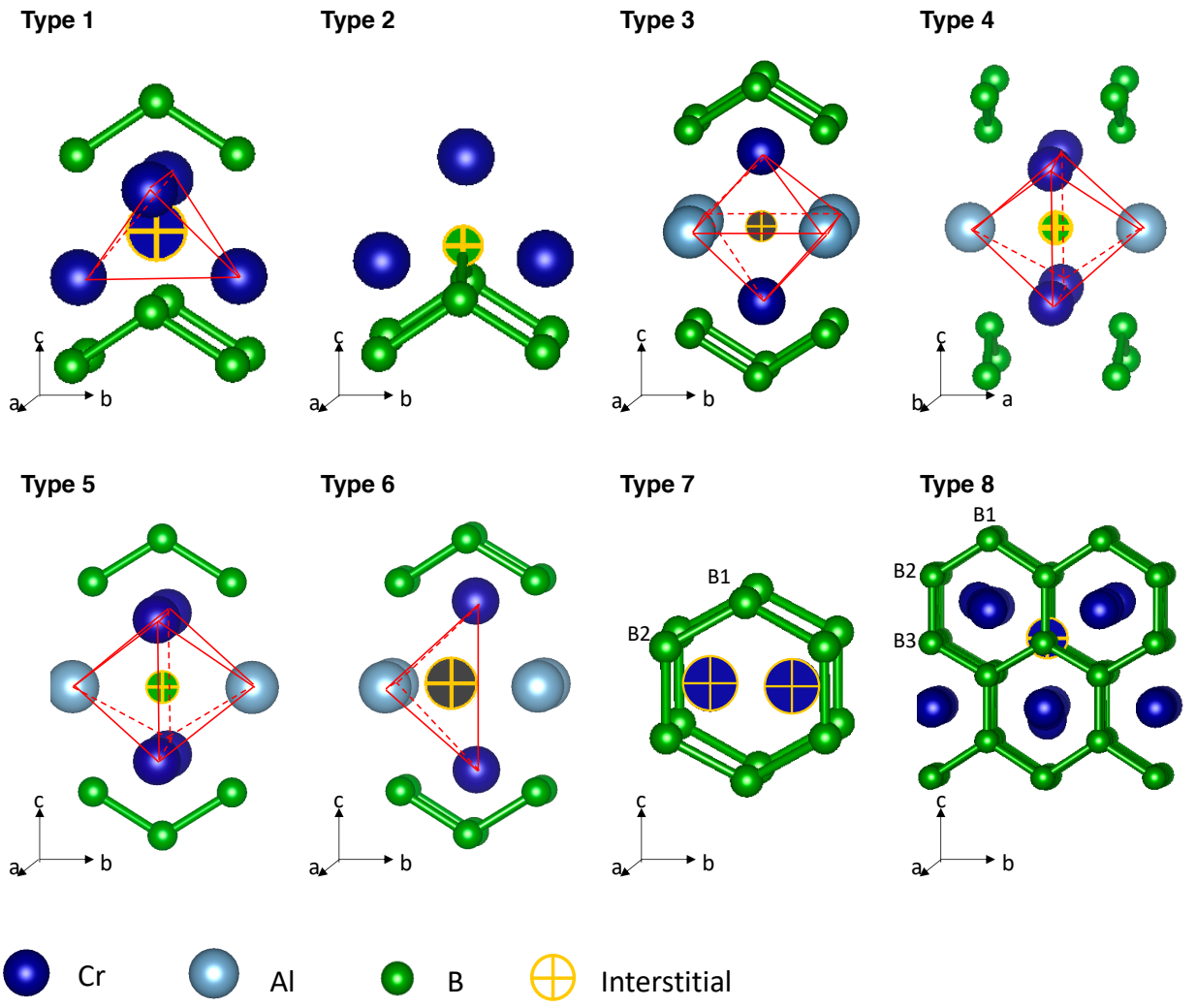

Figure 4.2 Types of the most stable interstitials in binary and ternary TMBs.

In Cr_2AlB_2, the only stable configuration of Cr_I was found at the center of an octahedron composed of two Cr atoms and four Al atoms (Type 3 in Fig. 4.2), and the most stable Al_I was found at the center of an octahedron composed of two Al atoms and four Cr atoms (Type 4 in Fig. 4.2). In Cr_2AlB_2, three types of B_I were found within Al layers as shown in Fig. 4.2: at the center of an octahedron composed of four Al atoms and two Cr atoms (Type 3), at the center of an octahedron composed of two Al atoms (aligned along the *a*-axis) and four Cr atoms (Type 4), and at the center of an octahedron composed of two Al atoms (aligned along the *b*-axis) and four Cr atoms (Type 5). Among the three types of B_I, Type 4 is the most stable. In Cr_3AlB_4 and Cr_4AlB_6, similarly to the corresponding binaries, the

most stable vacancies are V_{Cr2} and V_{B2} in Cr_3AlB_4 and V_{Cr2} and V_{B3} in Cr_4AlB_6, all of which form within B-ring layers. In Cr_3AlB_4 and Cr_4AlB_6, the most stable Cr_I forms within Al layers at the center of a tetrahedron composed of two Cr atoms and two Al atoms (Type 6 in Fig. 4.2). Although Cr_I is also found within B-ring layers in Cr_3AlB_4 and Cr_4AlB_6, their formation energies are much higher than that of Type 6 (see Section 4.5.3). Al_I is similar – the most stable Al_I was found within Al layers (Type 6 in Fig. 4.2) and are stable much more than the other Al_I found within B-ring layers (see Section 4.5.3). As for B_I in Cr_3AlB_4 and Cr_4AlB_6, they are similar to B_I in Cr_2AlB_2. The stable B_I is found in Al layers at the center of an octahedron as shown in Fig. 4.2: Type 3, Type 4, and Type 5. The formation energies of B_I found within B-ring layers are much higher than those of the three types of B_I found in Al layers (see Section 4.5.3).

To summarize, in CrB where B atoms form B chains, V_{Cr} and V_B are allowed to form only at one site for each species, whereas in the systems where B atoms form B rings (Cr_3B_4 and Cr_2B_3) the most stable V_{Cr} and V_B form within the B-ring layers. As for interstitials in the binaries, the only Cr_I in CrB is found outside the B-chain layers (Type 1 in Fig. 4.2), while the most stable Cr_I is found within the B-ring layers in Cr_3B_4 and Cr_2B_3. In the binaries, the most stable B_I is all found to form a B bridge (Type 2 in Fig. 4.2). For the ternaries, in Cr_2AlB_2 (which has B-chain layers), V_{Cr} and V_B form only at one site for each of the species, whereas in the systems that have B-ring layers (Cr_3AlB_4 and Cr_4AlB_6) the most stable V_{Cr} and V_B form within the B-ring layers. All the most stable interstitials in the ternaries are found within Al layers. As such, the types of defects created are different in the six TMBs and they are associated with the types of B networks. Therefore, for applications of the TMBs, it is critical to understand the dependence of the defect formation on the type of B networks in the binary Cr-B systems and the ternary Cr-Al-B MAB phases. Here, I will investigate the question of how the defect formation energies and the defect concentrations change with increasing the number of B rings.

The formation energies of the most stable point defects and Frenkel pairs (FPs) at 0 K and 300 K are plotted as a function of the chemical potential in Fig. 4.3. I also provided the concentrations of the defects in Section 4.5.4 and N_d used to calculate the concentrations in Section 4.5.5. For the ternary

systems, the defect formation energies were calculated at the Al-rich conditions because Cr-Al-B MAB phases are synthesized in Al-rich environments[27]. For each type of defect, the defect with the lowest formation energy is found to be the defect with the highest concentration.

4.3.2 Effects of B networks on defect formation energies

To investigate the effects of the type of B network on the defect formation energies, I compare the formation energies of defects in the binaries first (CrB, Cr_3B_4, Cr_2B_3), focusing on the most stable vacancies, antisites, interstitials and FPs. Figures 4.3(a)-(c) shows that the defect formation energies of V_B (red) and V_{Cr} (blue) decrease from CrB to Cr_3B_4 and to Cr_2B_3, which is the order of increasing the number of B rings (i.e., from B-chain to one-B-ring, and to two-B-ring). The defect formation energies plotted for V_B correspond to V_{B2} in Cr_3B_4 and V_{B3} in Cr_2B_3, and the defect formation energies plotted for V_{Cr} correspond to V_{Cr2} for both Cr_3B_4 and Cr_2B_3. The decrease in defect formation energy of V_B and V_{Cr} is attributed to the weakening of the strongest Cr-B bond from CrB to Cr_3B_4 and to Cr_2B_3. Kádas *et al.* have previously shown that the M-B bond is the strongest bond in M_2AlB_2 (M = Cr, Mn, Fe, and Co) systems. The authors have also found that the work of separation can be used as a reliable measure of the bond strength in MAB phases[34]. For that reason and because of the computational efficiency of the approach, here I also use the work of separation to determine qualitative trends in the bond strengths in Cr-B and Cr-Al-B systems. The work of separation is calculated using DFT, and the results are shown in Table 4.1. The work of separation for the Cr-B bonds in CrB is 6.33 eV (Cr1-B1 in Table 4.1), in Cr_3B_4 it is 5.44 eV (Cr2-B2), and in Cr_2B_3 it is 5.30 eV (Cr2-B2) and 5.11 eV (Cr2-B3). This data shows that, when B networks contain more B rings (from B-chain to one-B-ring, and to two-B-ring), the Cr-B bonds (the strongest bond in the systems) is weakened, and consequently V_{Cr} and V_B are easier to form.

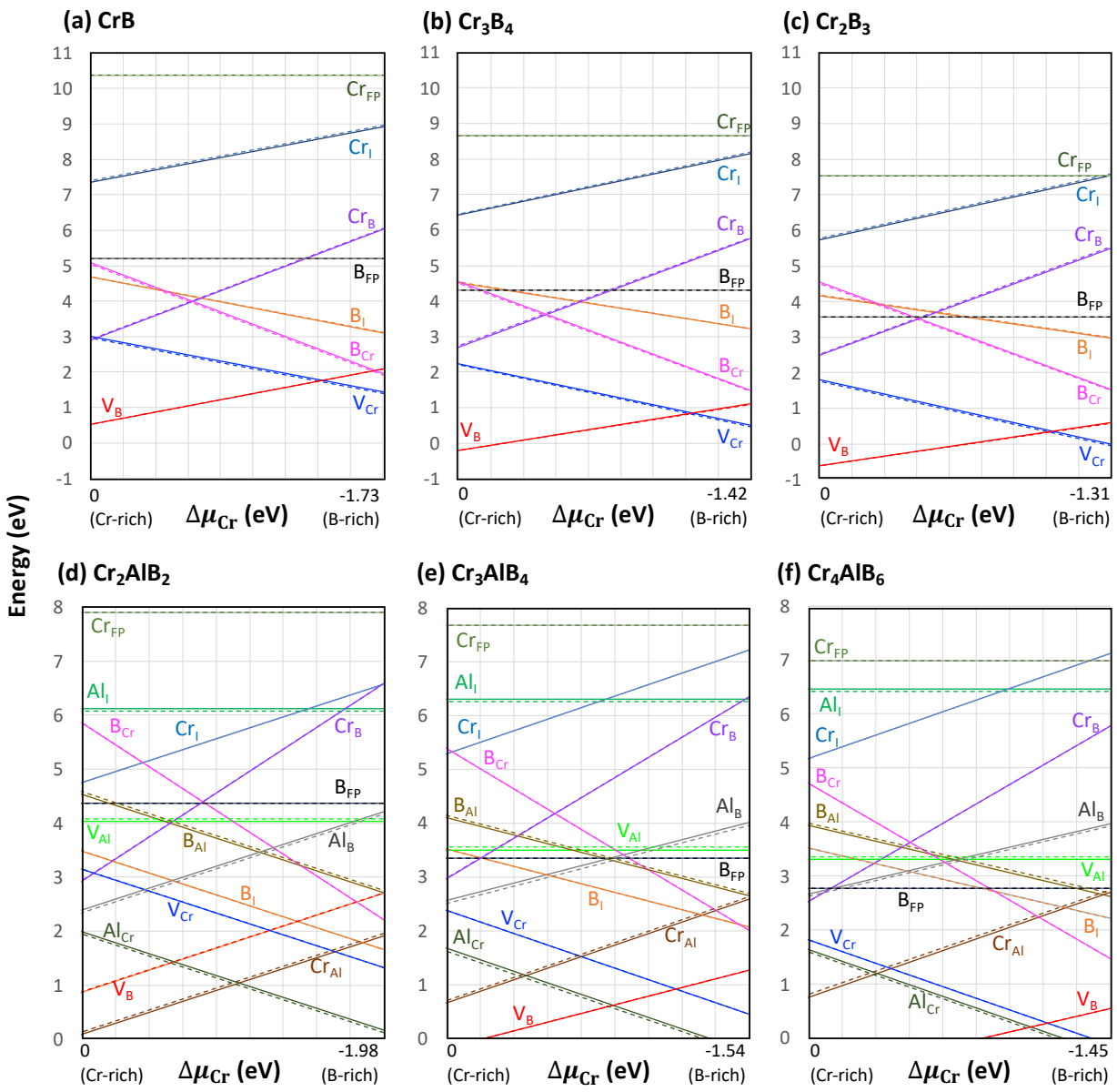

Figure 4.3 Defect formation energies at 0 K (bold) and 300 K (dashed) in (a) CrB, (b) Cr_3B_4, (c) Cr_2B_3, (d) Cr_2AlB_2, (e) Cr_3AlB_4, and (f) Cr_4AlB_6.

Table 4.1 Bond separation energy in the six TMBs shown in Fig. 4.1.

	Bond separation energy (eV)					
	CrB	Cr_3B_4	Cr_2B_3	Cr_2AlB_2	Cr_3AlB_4	Cr_4AlB_6
Cr1-Cr1[†]	4.38	4.21	4.14	N/A	N/A	N/A
Cr1-B1[†]	6.33	6.03	6.19	6.24	5.86	6.10
B1-B2[†]	4.82	4.99	4.96	5.05	5.19	5.14
Cr1-Al	N/A	N/A	N/A	3.33	3.37	3.42
Cr2-B2	N/A	5.44	5.30	N/A	5.57	5.41
Cr2-B3	N/A	N/A	5.11	N/A	N/A	5.01
B3-B3	N/A	N/A	5.25	N/A	N/A	5.29

[†]Cr1 for CrB and Cr_2AlB_2 denotes Cr, and B1 and B2 for CrB and Cr_2AlB_2 denote B, as depicted in Fig. 4.1(a) and (d).

As shown in Figs. 4.3(a)-(c), the defect formation energies of Cr_I (sky-blue) in the binaries decrease with increasing the number of B rings. In CrB, the only stable site for Cr_I is at the center of a tetrahedron composed of four Cr atoms (Type 1 in Fig. 4.2) outside the B-chain layers. In Cr_3B_4, the most stable Cr_I forms a Cr dumbbell on Cr2 sites (Type 7 in Fig. 4.2), and in Cr_2B_3, the most stable Cr_I forms in-between two B3 atoms (Type 8 in Fig. 4.2). Note that Cr_I in Cr_3B_4 and Cr_2B_3 is found within B-ring layers. The decrease in the defect formation energy of Cr_I in Figs. 4.3(a)-(c) is due to the softness of the bonds associated with Cr2 atoms positioned within the B-ring layers, which helps accommodate interstitials more easily. To show this, I plotted the force constants of Cr1 and Cr2 in each system. The force constant in the in-plane direction is defined as the average of the force constants along the b- and c-axes, and the out-of-plane direction constant is defined as the constant along the c-axis (the axes are indicated in Fig. 4.1). The force constants for Cr2 are much lower than those for Cr1 in the binary TMBs. This trend indicates that Cr2 atoms relax easier than Cr1 atoms do, which allows the systems having Cr2 atoms (and hence, having B-ring layers) to accommodate interstitials with a lower energy cost. As for the B_I in the binaries, the defect formation energies of B_I (orange) change only little over the different systems, because B_I shares the same type of B-bridge structure (Type 2 in Fig. 4.2), and the distances between the B_I and the nearest B atom differ only with the standard deviation of 0.01 Å.

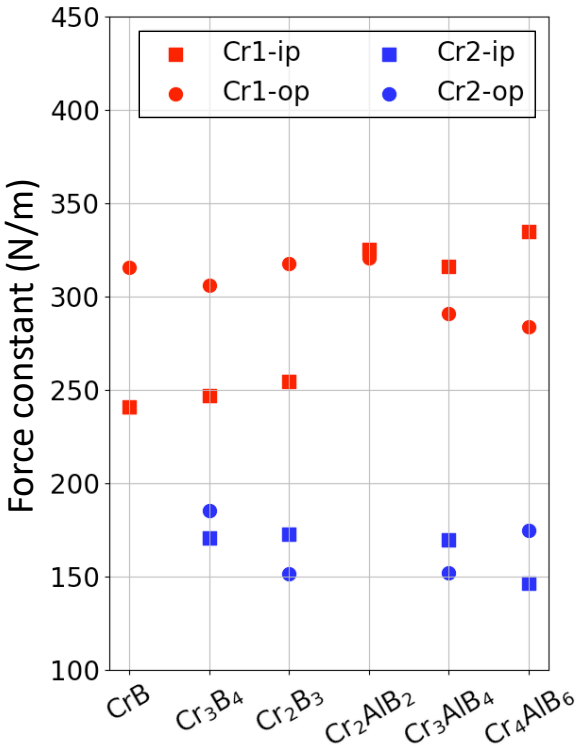

Figure 4.4 Force constants of Cr1 and Cr2 in the in-plane direction (ip) and out-of-plane direction (op).

As mentioned in the introduction, Cr_2AlB_2 (B-chain), Cr_3AlB_4 (one-B-ring), and Cr_4AlB_6 (two-B-ring) are similar in structure to CrB, Cr_3B_4, and Cr_2B_3, respectively, except for the addition of the Al layers. Here, I compare the formation energies of defects in the ternaries and investigate the effects of the number of B rings. The formation energies of defects in Cr_2AlB_2, Cr_3AlB_4, and Cr_4AlB_6 are plotted in Figs. 4.3(d)-(f). For V_{Cr} and V_B, I found the same trend as in the binary systems. The formation energies of V_{Cr} (blue) and V_B (red) in Figs. 4.3(d)-(f) decrease with increasing the number of B rings (from Cr_2AlB_2 to Cr_3AlB_4 and to Cr_4AlB_6), and this trend can be attributed to the weakening of the Cr-B bonds. This weakening is evidenced by the calculated bond separation energy: the Cr-B bond separation energy relevant to the formation of V_{Cr} and V_B in Cr_2AlB_2 is 6.24 eV (Cr1-B1), whereas in Cr_3AlB_4 it is 5.57 eV (Cr2-B2) and in Cr_4AlB_6 it is 5.41 eV (Cr2-B2) and 5.01 eV (Cr2-B3). The defect formation energy of V_{Al} (lime) was also found to decrease with increasing the number of B rings.

The most stable Cr_I, Al_I, and B_I in the ternaries were all found within Al layers. This is because of the softness of Al layers, whose in-plane force constants (determined as the average of the a-axis and the b-axis constants) range from 115 to 118 N/m over the three ternaries. These force constants are even lower than those of Cr2 atoms in B-ring layers (See Fig. 4.4), which is why the most stable interstitials form within the Al layers in the ternaries rather than in the B-ring layers. The defect formation energies of Cr_I, Al_I, and B_I in Cr_3AlB_4 and Cr_4AlB_6 are slightly higher than those in Cr_2AlB_2. This higher formation energy can be explained by the differences in the thickness of the Cr-Al-Cr layers where the interstitials are accommodated. Zhao *et* al. pointed out that a bigger interlayer spacing in MAX phase Ti_3AlC_2 provides interstitials with more stable sites, leading to a lower formation energy as compared with MAX phase Ti_3SiC_2[118]. In the case of MAB phases studied here, my DFT calculations show that in the relaxed undefected structures, the interlayer spacing of Cr-Al-Cr (where the interstitials would reside) is 3.27 Å (Cr_2AlB_2), 3.21 Å (Cr_3AlB_4), and 3.22 Å (Cr_4AlB_6). The interlayer spacings of Cr_3AlB_4 and Cr_4AlB_6 are slightly smaller than that of Cr_2AlB_2, which is consistent with the higher formation energies of the interstitials in Cr_3AlB_4 and Cr_4AlB_6.

To summarize, in the binaries, increasing the number of B rings in the structure leads to the lower formation energies (and hence the higher concentrations) of V_B, V_{Cr}, and Cr_I, whereas the formation energies of B_I are not significantly affected. This trend suggests the easier formation of FPs and the increase in the concentrations of B FPs and Cr FPs in the binaries with B-ring layers (Figs. 4.3(a)-(c)). In the ternaries, increasing the number of B rings is associated with the significant decreases in the formation energies (and hence increases in the concentrations) of vacancies and the slight increases in the interstitial formation energies (see Figs. 4.3(d)-(f)). Therefore, the easier formation of FPs and the corresponding increase in the concentrations of the FPs are expected with increasing the number of B rings. These trends indeed are found in my data, as shown in Figs. 4.3(d)-(f).

It is interesting to consider how the effects of B networks on the defect formation energy and the concentration could relate to applications of the TMBs. In integrated circuit applications, for diffusion barriers to prevent Cu atoms from diffusing out, the barrier metals should have a high diffusion energy

barrier or a high vacancy formation energy (low concentration)[147]. Based on my results, the vacancy formation energies are lower (the defect concentrations are higher) when a system has more B rings. This result implies that Cr_3B_4, Cr_2B_3, Cr_3AlB_4, and Cr_4AlB_6 contain more vacancies via which Cu atoms can diffuse and that, at least based on the defect concentrations, CrB and Cr_2AlB_2 might be more effective as diffusion barrier materials. For nuclear reactor applications, understanding defect behavior is critical. Under irradiation, a large number of FPs are created, and material's tolerance to radiation-induced amorphization largely depends on how many defects are created and how many of them are removed through defect recovery processes[144]. The radiation-induced defect recovery process involves complex processes, understanding of which requires formation energies as the first step. For example, in this chapter, I found that the most stable B_I and V_B in Cr_2B_3 and Cr_4AlB_6 are separated spatially from each other. That could potentially lead to a non-negligible energy barrier to recombination and could contribute to the accumulation of radiation-induced damage. Kinetics of defects needs to be further investigated to ultimately determine their impact on the recovery process. The defect chemistry data discussed in this chapter, combined with future studies of kinetics, will be important for boride applications including diffusion barriers and nuclear reactor applications.

4.4 Conclusions

I investigated the defect chemistry in CrB, Cr_3B_4, Cr_2B_3, Cr_2AlB_2, Cr_3AlB_4, and Cr_4AlB_6 by calculating the defect formation energies and the concentrations of point defects and FPs using DFT. I discussed the effects of the B networks on the defect formation energies and the defect concentrations. From CrB (Cr_2AlB_2) to Cr_3B_4 (Cr_3AlB_4), and to Cr_2B_3 (Cr_4AlB_6), the number of B rings increases. At the same time, the vacancy formation energies decrease, which can be attributed to the weakening of the Cr-B bonds. With increasing the number of B rings, the defect formation energies of Cr_I also decrease in the binary systems, because Cr atoms within B-ring layers form bonds that are softer than Cr atoms outside the B-ring layers. As a result, the B-ring layers can accommodate interstitials with a lower energy cost. The defect formation energies of B_I in the binary systems showed insignificant changes, and the defect

formation energies of all the interstitials in the ternary systems showed a slight decrease with the number of B rings. Based on my results it can be concluded that increasing the number of B rings leads to the lower defect formation energies and thus the higher concentrations of FPs in the binary and ternary systems. This work lays a foundation and is the necessary first step toward understanding defect-related properties of binary borides and ternary MAB phases.

4.5 Supplementary Information

4.5.1 Change in the chemical potential ($\Delta\mu$) at the Cr- and B-rich conditions.

Table 4.S1 Change in the chemical potential at the Cr- and B-rich conditions for the binaries.

eV	CrB		Cr_3B_4		Cr_2B_3	
	Cr-rich	B-rich	Cr-rich	B-rich	Cr-rich	B-rich
$\Delta\mu_{Cr}$	0	-1.73	0	-1.90	0	-1.97
$\Delta\mu_{B}$	-1.73	0	-1.42	0	-1.31	0

Table 4.S2 Change in the chemical potential at the Cr- and B-rich conditions for the ternaries (at the Al-rich condition, i.e., $\Delta\mu_{Al} = 0$).

eV	Cr_2AlB_2		Cr_3AlB_4		Cr_4AlB_6	
	Cr-rich	B-rich	Cr-rich	B-rich	Cr-rich	B-rich
$\Delta\mu_{Cr}$	0	-1.98	0	-2.10	0	-2.17
$\Delta\mu_{Al}$	0	0	0	0	0	0
$\Delta\mu_{B}$	-1.98	0	-1.54	0	-1.45	0

4.5.2 Structures of interstitials that are less stable than those shown in Fig. 4.2.

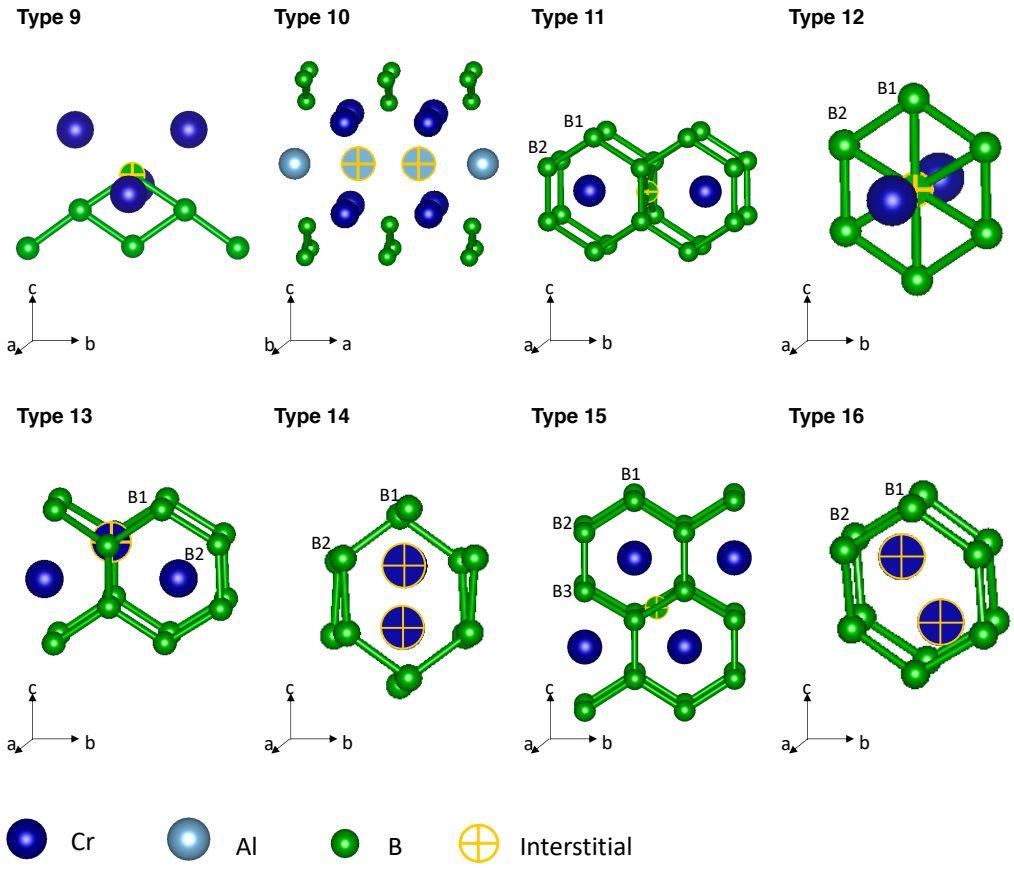

Figure 4.S1 Types of interstitials that are less stable than those shown in Fig. 4.2.

4.5.3 Defect formation energies of all the defects found in this chapter.

Table 4.S3 Defect formation energies referenced to the vacuum level ($E_d - E_p$) of all the defects found. The type of interstitial is indicated in parenthesis, and different types of interstitials are shown in Fig. 4.2 and Fig. 4.S1. "N/A" indicates that the system has no available site for the defect.

eV	CrB	Cr_3B_4	Cr_2B_3	Cr_2AlB_2	Cr_3AlB_4	Cr_4AlB_6
V_{Cr1}	12.71	12.17	12.14	12.87	12.11	12.09
V_{Cr2}	N/A	11.92	11.48	N/A	12.19	11.54
V_{Al}	N/A	N/A	N/A	7.78	7.25	7.05
V_{B1}	8.83	8.26	8.23	9.46	8.37	8.12
V_{B2}	N/A	7.83	7.70	N/A	8.02	7.80
V_{B3}	N/A	N/A	7.31	N/A	N/A	7.29
Cr_{I1}	−2.35 (1)	−2.60 (1)	−2.76 (1)	−4.97 (3)	−4.44 (6)	−4.56 (6)
Cr_{I2}	N/A	−2.20 (13)	−2.25 (13)	N/A	−2.17 (13)	−2.29 (13)
Cr_{I3}	N/A	−3.26 (7)	−3.20 (7)	N/A	−3.03 (7)	−3.28 (7)
Cr_{I4}	N/A	−2.80 (14)	−2.70 (14)	N/A	−2.24 (14)	−2.29 (14)
Cr_{I5}	N/A	N/A	−3.95 (8)	N/A	N/A	−3.79 (8)
Al_{I1}	N/A	N/A	N/A	2.37 (4)	2.56 (6)	2.71 (6)
Al_{I2}	N/A	N/A	N/A	N/A	7.73 (14)	N/A
Al_{I3}	N/A	N/A	N/A	N/A	N/A	7.25 (12)
Al_{I4}	N/A	N/A	N/A	N/A	N/A	4.61 (8)
B_{I1}	−3.63 (2)	−3.51 (2)	−3.75 (2)	−4.68 (3)	−4.64 (3)	−4.52 (3)
B_{I2}	−3.50 (9)	−3.29 (9)	N/A	−5.10 (4)	−4.67 (4)	−4.69 (4)
B_{I3}	N/A	N/A	N/A	−4.98 (5)	−4.62 (5)	−4.49 (5)
B_{I4}	N/A	−2.83 (11)	−2.96 (11)	N/A	−2.85 (11)	−2.80 (11)
B_{I5}	N/A	−1.90 (12)	−2.03 (12)	N/A	−2.33 (12)	−2.21 (12)
B_{I6}	N/A	N/A	−2.71 (15)	N/A	N/A	−2.55 (15)
Cr_{B1}	1.49	1.06	1.04	1.79	1.44	1.49
Cr_{B2}	N/A	1.91	1.58	N/A	2.76	1.79
Cr_{B3}	N/A	N/A	0.73	N/A	N/A	0.85
Cr_{Al}	N/A	N/A	N/A	−5.88	−5.32	−5.22
Al_{B1}	N/A	N/A	N/A	7.23	7.00	6.96
Al_{B2}	N/A	N/A	N/A	N/A	7.51	7.47
Al_{B3}	N/A	N/A	N/A	N/A	N/A	7.23
Al_{Cr1}	N/A	N/A	N/A	−7.96	8.08	8.28
Al_{Cr2}	N/A	N/A	N/A	N/A	7.66	7.62
B_{Al}	N/A	N/A	N/A	−0.30	−0.34	−0.36
B_{Cr1}	6.48	6.19	6.30	6.99	7.59	7.90
B_{Cr2}	N/A	6.91	6.48	N/A	6.92	6.41

4.5.4 Concentrations of the most stable point defects and FPs at 300 K.

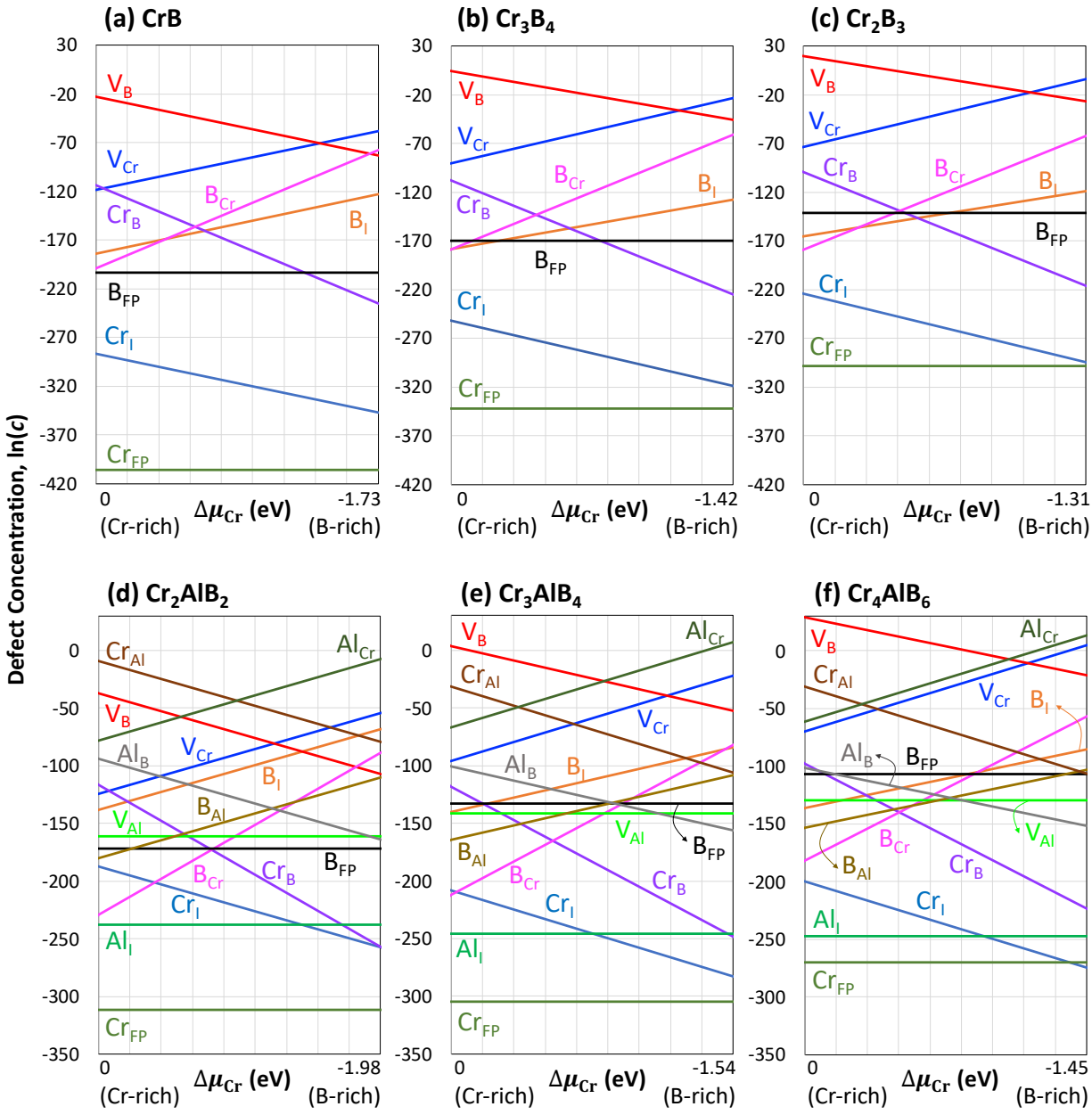

Figure 4.S2 Concentrations of the most stable point defects and FPs at 300 K in (a) CrB, (b) Cr_3B_4, (c) Cr_2B_3, (d) Cr_2AlB_2, (e) Cr_3AlB_4, and (f) Cr_4AlB_6.

4.5.5 Evaluation of N_d

Table 4.S4 Evaluation of available sites per unit volume for each defect (N_d), used to calculate the defect concentrations.

	N_d (#/Å^3)					
	CrB	Cr_3B_4	Cr_2B_3	Cr_2AlB_2	Cr_3AlB_4	Cr_4AlB_6
Cr_I	0.062	0.018	0.026	0.022	0.015	0.011
B_I	0.031	0.018	0.013	0.022	0.015	0.011
Al_I	N/A	N/A	N/A	0.022	0.015	0.011
V_{Cr}	0.062	0.018	0.013	0.044	0.015	0.022
V_B	0.062	0.037	0.026	0.044	0.029	0.022
V_{Al}	N/A	N/A	N/A	0.022	0.015	0.011
Cr_B	0.062	0.037	0.026	0.044	0.029	0.022
B_{Cr}	0.062	0.037	0.026	0.044	0.015	0.022
Al_{Cr}	N/A	N/A	N/A	0.044	0.015	0.022
Cr_{Al}	N/A	N/A	N/A	0.022	0.015	0.011
B_{Al}	N/A	N/A	N/A	0.022	0.015	0.011
Al_B	N/A	N/A	N/A	0.044	0.029	0.022

CHAPTER 5

DEFECT RECOVERY PROCESS

The experimental part in this chapter was carried out by Dr. Hongliang Zhang.

5.1 Introduction

Layered transition metal materials have drawn attention for many potential applications, including high-temperature heating elements, coatings for electrical contacts, and structural components in nuclear reactor applications. One of well-known examples is MAX phases, which have shown many outstanding properties, including thermal shock resistance[28], radiation tolerance[34,116,119,159], and oxidation resistance[115]. For instance, Ti-based MAX phases (e.g., Ti_3SiC_2 and Ti_3AlC_2) exhibit excellent resistance to radiation-induced amorphization, up to 25 displacements per atom (dpa) at room temperature (RT)[116]. A similar class of ternary borides are MAB phases [7,8], which have been shown to have high hardness[48], high decomposition temperature[60], good thermal and electrical conductivities[53,54,160], the large magnetocaloric effect[43], and good oxidation resistance[39,143,161]. Recently, two-dimensional borides, so-called MBenes, and MAB phases have been proposed for promising materials in future energy applications[162] and safe biological applications[75,163]. More recently, MAB phases have been proposed as promising materials for nuclear-related applications[144]. For instance, our previous experimental results showed that MAB phase Fe_2AlB_2 is as tolerant to radiation-induced amorphization as SiC, which is already considered for nuclear reactor applications. In addition, Fe_2AlB_2 does not undergo radiation-induced cracking, whereas radiation-induced cracking has been seen in the MAX phases of Ti_3SiC_2 and Ti_2AlC. Also, MAB phase MoAlB has shown a high neutron shielding capacity exhibiting strong resistance to crack formation and tolerance to radiation-induced amorphization under high temperature[144].

Resistance to radiation-induced amorphization depends largely on the ability of the material to anneal out or accommodate radiation-induced non-equilibrium defects[164]. Defect behavior is highly dependent on the structure of the material. For instance, in MAX phases, the A layer is known to provide stable sites where interstitials can be accommodated with a low-cost (i.e., low formation energy)[35,165]. In contrast to MAX phases, studies of defect kinetics in MAB phases are rare[27,144], and it is currently unknown how the specific structural features of MAB phases affect defect behavior.

In this chapter, we studied Cr-Al-B MAB phases and Cr-B binary phases, focusing on their resistance to radiation-induced amorphization. A schematic view of the atomic structures of the Cr-Al-B and Cr-B systems is shown in Fig 5.1. As shown in Figs. 5.1(a)-(c), the binary phases consist of B networks bonded with Cr layers, wherein the B networks may be one-B-chain (CrB), one-B-ring (Cr_3B_4), or two-B-ring (Cr_2B_3) types. Unlike the binary phases, the ternary phases have Al layers interleaving the B networks, which are similar to the corresponding binary phases: one-B-chain (Cr_2AlB_2), one-B-ring (Cr_3AlB_4), or two-B-ring (Cr_4AlB_6), as shown in Figs. 5.1(d)-(f). Like many other ultra-high temperature ceramics, the binary Cr-B phases have extreme hardness[13], high thermal and electrical conductivities[2,166], and high melting point[167]. The ternary Cr-Al-B phases have also exhibited outstanding properties, including high decomposition temperatures, hardness[27], electrical conductivity[54], magnetic properties[148], and oxidation tolerance[115]. The six systems considered in our study were specifically selected because they allow us to understand the effects of the Al layer (binary vs. ternary) and the effects of the B networks (one-B-chain vs. one-B-ring vs. two-B-ring) on the resistance to radiation-induced amorphization. To understand these effects, we performed irradiation experiments with CrB, Cr_3B_4, Cr_2AlB_2, Cr_3AlB_4, and Cr_4AlB_6 at 150 °C and 300 °C. The resulting crystal structures were analyzed using transmission electron microscopy (TEM), X-ray diffraction (XRD) and the corresponding Rietveld refinement of the diffraction patterns. The trends found in our experiments are explained based on density functional theory (DFT) calculations of defect migration energies and recombination barriers.

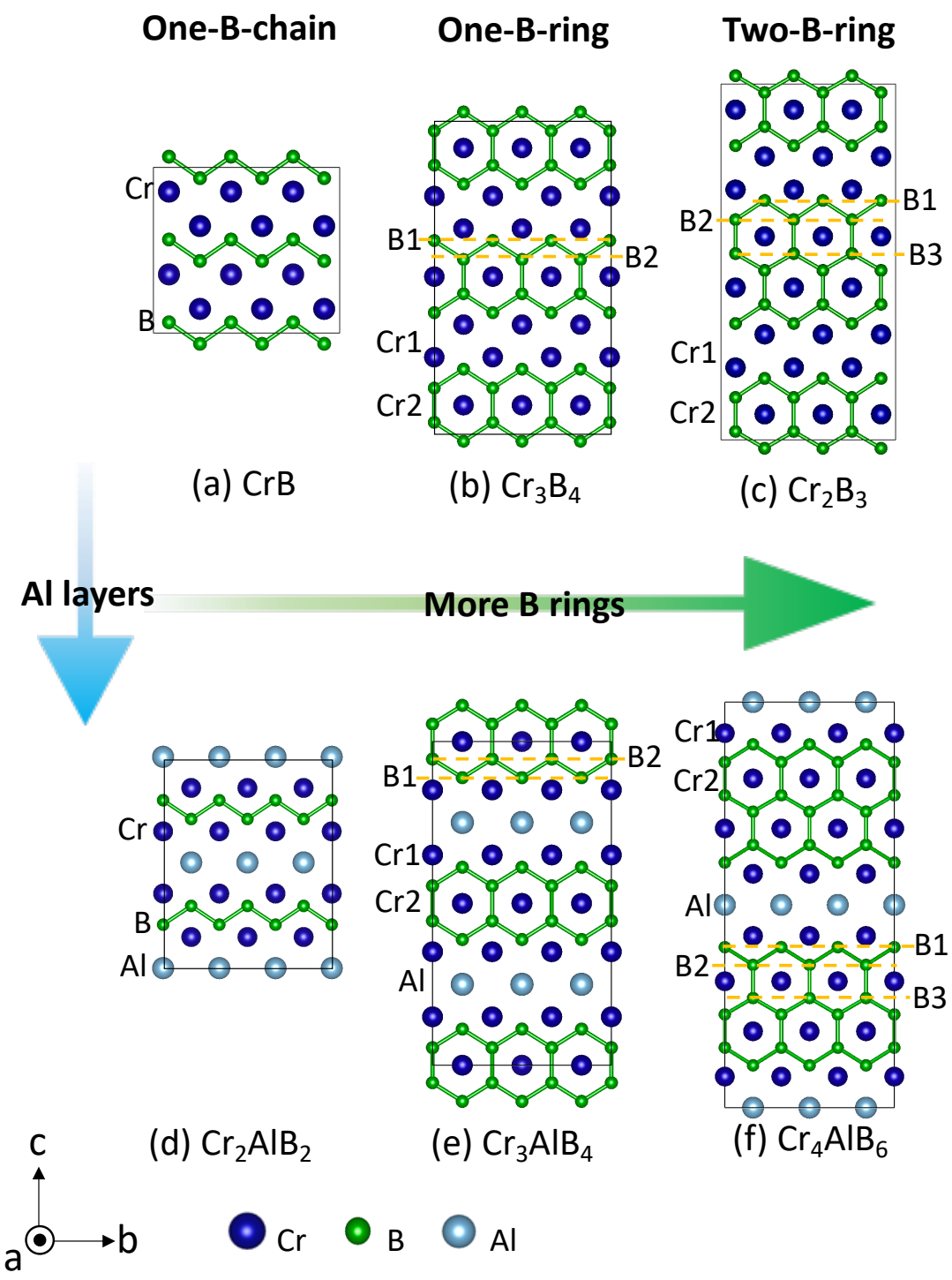

Figure 5.1 Atomic structure of (a) CrB, (b) Cr_3B_4, (c) Cr_2B_3, (d) Cr_2AlB_2, (e) Cr_3AlB_4, and (f) Cr_4AlB_6.

5.2 Methods

CrB powder (<45 μm), used as a precursor material for MAB phase synthesis, was produced in-house. No impurities were identified in the powders by XRD analysis. The CrB powder was mixed with Al powder (<45 μm, >99.7 %) and B powder (<1 μm, >95 %) in molar ratios of 2:1.7 (CrB:Al) for Cr_2AlB_2, 3:1.7:1 (CrB:Al:B) for Cr_3AlB_4, and 4:1.7:2 (CrB:Al:B) for Cr_4AlB_6. The 10 g powder mixtures were high-energy ball milled for 30 min using a hardened steel milling vial and balls in a SPEX 8000 M mixer/mill, with a ball to powder mass ratio of 7. The milled powders were loaded into an 18 mm diameter graphite die lined with BN-coated graphite foil and hot-pressed in a mullite tube under flowing argon. The heating and cooling rates were both 10 °C/min, the peak temperature was 1200 °C, and the dwell time was 60 min. The pressure was gradually applied during the final 30 min of the heating ramp, to the maximum of 50 MPa, and was removed upon the commencement of the cooling ramp. CrB and Cr_3B_4 were synthesized by the arc melting method. Cr and B powders were mixed in a ball mill and were pressed into bars and then sintered at >1600 °C. The sintered samples were arc-melted in an argon atmosphere. Each ingot was flipped and remelted more than 5 times to enhance the composition homogenization. Arc-melted samples were cooled on a water-cooled copper hearth. The as-cast samples were annealed at 1300 ℃ for 50 hours to form large grains (2-20 μm). Diamond grinding discs were used to remove residual graphite/BN on the outside of the pellets before grinding with SiC papers. The as-sintered specimens were all characterized using the Rigaku D/max 2500 XRD diffractometer, which adopts a Cu Kα source with a wavelength of 0.154 nm. A 2D detector, which has a 2θ resolution of 0.005°, was used to acquire the diffraction signals. Grazing incidence X-ray diffraction (GI XRD) was used for the characterization with an incident angle of 1.0°, a time of 600 sec per step, and a 2-theta range of 20-60º. As shown in Fig. 5.2, no impurity phase was found in the CrB, Cr_3B_4, Cr_2AlB_2, Cr_3AlB_4, and Cr_4AlB_6 bulk samples. We also attempted to synthesize Cr_2B_3, however, we found that this phase is unstable at RT. All the specimens were polished using fine metallographic abrasive papers and Al_2O_3

suspensions, cleaned by rinsing in ultrasonic baths of acetone and ethanol, and annealed at 600 °C in a vacuum environment of 5 $\times 10^{-5}$ Pa for 1 hour to release residual stress.

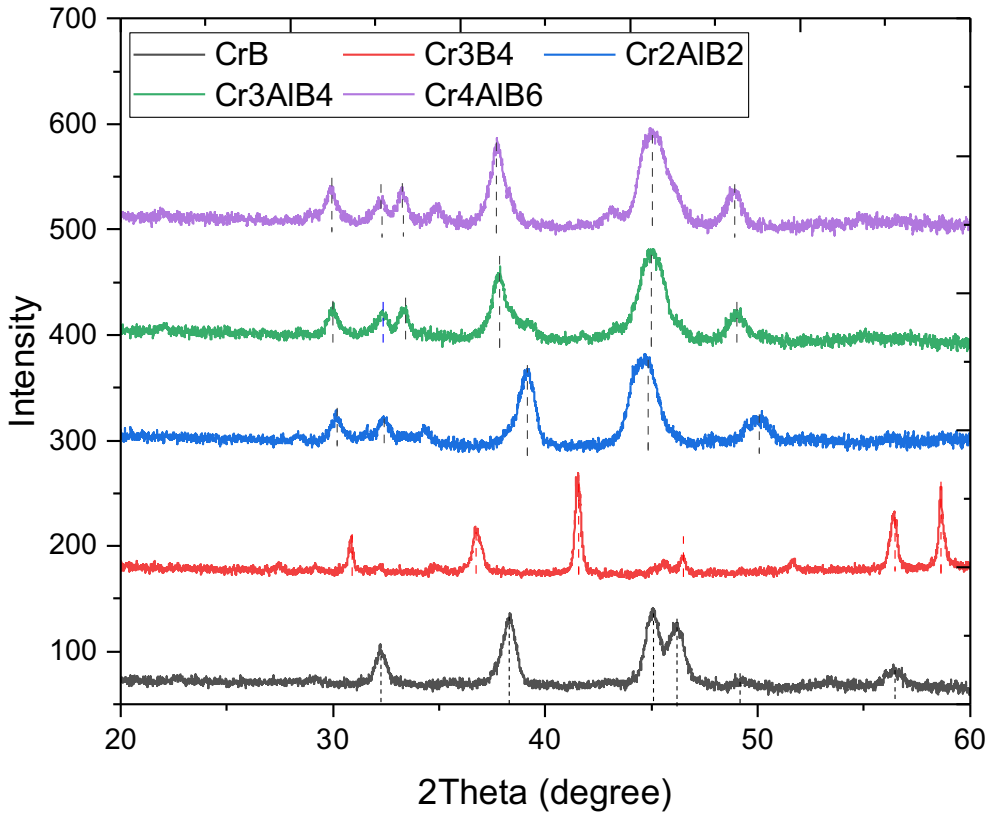

Figure 5.2 GI XRD of unirradiated Cr_2AlB_2, Cr_3AlB_4, Cr_4AlB_6, CrB, and Cr_3B_4 at the incident angle of 1.0°, the dashed lines indicating the expected phase peak positions.

The final Cr_2AlB_2, Cr_3AlB_4, and Cr_4AlB_6 bulk samples were irradiated with a 6.00 MeV silicon ion beam incident at 0° to the normal using the tandem accelerator at Ion Beam Lab, University of Michigan. The irradiation was performed at 150 °C and at 300 °C. The typical irradiation flux was kept at ~1.2×10^{12} ions·cm^{-2}·s^{-2}. The irradiation fluence delivered to the samples was 1.3×10^{16} ions·cm^{-2} at 150 °C (low-dose) and 2.6 $\times10^{16}$ ions·cm^{-2} at 300 °C (high dose). The background pressure during the irradiation was < 5×10^{-4} Pa. The total damage, measured in dpa, was simulated using SRIM-2013[125]. The threshold displacement energies are 25 eV, 25 eV, and 28 eV, respectively for Cr, Al, and B in all the

three ternary borides (Cr_2AlB_2, Cr_3AlB_4, and Cr_4AlB_6)[125]. The threshold displacement energies are 25 eV and 28 eV for Cr and B, respectively in the two binary borides (CrB and Cr_3B_4). For the high-dose irradiation (fluence of 2.6×10^{16} ions·cm^{-2}), the damage level obtained from the SRIM-2013 simulation was estimated to be 1.0 dpa at the surface, rising to ~15 dpa for Cr_2AlB_2, Cr_3AlB_4, and Cr_4AlB at the depth of ~2200 nm (see Fig. 5.3). The irradiation doses for CrB and Cr_3B_4 are similar to those in the Cr-Al-B MAB phases for the high-dose irradiation, and they are ~1.0 dpa at the flat region and ~20 dpa at the peak region. For the low-dose irradiation, the dose is half that of the high-dose irradiation, which is ~ 0.5 dpa at the surface for Cr_2AlB_2, Cr_3AlB_4, Cr_4AlB, CrB, and Cr_3B_4. The 0.5 dpa and 1.0 dpa are used to simplify sample naming and the actual damage is depth dependent as shown by SRIM.

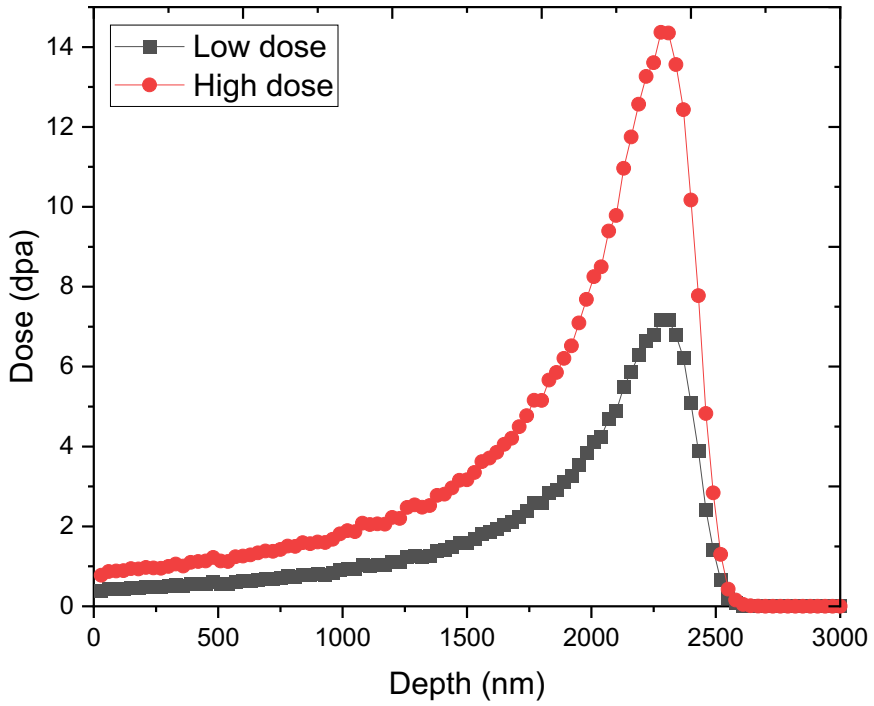

Figure 5.3 Irradiation dose in dpa versus depth profiles for Cr_2AlB_2 at a fluence of 1.3×10^{16} ions·cm^{-2}(low dose) and 2.6×10^{16} ions·cm^{-2} (high dose) under Si^{2+} irradiation.

The samples for TEM analysis were obtained using standard lift-out techniques by the FEI Helios PFIB G4 FIB/FESEM Focused Ion Beam (FIB) instrument in the Materials Science Center at the University of Wisconsin-Madison[126]. To protect the sample surface from damages during the TEM sample preparation by FIB, a 4.0 μm Pt protective layer was deposited on the surface of the samples in two steps: (i) 2 kV electron beam (low-energy) was used to deposit a 1.0 μm Pt layer to avoid damages from high-energy ions deposition and (ii) a 12 kV ion beam was used for the deposition of another 3.0 μm Pt layer[168]. The thinning process was accelerated using a high-energy ion beam (30 kV) at the beginning and a low-energy ion beam (2 kV) at the end to carefully remove the amorphous area generated during the former steps. An FEI Tecnai F30 with field emission gun (FEG) TEM and high-resolution TEM were used to analyze the damages and microstructural changes before and after the irradiation.

In Chapter 4, we discussed how the parameters for the DFT calculations of the six systems were optimized, and we reported the different types of defects with their defect formation energies. For the most stable interstitials found, the relaxed structures are shown in Fig. 4.2. In this chapter, we calculated the migration energies and the reaction energy barriers of the most stable defects and selected defects relevant for the defect recombination processes using DFT calculations and the climbing image nudged elastic band method[111]. We used the Vienna Ab-initio Simulation Package[110] with the projector augmented wave and the generalized gradient approximation by Perdew, Burke, and Ernzerhof. Following the process in Chapter 4, we have used the following supercell sizes for the defective systems: 3×3×2 and 3×3×1 for a vacancy in the binaries and the ternaries, respectively. For interstitials, we also used the same supercell sizes as in Chapter 4, determined based on the results of convergence tests. The Monkhorst-Pack *k*-point mesh sizes, plane-wave cutoff energy (400 eV), and the energy tolerance (0.5 meV/atoms) were kept the same as the previous chapter.

5.3 Results and discussion

5.3.1 Radiation performance of Cr-B binaries and Cr-Al-B ternaries

The damage introduced during the irradiation was analyzed using cross-sectional bright-field (BF) TEM and high-resolution TEM (HR TEM), and results are shown in Fig. 5.4 for the ternary Cr-Al-B MAB phases and in Fig. 5.5 for the binary Cr-B phases. In both Fig. 5.4 and Fig. 5.5, the top two rows correspond to the irradiation at the low dose at the low temperature (0.5 dpa, 150 °C), and the bottom two rows correspond to the irradiation at the high dose at the high temperature (1.0 dpa, 300 °C). As shown in Fig. 5.4, after the irradiation of 0.5 dpa at 150 °C, Cr_2AlB_2 became entirely amorphous. This is evidenced by the selected area electron diffraction (SAED) pattern, which shows diffuse rings with no indication of diffraction spots anywhere in the irradiated region, and a very small contrast in bright-field imaging, which is typical of amorphous material[141]. The HR TEM image further confirms the amorphization of Cr_2AlB_2. Cr_4AlB_6 became partially amorphous, as the SAED pattern shows both diffusion rings and some diffraction spots. The HR TEM image shows that the microstructure of Cr_4AlB_6 is highly damaged. In contrast, Cr_3AlB_4 retains a good crystalline structure, as no diffraction spots were found to be missing and the microstructure is well ordered in the HR TEM image. The results indicate that at this irradiation condition, Cr_3AlB_4 has the best radiation resistance among the three Cr-Al-B MAB phases, followed by Cr_4AlB_6, and then Cr_2AlB_2. The TEM images and corresponding SAED patterns of CrB and Cr_3B_4 at the same irradiation conditions are also shown in Fig. 5.5. Based on the results from TEM and SAED, CrB shows excellent resistance to radiation damage since the TEM image and the SAED patterns display a perfect crystal structure. There is no obvious disorder of the microstructure observed in the HR TEM image. Even in the peak damage region, there is no evidence of severe radiation damage, such as an obvious high density of black spot defects or dislocation loops. When it comes to Cr_3B_4, the damage level caused by the same irradiated fluence is higher than that in CrB, as shown in Fig. 5.5. This conclusion is made based on a much higher density of the black spot defects (based on qualitative interpretation), the distortion of diffraction spots, as well as the disorder level in the HR TEM images. The black spot defect density in the BF TEM images and the microstructure disorder level in the HR

TEM images in Cr_3B_4 are slightly higher than in Cr_3AlB_4 for the same irradiation condition. Therefore, it can be concluded that, at 150 °C and 0.5 dpa, the order of the radiation damage resistance of these materials is, from high to low: CrB, Cr_3AlB_4, Cr_3B_4, Cr_4AlB_6, and Cr_2AlB_2.

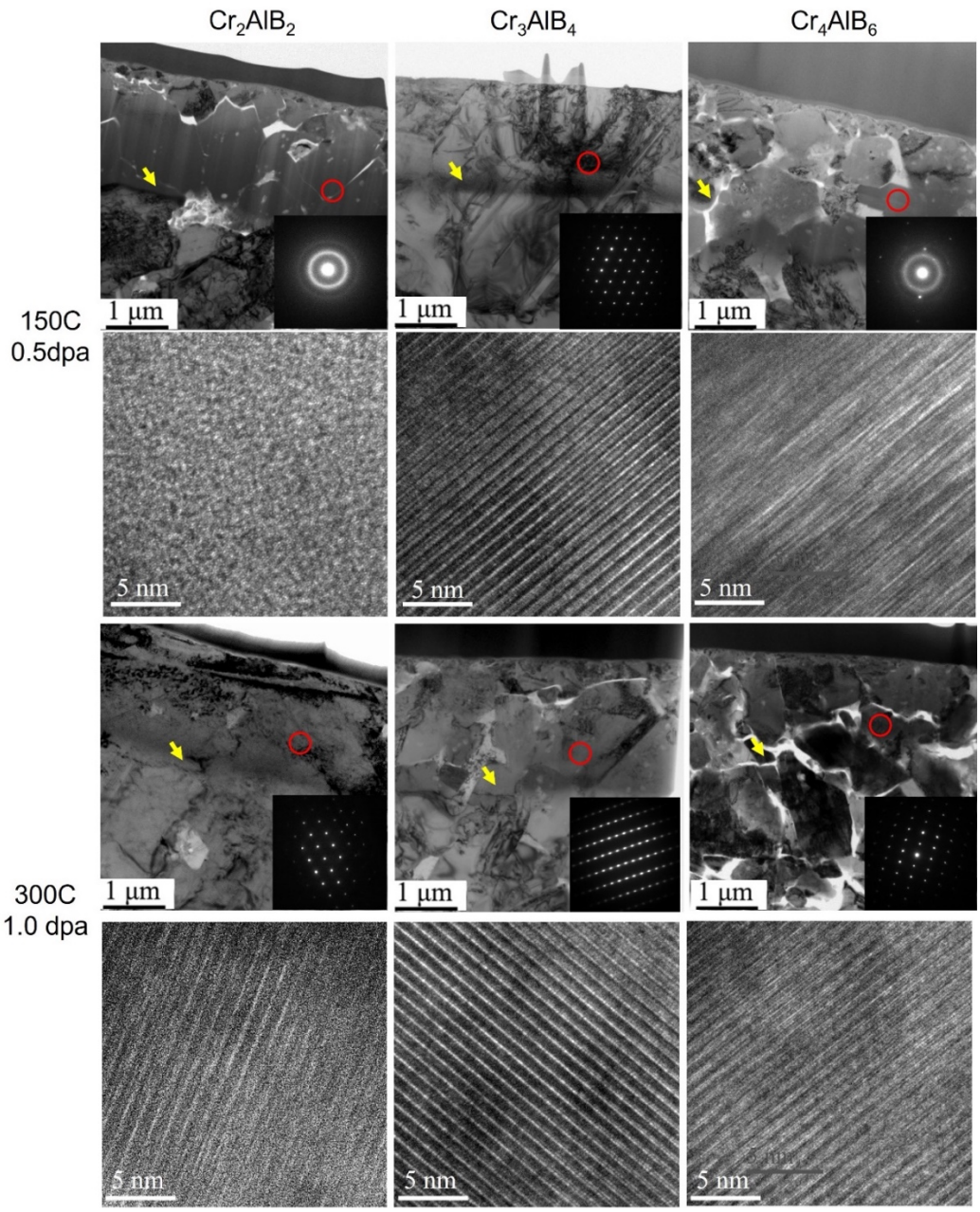

Figure 5.4 BF TEM and corresponding HR TEM images (viewed from (110)) of Cr_2AlB_2, Cr_3AlB_4, and Cr_4AlB_6, irradiated at 1.3 $\times 10^{16}$ ions·cm^{-2} at 150 °C (top row), at 2.6 $\times 10^{16}$ ions·cm^{-2} at 300 °C (bottom row). The red circle in each image indicates the region that was analyzed by SAED. The yellow arrow in each image indicates the damage peak.

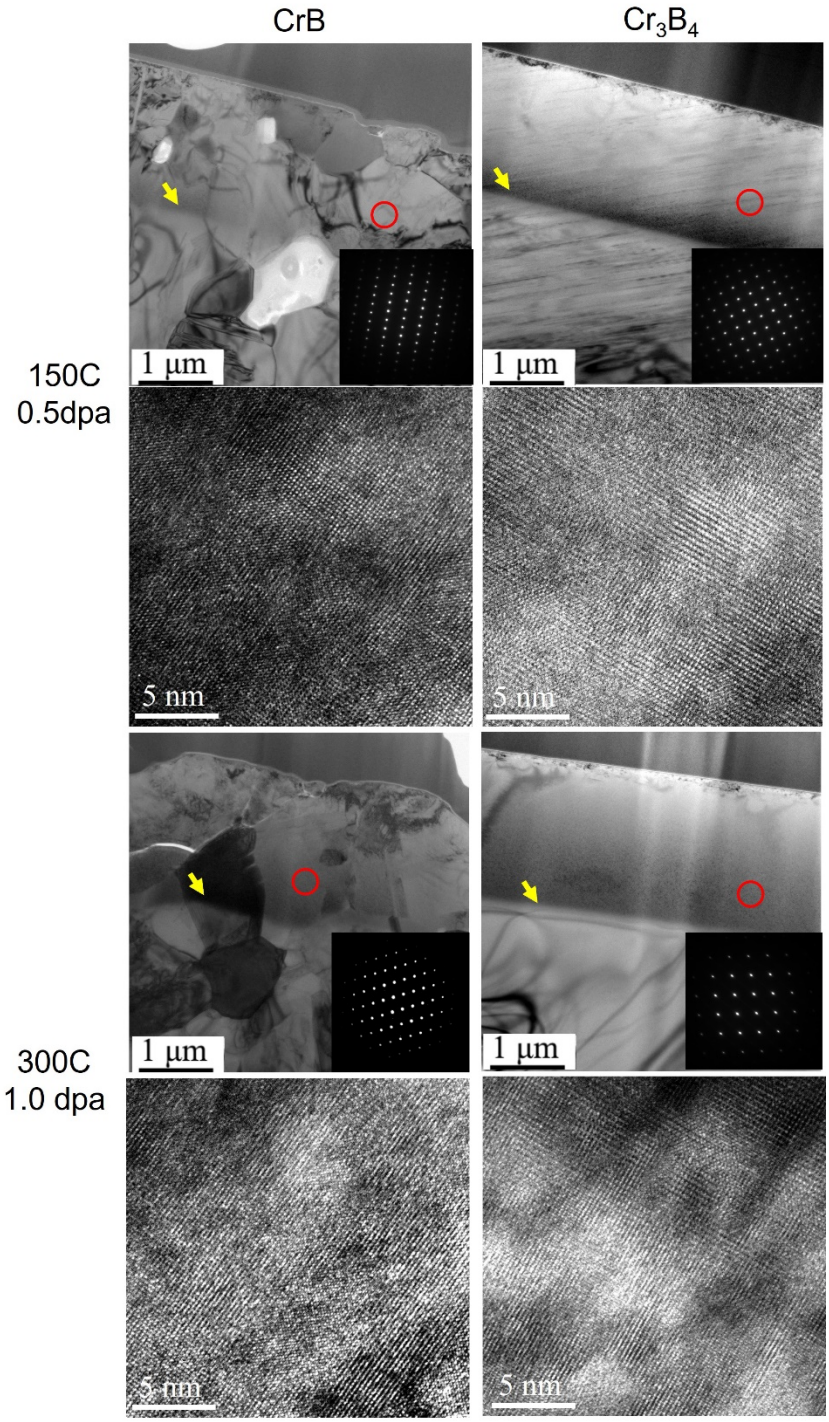

Figure 5.5 BF TEM and corresponding HR TEM images (viewed from (110)) of CrB and Cr_3B_4, irradiated at 1.3 $\times 10^{16}$ ions·cm^{-2} at 150 °C (top row) and at 2.6 $\times 10^{16}$ ions·cm^{-2} at 300 °C (bottom row). The red circle in each image indicates the region that was analyzed by SAED. The yellow arrow in each image indicates the damage peak.

When the irradiation temperature increased to 300 °C and the irradiation dose increased to 1.0 dpa, all the three Cr-Al-B MAB phases remained crystalline after the irradiation even at the peak region, indicating a much better radiation resistance at the high temperature. CrB and Cr_3B_4 also exhibited good crystallinity in the flat damage region, but there is an amorphous band with the width of about 0.15 μm in the peak damage region of Cr_3B_4, corresponding to the damage dose of ~12 dpa. It should be also noted that Si implantation is greatest here and may contribute to the observed feature. Therefore, it is clear that at 300 °C, Cr_3AlB_4 is more resistant to radiation-induced amorphization than Cr_3B_4. However, based on the results from the TEM images (see the bottom rows of Fig. 5.4 and Fig. 5.5), it is difficult to tell which Cr-Al-B MAB phase is most resistant to radiation-induced damage at 300 °C, and it is also difficult to tell if CrB is better than the Cr-Al-B ternary MAB phases at this temperature. Therefore, the distortion of the SAED patterns was analyzed along with the GI XRD patterns, and the corresponding full-pattern Rietveld refinements were used to distinguish the level of the radiation-induced damage. Fig. 5.6 shows the GI XRD patterns for CrB, Cr_3B_4, Cr_2AlB_2, Cr_3AlB_4, and Cr_4AlB_6 irradiated at 300 °C and 1.0 dpa, at the incident angle of 1.0°. Unlike the GI XRD results of the irradiated MAX phases, where a significant shift of peaks has been reported[141,169], no obvious shift of the peak positions was found in the patterns of the irradiated CrB and Cr_3B_4 phases, indicating that the change in the lattice parameter (LP) was very small. However, peak shifts were found in the spectra of the irradiated ternaries, Cr_2AlB_2, Cr_3AlB_4, and Cr_4AlB_6. The GI XRD data and the refinement results show that the radiation-induced LP change in Cr_3AlB_4 is the smallest of the three Cr-Al-B MAB phases at the irradiation condition of 300 °C and 1.0 dpa. Specifically, the *a*-LP increased by 0.8% in Cr_3AlB_4, by 1.3% in Cr_4AlB_6, and by 1.9% in Cr_2AlB_2. The *b*-LP decreased by 0.5 % in Cr_3AlB_4, by 1.0 % in Cr_4AlB_6, and by 1.0% in Cr_2AlB_2. The *c*-LP decreased by 0.8% in Cr_3AlB_4, by 1.1 % in Cr_4AlB_6, and by 1.3% in Cr_2AlB_2. Note that the LP change in MAX phase Ti_3SiC_2[131] is: *a*-LP decreased by ~1.0% and *c*-LP increased by ~4%. The radiation-induced LP change in CrB is a little larger (increase by 1.1% in *a*, *b* and *c*-LPs) than that in Cr_3AlB_4, but the swelling is uniform in all the three directions. The decrease in the peak intensity is quite obvious for Cr_3B_4 but not obvious for CrB and all the three MAB phases. Moreover, the GI XRD patterns of Cr_3B_4 after the

irradiation show disappearance of several peaks of Cr_3B_4 but include strong peaks of CrB, located at about 32°, 38°, and 45°, and another small peak of CrB_2 located at ~43°, which indicates phase decomposition of Cr_3B_4 after the irradiation. In general, by combining the GI XRD results with the TEM and SAED analysis, it can be concluded that, at 300 °C, Cr_3AlB_4 is the most radiation-resistant, followed by CrB, Cr_3B_4, Cr_4AlB_6, and Cr_2AlB_2.

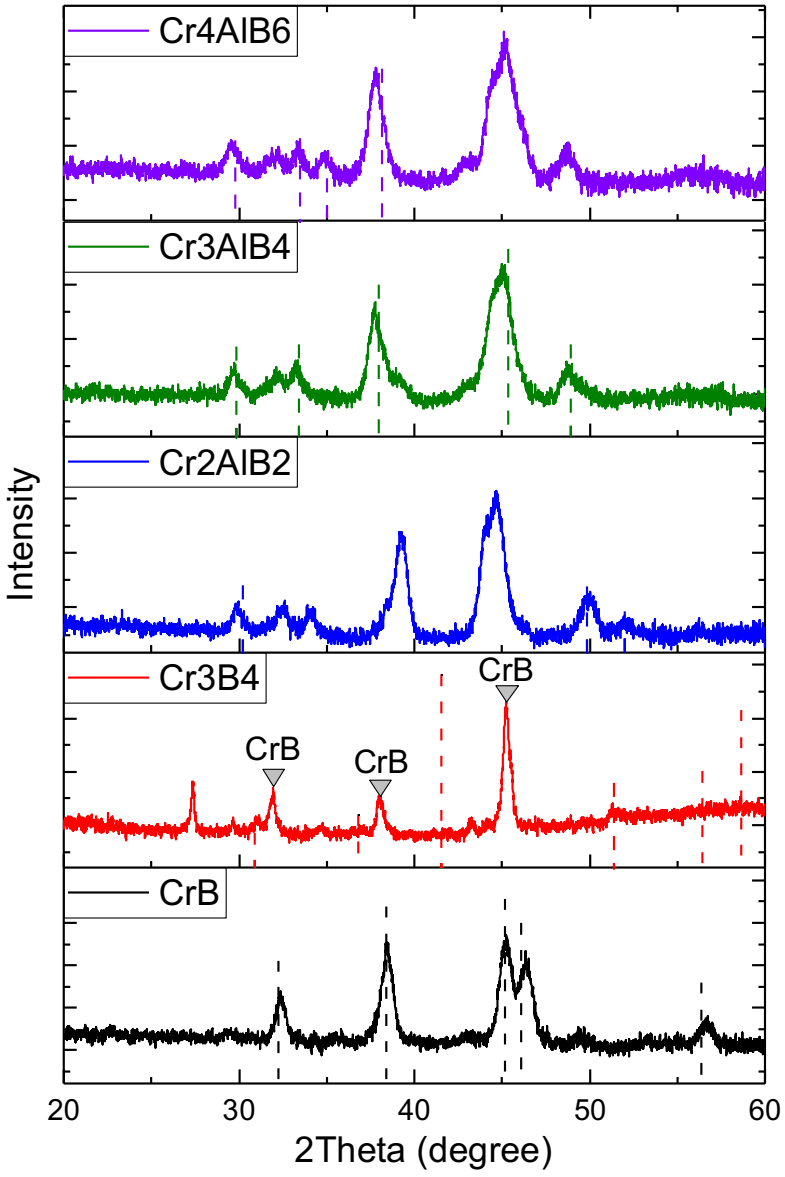

Figure 5.6 GI XRD patterns at the incident angle of 1.0° for Cr_2AlB_2, Cr_3AlB_4, Cr_4AlB_6, CrB and Cr_3B_4 at 2.6 $\times 10^{16}$ ions·cm^{-2} (1.0 dpa) and 300 °C. The dashed lines show the peak positions of the unirradiated phases.

To summarize, our experiments showed the resistance to radiation-induced amorphization of Cr-B and Cr-Al-B systems, as follows. For the effect of B networks, in the ternaries, Cr_3AlB_4 (one-B-ring) is the best, followed by Cr_4AlB_6 (two-B-ring), and then Cr_2AlB_2 (one-B-chain), whereas in the binaries, CrB (one-B-chain) performs better than Cr_3B_4 (two-B-ring). As for the effect of Al layers in the one-B-chain structures, CrB performs better than Cr_2AlB_2, whereas in the one-B-ring structures, Cr_3AlB_4 is better than Cr_3B_4.

5.3.2 Migration energies and reaction energy barriers

The structure-dependent radiation tolerance of the Cr-B binaries and Cr-Al-B MAB phases can be explained based on the results of my first-principles calculations. For a material to be tolerant to radiation-induced amorphization, it needs to efficiently remove the radiation-induced defects, predominantly Frenkel pairs (FPs). FPs can be recovered through a vacancy-interstitial recombination process, for which either the vacancy migration energy or the interstitial migration energy must be low relative to the thermal energy. In addition, the recombination energy barrier, which can exist in covalently bonded materials[144,170], also must be low compared with the thermal energy. Here, we compare the migration energies, the recombination barriers, and the recombination process of FPs between the six systems to rationalize our experimental results.

The most stable defects and other selected defects relevant for defect recombination processes were depicted in Fig. 4.2, and we report the lowest migration energies of the defects in Table 5.1. The migration energy for Cr_I in CrB (0.06 eV) is significantly lower than in Cr_3B_4 and Cr_2B_3 (~1.6 eV). This is because the most stable Cr_I in CrB is located in the Cr layers (Type 1 in Fig. 4.2), whereas the most stable Cr_I in the other two systems (Cr_3B_4 and Cr_2B_3) are found inside the B networks (Type 7 and 8 in Fig. 4.2). In the ternaries, Cr_I are all found in the Al layers (Type 6 in Fig. 4.2), and their migration energies are comparable among the different systems (~1.3 eV). As for B_I in all the binaries, these defects form a B bridge (Type 2 in Fig. 4.2), and the migration energies are ~1.8 eV. In contrast, in the ternaries, B_I is found in the Al layers (Type 3-5 in Fig. 4.2), and the migration energies are in the range of

0.73-0.82 eV. Al_I, which exist in the ternaries only, are found in the Al layers, and the migration energies of Al_I for all the ternaries are ~0.2 eV. For vacancies in the binaries and ternaries, the migration energies of V_{Cr} and V_{Al} are significantly higher than the corresponding interstitial migration energies (see Table 5.1). In CrB and Cr_2AlB_2, there is only one type of V_B, and it migrates into an equivalent site with the energy of 0.93 eV and 0.76 eV, respectively, in the two systems. In Cr_3B_4 and Cr_3AlB_4, the most stable V_B (V_{B2} on a B2 site in Figs. 5.1(b) and (e)) migrates into an equivalent site with the energy of ~1.1 eV. The second most stable vacancy, V_{B1} (on a B1 site in Figs. 5.1(b) and (e)) can migrate into a B2 site with the energy of 0.68 eV and 0.58 eV, respectively, in Cr_3B_4 and Cr_3AlB_4. V_B is then stabilized on the B2 site, since the opposite reaction (V_{B2} migrates from B2 to B1 site) has the migration energy of 1.11 eV and 0.93 eV, respectively in Cr_3B_4 and Cr_3AlB_4. In Cr_2B_3 and Cr_4AlB_6, the most stable V_B (V_{B3} on a B3 site in Figs. 5.1(c) and (f)) migrates into an equivalent site with the energy of 0.71 eV. The other V_B (V_{B1} and V_{B2}) can also migrate into the more stable vacancy site with the following paths: V_{B1} migrates into a B2 site (~0.7 eV both in Cr_2B_3 and Cr_4AlB_6) and V_{B2} migrates into a B3 site (~0.8 eV both in Cr_2B_3 and Cr_4AlB_6). As for the opposite direction, V_{B3} migrates into a B2 site with the energy of ~1.2 eV both in Cr_2B_3 and Cr_4AlB_6, and V_{B2} migrates into a B1 site with the energy of 1.24 eV and 0.97 eV, respectively in Cr_2B_3 and Cr_4AlB_6.

We also calculated the energy barriers that each FP must overcome to recombine, and we tabulated the results in Table 5.2. "Diff" denotes a diffusion-limited step, namely a barrierless reaction. The number in parentheses represents the lower migration energies of the vacancy or interstitial, which means that it governs the recombination process. The recombination reactions of Cr FPs in all the borides considered here are barrierless and are controlled by the migration of Cr_I. In the binaries, B FPs recombine without a barrier, and the reactions are governed by the migration of V_B. On the other hand, in the ternaries, B FP recombination barriers are 1.30 eV for Cr_2AlB_2 and ~0.9 eV for Cr_3AlB_4 and Cr_4AlB_6. Lastly, Al FPs in the ternaries recombine without a barrier, and the reactions are controlled by the diffusion of Al_I.

Table 5.1 The lowest migration energies of the most stable defects and other selected defects relevant for defect recombination processes.

eV	CrB	Cr_3B_4	Cr_2B_3	Cr_2AlB_2	Cr_3AlB_4	Cr_4AlB_6
Cr_I	0.06	1.57	1.61	1.28	1.26	1.26
B_I	1.78	1.79	1.80	0.82	0.74	0.73
Al_I	N/A	N/A	N/A	0.24	0.20	0.18
V_{Cr}	3.28	5.80	4.56	4.74	6.02	5.01
$V_{B1} \rightarrow V_{B2}^{\dagger}$	0.93	0.68	0.71	0.76	0.58	0.65
$V_{B2}^{\dagger} \rightarrow V_{B1}$	0.93	1.11	1.24	0.76	0.93	0.97
$V_{B2} \rightarrow V_{B3}^{\ddagger}$	N/A	1.10	0.78	N/A	1.09	0.75
$V_{B3}^{\ddagger} \rightarrow V_{B2}$	N/A	1.10	1.17	N/A	1.09	1.25
$V_{B3} \rightarrow V_{B3}$	N/A	N/A	0.71	N/A	N/A	0.71
V_{Al}	N/A	N/A	N/A	2.24	1.91	1.83

$^{\dagger}V_{B2}$ for CrB and Cr_2AlB_2 indicates V_{B1}.
$^{\ddagger}V_{B3}$ for Cr_3B_4 and Cr_3AlB_4 indicates V_{B2}.

Table 5.2 FP recombination energy barriers. "Diff" denotes a diffusion-limited step, and the number in parentheses is the lower of the migration energies of the FP defect.

eV	CrB	Cr_3B_4	Cr_2B_3	Cr_2AlB_2	Cr_3AlB_4	Cr_4AlB_6
Cr	Diff (0.06)	Diff (1.57)	Diff (1.61)	Diff (1.28)	Diff (1.26)	Diff (1.26)
B	Diff (0.93)	Diff (0.68)	Diff (0.71)	1.30	0.89	0.88
Al	N/A	N/A	N/A	Diff (0.24)	Diff (0.20)	Diff (0.18)

5.3.3 Effects of Al layers and B networks on defect recovery processes

Using the migration energies and the recombination energy barriers in Table 5.1 and Table 5.2, we explain our experimental results in terms of the structural differences and their impact on defect recovery processes. First, we discuss the effects of B networks by comparing CrB (one-B-chain) vs. Cr_3B_4 (one-B-ring) and Cr_2AlB_2 (one-B-chain) vs. Cr_3AlB_4 (one-B-ring) vs. Cr_4AlB_6 (two-B-ring). Subsequently, we discuss the effects of Al layers by comparing the binaries and the ternaries (i.e., CrB vs. Cr_2AlB_2 and Cr_3B_4 vs. Cr_3AlB_4).

In our experiments on the binaries, we observed that CrB showed the better performance under the irradiation than Cr_3B_4. The different performances can be explained by the difference in the location of Cr_I and their migration energies. In CrB, Cr_I is located in the Cr layers and it migrates with the migration energy of 0.06 eV, so the recombination of Cr FPs is expected to be very efficient. On the other hand, in Cr_3B_4, the most stable Cr_I is found in the B network layer and it migrates with the migration energy of 1.57 eV, which is significantly higher than that of Cr_I in CrB (0.06 eV). Therefore, compared with CrB, the rate of Cr FP recombination in Cr_3B_4 is low, which is consistent with the relatively poor radiation performance of Cr_3B_4 compared with CrB, as observed in the experiments. In the two systems (CrB and Cr_3B_4), the recombination process of B FPs shows no significant difference (see Table 5.2).

In the ternaries, we observed experimentally that Cr_3AlB_4 performs best under the irradiation, followed by Cr_4AlB_6 and then Cr_2AlB_2. First of all, the relatively poor radiation tolerance of Cr_2AlB_2 (one-B chains), compared with Cr_3AlB_4 and Cr_4AlB_6 (which have one-B or two-B rings, respectively), can be attributed to the B FP recombination process. In each of the ternary systems, Al FPs are expected to be easily annealed because the recombination is barrierless and is governed by fast Al_I (migration energy of ~0.2 eV). Also, Cr FPs are expected to behave similarly in all the three ternaries: the recombination is barrierless and is controlled by Cr_I (migration energy of ~1.3 eV). For the B FP recombination, the migration energies of both B_I and V_B in all the three ternaries are low enough to be mobile (0.73-0.82 eV for B_I, 0.58-0.97 eV for V_{B1}). The recombination paths are also identical in all the three ternaries: B_I located within the Al layers moves into a B1 site to recombine with V_B. However, the barrier of this recombination process is 1.30 eV in Cr_2AlB_2 (which has one-B chains), and it is ~0.9 eV in Cr_3AlB_4 and Cr_4AlB_6 (which have B rings) (see Table 5.2). Since a lower recombination barrier means that the defects can be recombined faster, this difference in the recombination barrier is consistent with the better performance of Cr_3AlB_4 and Cr_4AlB_6 than that of Cr_2AlB_2. The difference in the recombination barriers can be explained by the difference in the bond strengths. Specifically, the B FP recombination barrier in Cr-Al-B MAB phases likely depends on the strengths of the nearby Cr-B bonds. When a B_I

atom moves into a V_B site to recombine, nearby atoms need to shift to make way for the interstitial. The stronger the bond, the higher the energy cost required to move the neighboring atoms, which makes the recombination barrier higher. In Chapter 4, we estimated the strengths of the different bonds in Cr-Al-B systems and found that the Cr-B bonds in Cr_3AlB_4 and Cr_4AlB_6 are comparable to each other and are significantly weaker than those in Cr_2AlB_2. In summary, the better performance of Cr_3AlB_4 and Cr_4AlB_6, compared with Cr_2AlB_2, can be explained by the structural differences. The systems with B rings (Cr_3AlB_4 and Cr_4AlB_6) have weaker Cr-B bonds than those with B chains (Cr_2AlB_2), which leads to the lower barriers of B FP recombination in the systems with B rings.

Next, Cr_3AlB_4 was found experimentally to have a better radiation resistance than Cr_4AlB_6, which can be rationalized in terms of B FP recombination. Although the migration energies and the reaction energy barriers are all comparable in the two systems (see Table 5.2) and the B FP recombination paths are identical, the structural difference (one-B-ring vs. two-B-ring) affects the probability for B FPs to recombine. As mentioned earlier, the recombination process of B FPs in ternary MAB phases occurs by B_I moving from the Al layers to a V_B site nearby. Thus, in Cr_3AlB_4 and Cr_4AlB_6, for a B_I to recombine with a V_B, the V_B needs to be on the sites nearest to the Al layer (i.e., B1 position in Figs. 5.1(e) and (f)). Cr_3AlB_4 (one-B-ring) allows V_B to occupy B1 sites and recombine with B_I, whereas in Cr_4AlB_6 (two-B-ring) V_B has a low probability of occupying B1 sites, based on a high probability of V_B moving from V_{B1} to V_{B2} and then V_{B3}, and the high formation energies of V_B. Specifically, in Cr_3AlB_4, as shown in Table 5.1, V_{B1} migrates into V_{B2} with the migration energy of 0.58 eV, whereas V_{B2} can migrate to V_{B1} with the migration energy of 0.93 eV or it can migrate to an equivalent V_{B2} with the migration energy of 1.09 eV. In Cr_4AlB_6, V_{B1} migrates to V_{B2} with the migration energy of 0.65 eV. V_{B2} migrates to V_{B1} with the migration energy of 0.97 eV, or it migrates to V_{B3} with the migration energy of 0.74 eV, which means that the latter migration would be preferable. V_{B3} migrates into V_{B2} with the migration energy of 1.25 eV or migrates into an equivalent V_{B3} with the migration energy of 0.71 eV. In summary, V_B in Cr_3AlB_4 can be found on B1 and B2 sites, allowing B_I to easily recombine with V_B. In Cr_4AlB_6, V_B migrates preferentially into B2 and then B3 sites rather than the other way, which means that V_B is likely trapped

in V_{B3}, making it difficult to recombine with B_I. In addition, my defect chemistry study (Chapter 4) supports the different behavior of V_B. We reported the formation energies referenced to the vacuum level of V_B in Cr_3AlB_4 and Cr_4AlB_6 as follows: V_{B1} (8.37 eV), V_{B2} (8.12 eV) in Cr_3AlB_4 and V_{B1} (8.12 eV), V_{B2} (7.80 eV), V_{B3} (7.29 eV) in Cr_4AlB_6. This data shows that the difference in the formation energies between V_{B1} and V_{B3} makes V_B easier to form on B3 sites rather than B1 and supports the conclusion that B FPs are more difficult to recombine in Cr_4AlB_6 than Cr_3AlB_4.

Lastly, we discuss the effect of the Al layers on the radiation resistance. First, our experiments showed that in the case of one-B-chain structures (CrB and Cr_2AlB_2), CrB performed better under the irradiation than Cr_2AlB_2. We can attribute the inferior performance of Cr_2AlB_2 to the effects of Cr FP recombination. In CrB, Cr FPs are expected to be easily removed because the recombination process is diffusion-limited and controlled by the fast Cr_I with the migration energy of 0.06 eV, as shown in Table 5.2. On the other hand, in Cr_2AlB_2, Cr_I migrates with the migration energy of 1.28 eV, which is significantly higher than that of CrB (0.06 eV), leading to slower recombination of Cr FPs in Cr_2AlB_2 and ultimately the better performance of CrB. Note that the recombination process of B FPs in CrB is also faster than that of Cr_2AlB_2 (see Table 5.2). Next, in our experiments for the one-B-ring structures (Cr_3B_4 and Cr_3AlB_4), Cr_3AlB_4 is better than Cr_3B_4 at 300 °C (slightly better at 150 °C). Our calculations showed that the migration energy of Cr_I in Cr_3AlB_4 (1.26 eV) is lower than that in Cr_3B_4 (1.57 eV), which can explain our experiments. In comparison to Cr_3AlB_4, Cr FPs are less likely to recombine in Cr_3B_4 because of the migration energy of Cr_I being too high (1.57 eV). In both systems, B FPs (and Al FPs for Cr_3AlB_4) are expected to recombine based on the energies reported in Table 5.1 and Table 5.2.

5.4 Conclusions

In summary, in terms of radiation-induced amorphization, our TEM analysis and DFT studies concluded: for the effects of the B networks, (1) CrB (one-B-chain) is better than Cr_3B_4 (one-B-ring) and (2) Cr_3AlB_4 (one-B-ring) performs the best among the ternaries, followed by Cr_4AlB_6 (two-B-ring) and Cr_2AlB_2 (one-B-chain). When it comes to the effects of the Al layers, we found that (3) CrB is better than

Cr_2AlB_2, (4) Cr_3AlB_4 is better than Cr_3B_4. The different performances were explained by the structure-dependent defect recovery processes: the Al layers tend to prevent B FPs from recombining, and the B FP recombination is largely controlled by the number of B rings.

Our joint experimental and computational study provides a new understanding of how structural differences in layered borides affect the defect recovery processes and the tolerance to radiation-induced amorphization.

CHAPTER 6

DESIGN RULES FOR DEFECT RECOVERY PROCESS

6.1 Introduction

Binary transition metal borides (TMBs), classified as ultra-high temperature ceramic[142,171], have long been studied for many applications, including wear resistant coating[171], aerospace thermal protection[172], and high temperature diffusion barrier[146], owing to their high hardness, high melting temperature[142], good thermal and electrical conductivities[173], and high-temperature strength[174]. More recently, ternary TMBs, called MAB (M = transition metal; A = Al; B = B) phases[27] have also been studied and shown to have outstanding properties, such as good oxidation resistance[39,143], magnetocaloric effect[43], and radiation tolerance[144], while maintaining such benefits of binary TMBs as hardness[27,48] as well as thermal and electrical conductivities[53,54]. In addition, MBene, a new class of two-dimensional systems exfoliated from MAB phases, has been considered for promising materials in spintronics applications[74] and safe biological applications[75,163]. Many MAB phases have been theoretically predicted so far, while only a few of them have been synthesized[62,162].

Many of the aforementioned properties of TMBs depend on the presence of defects and on their thermokinetic behavior. In the studies on the binary and ternary TMBs in Chapter 3-5, we reported the defect recovery processes in MoAlB and Fe_2AlB_2[144] as well as in a series of Cr-B and Cr-Al-B systems. These specific materials have been shown to be promising for applications that involve radiation and chemically aggressive environments, due to their efficient defect recovery processes. Based on our findings in these specific systems, we have formulated hypotheses for how the Al layers and the type of transition metal elements affect the defect stability and kinetics. These hypotheses are investigated in this chapter by considering a series of different transition metal elements, and we generalize our findings from

the specific systems (Mo-, Fe-, and Cr-based TMBs) to TMBs with different transition metal elements in order to provide guidance for the design of TMBs.

Firstly, in Chapter 3, we found that the defect recovery processes in Fe_2AlB_2 (which has one-Al-atomic layers) are more efficient than in MoAlB (which has two-Al-atomic layers), because of the presence of unstable Mo_I in MoAlB. In Fe_2AlB_2, Fe_I is stable in Al layers (one-atomic) and easily migrates and recombines with V_{Fe}. In contrast, in MoAlB, when a Mo atom is introduced as an interstitial within the Al layers, the Mo atom is relaxed into a nearby Al lattice site (i.e., becomes an antisite, Mo_{Al}), by kicking out the Al atom and making it an interstitial, Al_I. This behavior of unstable Mo_I and Mo_{Al} is considered detrimental for the defect recovery processes in MoAlB because Mo_{Al} is immobile and does not easily react with the other defects, preventing Al_I from finding and recombining with V_{Al} in MoAlB. Based on this study, we hypothesize that $M_1A_1B_1$ (MAB phases which have two-Al-atomic layers) cannot accommodate M_I in the Al layers. This is in contrast to $M_2A_1B_2$ (MAB phases which have one-Al-atomic layer), where M_I is stable in the Al layers. This hypothesis is tested in this chapter by investigating the stability of M_I in $M_1A_1B_1$ and $M_2A_1B_2$ with different transition metal elements. In this chapter, I use the notation $M_1A_1B_1$ for the particular systems to avoid confusion with MAB phases for ternary TMBs.

In Chapter 4 and Chapter 5, the studies on CrB, Cr_3B_4, Cr_2B_3, Cr_2AlB_2, Cr_3AlB_4, and Cr_4AlB_6, we found that the presence of Al layers in the structure plays a crucial role in the migration and recombination processes of defects. For CrB and Cr_2AlB_2, where B networks form as B chain, the presence of Al layers in Cr_2AlB_2 significantly hinders the recombination and migration processes of Cr and B Frenkel Pairs (FPs). In CrB, the most stable Cr_I, found in Cr layers, migrates faster than the most stable Cr_I in the ternary counterpart (Cr_2AlB_2), which is found in Al layers. In addition, the presence of Al layers increases the recombination barriers of B FPs in Cr_2AlB_2, while the recombination of B FPs in CrB is barrierless. Based on this observation, we formulate hypotheses that M_I migrates faster in M_1B_1 compared with the corresponding MAB ternaries ($M_2A_1B_2$) and that the recombination barriers of B FPs in M_1B_1 are lower than that in $M_2A_1B_2$. To test the hypotheses, we study the migration energies of M_I and the recombination barriers of B FPs in M_1B_1 and $M_2A_1B_2$ with different transition metal elements. As for

Cr_3B_4 and Cr_3AlB_4, where the B networks form as B rings, the Al layers help lower the migration energy of Cr_I, but hinder the recombination process of B FPs. To find a general trend of the role of the Al layers, I study the migration energies of M_I and the recombination barriers of B FPs in M_3B_4 and $M_3A_1B_4$ with different transition metal elements.

By comparing the defect recovery processes of Cr_2AlB_2 and Cr_3AlB_4, we found that the B FP recombination barriers in Cr-Al-B ternaries largely depend on the strengths of the nearby Cr-B bonds. Although Cr_2AlB_2 (B chains) and Cr_3AlB_4 (B rings) have the different types of B networks, they share the same local environment where B FPs recombine, and the recombination processes in the two systems are identical. However, the Cr-B bonds in Cr_2AlB_2 are stronger than those in Cr_3AlB_4, resulting in the recombination barrier of B FP in Cr_2AlB_2 higher than that in Cr_3AlB_4. This is because, during the B FP recombination, in which the nearby atoms need to shift to make room for the interstitial, the stronger nearby bonds require a higher energy cost to move the neighboring atoms, leading to a higher recombination barrier. In addition, my comparative analysis on Fe_2AlB_2 (Chapter 3) and Cr_2AlB (Chapter 4), which share the exact same structure, revealed the same trend: the Cr-B bonds in Cr_2AlB_2 are stronger than the Fe-B bonds in Fe_2AlB_2, and the B FP recombination barrier in Fe_2AlB_2 is lower than that in Cr_2AlB_2. Based on the findings, I hypothesize that transition metal elements with weaker M-B bonds in MAB phases lead to a lower B FP recombination barrier. I test the hypothesis and generalize the aforementioned trend with the two types of MAB phases that share the same local environment ($M_2A_1B_2$ and $M_3A_1B_4$) over different transition metal elements.

The structures of TMBs studied in this chapter are M_1B_1, M_3B_4, $M_2A_1B_2$, $M_3A_1B_4$, and $M_1A_1B_1$, as shown in Fig. 6.1. I selected these systems because many of these systems have been theoretically predicted and our earlier studies are based on these compositions. First, the binaries consist of transition metals bonded to B networks, wherein the B networks may be B chains (M_1B_1 in Fig. 5.1(a)) or B rings (M_3B_4 in Fig. 5.1(b)). Figure 5.1(c) shows $M_2A_1B_2$, where the transition metals bonded to B chains are interleaved by the one-Al-atomic layers. In Fig. 5.1(d), $M_3A_1B_4$ consists of transition metals bonded to B the rings, interleaved by the one-Al-atomic layers. In $M_1A_1B_1$ shown in Fig. 5.1(e), the two-Al-atomic

layers interleave the transition metals bonded to the B chains. To investigate the defect properties in these five structures and to test the aforementioned hypotheses, I performed density functional theory (DFT) calculations focusing on four topics: (i) the effects of the number of Al layers (one-Al-atomic layers vs. two-Al-atomic layers) on the stability of M_I in $M_2A_1B_2$ and $M_1A_1B_1$, (ii) the effects of Al layers (the presence of Al layers vs. the absence of Al layers) on the migration of M_I and the recombination of B FPs in M_1B_1 and $M_2A_1B_2$, (iii) the effects of Al layers (the presence of Al layers vs. the absence of Al layers) on the migration of M_I and the recombination of B FPs in M_3B_4 and $M_3A_1B_4$, and (iv) the effects of the type of transition metal elements in $M_2A_1B_2$ and $M_3A_1B_4$ on the B FP recombination barriers. Lastly, based on the calculated kinetic properties of defects (i.e., migration and recombination), I discuss the defect recovery processes in light of nuclear reactor applications.

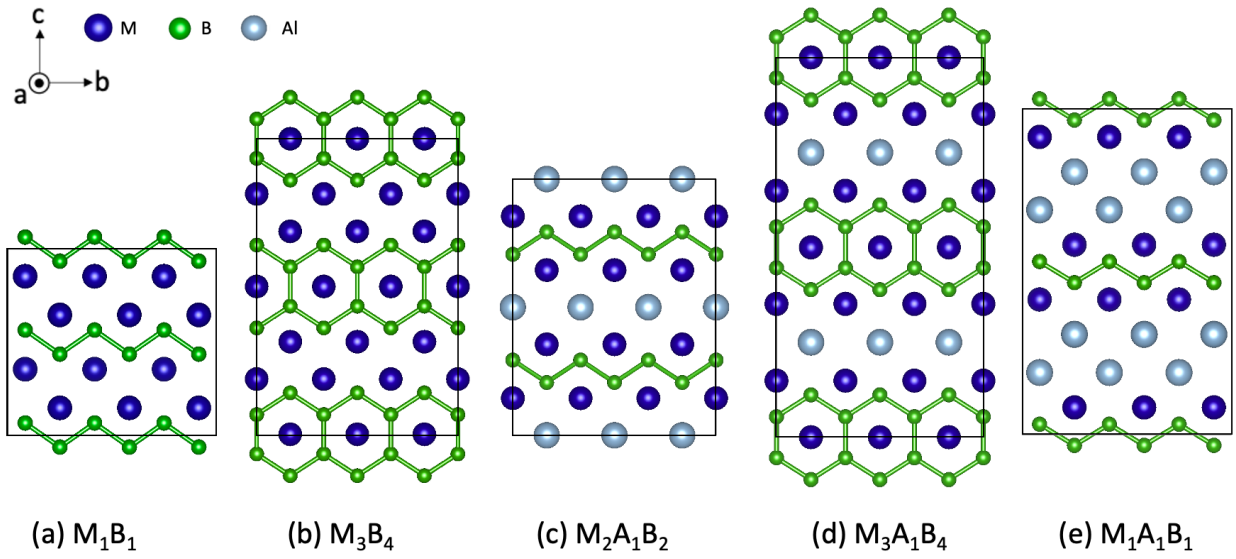

Figure 6.1 Atomic structures of (a) M_1B_1, (b) M_3B_4, (c) $M_2A_1B_2$, (d) $M_3A_1B_4$, and (e) $M_1A_1B_1$.

6.2 Methods

The defect properties were determined based on DFT calculations using the Vienna Ab-initio Simulation Package[110] with the projector augmented wave[127] and the generalized gradient approximation

by Perdew, Burke, and Ernzerhof[99]. We optimized the unit cells of the TMBs with the plane-wave cutoff energy of 450 eV and the energy tolerance of 0.1 meV/atoms. Monkhorst-Pack *k*-point mesh[128] of 10×10×4 (M_1B_1), 11×11×5 (M_3B_4), 11×11×3 ($M_2A_1B_2$), 11×11×4 ($M_3A_1B_4$), and 10×10×2 ($M_1A_1B_1$) were set. The calculated lattice constants agree well with previously reported works[62,175,176]. The total energies of the perfect structures and those containing defects were calculated in 4×4×2 supercells for all the systems, and the size of the supercells was determined based on the interstitial convergence tests for M = Cr. For the supercell calculations, Monkhorst-Pack *k*-point mesh of 3×3×2 (M_1B_1, M_3B_4), 2×2×2 ($M_2A_1B_2$, $M_2A_1B_2$), and 3×3×1 ($M_1A_1B_1$) were set. To calculate the migration energies and the reaction energy barriers of defects, I used the climbing image nudged elastic band method[111]. In addition, in order to find a correlation between the defect kinetics properties and the strength of chemical bonds, I calculated the bond separation energies by subtracting the energy of a perfect unit cell from the energy of a unit cell where a vacuum region of 2 nm thickness is inserted between the layers and finally by dividing the energy difference by the number of surface atoms.

6.3 Results and discussion

6.3.1 Effects of the number of Al layers: $M_1A_1B_1$ vs. $M_2A_1B_2$

I first test the hypothesis that $M_1A_1B_1$ (which has two-Al-atoimc layers) cannot accommodate M_I in their Al layers, whereas M_I can be accommodated in the Al layers of $M_2A_1B_2$ (which has one-Al-atomic layers). This hypothesis is tested by considering a number of different $M_1A_1B_1$ and $M_2A_1B_2$ systems with different transition metal elements. We tested eight different systems (M = Cr, Ti, V, Nb, Mo, Hf, Ta, W) for $M_1A_1B_1$ and ten different systems (M = Cr, Fe, Mn, Ni, Rh, Ru, Sc, Ti, V, W) for $M_2A_1B_2$. The elements were chosen because they have been predicted theoretically to be stable either in the $M_1A_1B_1$ or in the $M_2A_1B_2$ composition or in both[62]. In each of the MAB phases, an M atom was introduced as an interstitial within an Al layer, and the system was relaxed. As an example of interstitial configuration for $M_1A_1B_1$ (which has two Al layers), in Fig. 6.2(a) I show the atomic structure of CrAlB

with a Cr_I (①) before the relaxation. The Cr atom was introduced at the center of four Al atoms that form a tetrahedron. During the relaxation, the Cr_I kicks out a nearby Al atom (②) and takes the Al site, as indicated by the red arrows in Fig. 6.2(a). After the relaxation, as shown in Fig. 6.2(b), the Cr atom forms an antisite (Cr_{Al}) on the Al site (①), and the kicked-out Al atom forms Al_I (②). The same mechanism was found in all the eight $M_1A_1B_1$ (which have two Al layers). In other words, in the $M_1A_1B_1$ structure (Fig. 6.1(e)), M_I cannot be accommodated within the Al layers and instead it forms an antisite (M_A). Consequently, it is expected that the defect recovery process in $M_1A_1B_1$ is poor because of the formation of immobile antisites, which prevent Al_I from occupying and recombining with the V_{Al} sites, which has been already taken by the unstable M_I. In contrast, all the ten MAB phases that have one-Al-atomic layers ($M_2A_1B_2$) were found to have stable M_I within their Al layers. In Fig. 6.2(c), we show the atomic structure of Cr_2AlB_2 with Cr_I (③) before the relaxation, as an example for $M_2A_1B_2$. Before the relaxation, a Cr atom was introduced as an interstitial at the center of an octahedron consisting of four Al atoms and two Cr atoms. After the relaxation, the M_I stays at the center of the octahedron, as shown in Fig. 6.2(d), while the nearby Cr and Al atoms are shifted to accommodate the interstitial. The same mechanism was found in all the $M_2A_1B_2$ considered in this chapter, and no formation of antisite was observed.

These results generalize the previous finding on MoAlB and Fe_2AlB_2 (Chapter 3) and supports the hypothesis that MAB phases that have two-Al-atomic layers ($M_1A_1B_1$) cannot accommodate M_I in their Al layers (and therefore are expected to have poor defect recovery), while MAB phases with one-Al-atomic layers ($M_2A_1B_2$) can accommodate stable interstitials.

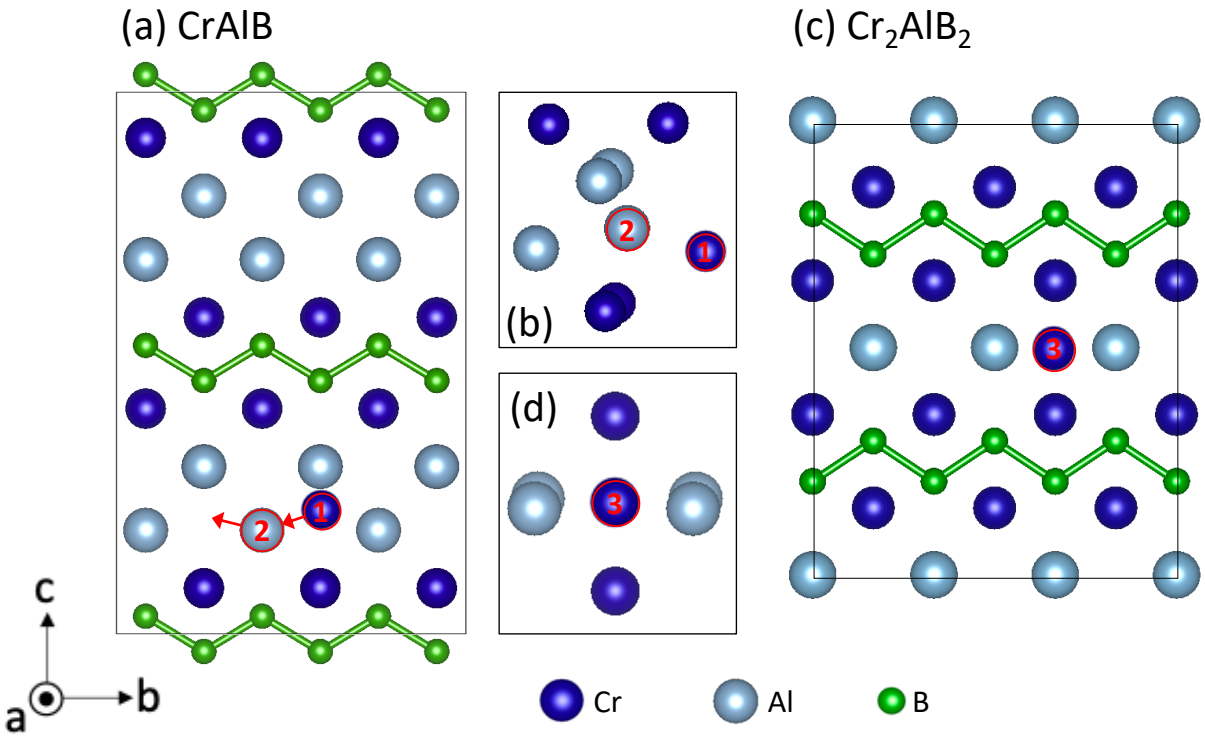

Figure 6.2 (a) CrAlB with Cr_I before the relaxation, (b) configuration of Cr_I in CrAlB after the relaxation, (c) Cr_2AlB_2 with Cr_I before the relaxation, and (d) configuration of Cr_I in Cr_2AlB_2 after the relaxation.

6.3.2 Absence of Al layers (M_1B_1) vs. presence of Al layers ($M_2A_1B_2$)

In Chapter 4, I showed that the defect recovery processes are more efficient in CrB than in the corresponding ternary, Cr_2AlB_2. In the study, we found that the absence of Al layers in CrB plays a crucial role in their superior defect recovery processes, specifically reducing the migration energies of M_I and the recombination barriers of B FPs. Here, I first test the hypothesis that M_I migrates faster in M_1B_1 than in $M_2A_1B_2$, and secondly, test the hypothesis that the recombination barriers of B FPs in M_1B_1 are lower than those in $M_2A_1B_2$. By calculating the defect kinetics in M_1B_1 and $M_1A_1B_1$ with different transition metal elements, I generalize the findings on CrB and Cr_2AB_2 systems to M_1B_1 and $M_2A_1B_2$.

I tested the hypothesis with 14 M_1B_1 and 14 $M_2A_1B_2$ (M = Cr, Fe, Hf, Mn, Mo, Ni, Rh, Ru, Sc, Tc, Ti, V, W, Zr). For each M_1B_1 (Fig. 6.1(a)) tested here, an M atom was located as an interstitial between two M layers at the center of a tetrahedron consisting of four M atoms (see Fig. 6.3(a)). We calculated the migration energies of M_I in M_1B_1 with the migration path depicted in Fig. 6.3(b). Note that

the considered interstitial position and migration path were found to be the most stable interstitial configuration and the fastest migration path in CrB (Chapter 5). For $M_2A_1B_2$ (Fig. 6.1(c)), I considered the interstitial configuration discussed in Section III-I (Fig. 6.2(d)). I calculated the migration energies of M_I along the *a*- and *b*-axis (Fig. 6.2(d)) and plotted the lowest migration energies in Fig. 6.3(c). I found that the migration energy of M_I in M_1B_1 (blue) is lower than that of M_I in the corresponding $M_2A_1B_2$ (red), except for M = Mo, Tc, and Zr. The lower migration energies in M_1B_1 can be explained based on the differences in the migration path, as follows. As depicted in Fig. 6.3(b), when migrating in the binaries, the M_I moves along the *a*-axis into one of the nearest M lattice sites, and at the same time, it pushes ("kicks out") the M atom that has occupied the lattice site into a nearest equivalent interstitial site. In contrast, in $M_2A_1B_2$, M_I, which forms within an Al layer (see Fig. 6.2(d)), migrates by hopping directly between symmetry equivalent sites without switching positions with lattice atoms. Because the direct hopping in general requires more energy compared with the "kick-out" mechanism, it makes physical sense that the migration energies of M_I in $M_2A_1B_2$ is higher. For the ternaries with M = Mo, Tc, and Zr for which the migration energies were found lower than those in the corresponding binaries, the most stable interstitial does not form within Al layers and thus the migration mechanism is different from the other ternaries. In these systems, M_I forms a M dumbbell within a M layer and migrates similarly as M_I in M_1B_1: M_I kicks out a nearby M atom into a nearest equivalent interstitial site and takes the lattice site of the kicked-out M atom. Finally, our results support the hypothesis that M_I in M_1B_1 migrates faster than M_I in $M_2A_1B_2$.

It is worth mentioning that the faster migration of M_I in M_1B_1 is a key factor contributing to the superior recovery processes of the binaries. For a FP to recombine, either the vacancy or the interstitial has to be mobile, and the recombination barrier has to be low enough to be overcome at a given temperature. We have previously found that in both Cr-B binary and Cr-Al-B ternary systems the migration of V_{Cr} is unlikely (migration energy: >3.1 eV for Cr-B and >4.7 eV for Cr-Al-B), and the recombination of Cr FPs is barrierless in both the Cr-B and the Cr-Al-B systems due to the defect pair positioned close enough to easily recombine. Also, in the other systems with M = Fe, Mo, the migration

energies of V_M are found to be 3.34 eV (Fe_2AlB_2) and 5.27 eV (MoAlB), while the recombination of M FPs in Fe_2AlB_2 is barrierless (in MoAlB, M_I is unstable, discussed in Chapter 3)[144]. Therefore, the migration of M_I likely controls the recombination processes of M FPs, in which the absence of Al layers in the binaries helps lower the temperature required to recover defects.

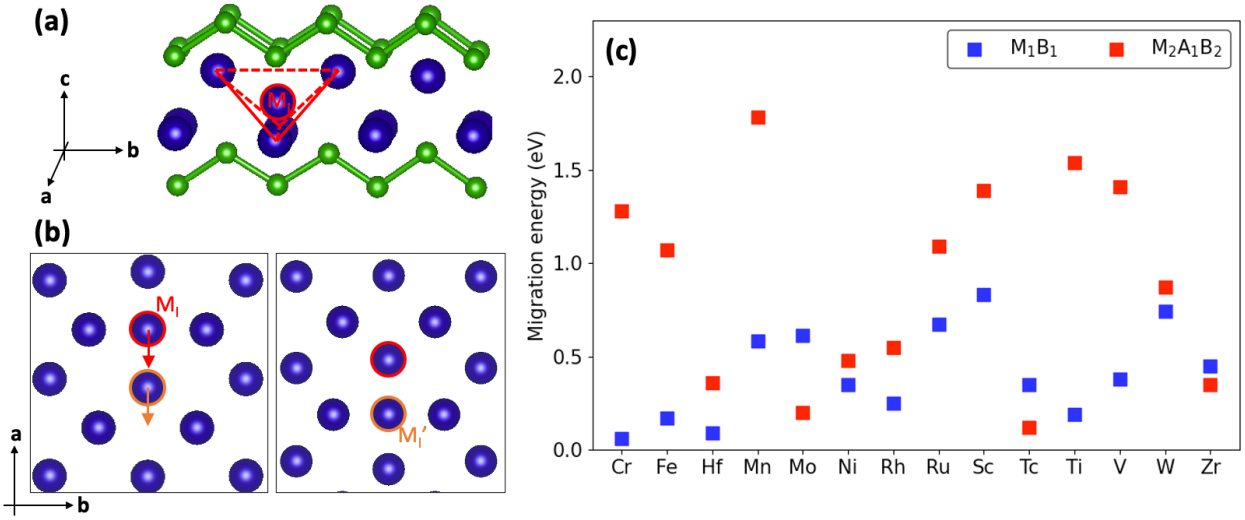

Figure 6.3 (a) configuration of M_I in M_1B_1, (b) migration path of M_I in M_1B_1, (c) migration energies of M_I in M_1B_1 and $M_2A_1B_2$.

The presence/absence of Al layers can affect the recombination of B FP as well as the migration of M_I. In Chapter 5, I found that the recombination of B FPs in CrB is barrierless, whereas the recombination process has a barrier of 1.30 eV in Cr_2AlB_2. This discrepancy is attributed to the absence of Al layers in CrB, and I hypothesized that the recombination barriers of B FPs in M_1B_1 are lower than those in $M_2A_1B_2$, due to the absence of Al layers in M_1B_1.

To test this hypothesis, I calculated the recombination barriers of B FPs in M_1B_1 and $M_2A_1B_2$ with M = Cr, Fe, Hf, Mn, Mo, Ni, Rh, Ru, Sc, Tc, Ti, V, W, Zr and plotted the results in Fig. 6.4. In M_1B_1, as depicted in Fig. 6.4(a), the B_I considered here is a B bridge that connects two neighboring B chains, which is the most stable B_I configuration in CrB. For $M_2A_1B_2$, I considered the B_I configuration depicted in Fig. 6.4(b), which is the most stable B_I in $Cr_2A_1B_2$. In Fig. 6.4(c), I plotted the calculated

recombination barriers of B FPs in M_1B_1 (circle, blue) and $M_2A_1B_2$ (circle, red). In all the tested systems, the recombination barriers of B FPs are lower in M_1B_1 compared with the corresponding $M_2A_1B_2$ ternary, and in most of the binaries (except for HfB and ZrB), the B FP recombination is barrierless. The barrierless or very low barrier processes in M_1B_1 are attributed to the fact that in M_1B_1 the B_I and V_B are close enough to each other (see Fig. 6.4(a)). In contrast, in $M_2A_1B_2$, the recombination barriers of B FPs are mostly higher than 1 eV, except for M = Ni, Rh, Sc where the barrier is around 0.5 eV. The higher barriers in $M_2A_1B_2$ are likely due to the fact that B_I and V_B are separated from each other by the M layer (see Fig. 6.4(b)), and also because more atoms are required to shift their positions during the recombination process. This result supports our hypothesis that the recombination barriers of B FPs in M_1B_1 are lower than those in $M_2A_1B_2$.

It should be pointed out that the recombination barriers of B FPs primarily determine if the B FPs can recombine. For a FP to recombine, either the vacancy or the interstitial has to be mobile, and the recombination barrier has to be low enough to be overcome at a given temperature. From the studies on MoAlB, Fe_2AlB_2, three Cr-B and three Cr-Al-B systems in Chapter 3 and Chapter 5, I found that the V_B is mobile in the studied systems with the migration energies ranging from 0.50 eV to 0.93 eV, indicating that the B FPs can recombine as long as the B FP recombination barrier is low enough. Therefore, the absence of Al layers in M_1B_1 helps the recombination processes of B FPs by lowering the recombination barriers.

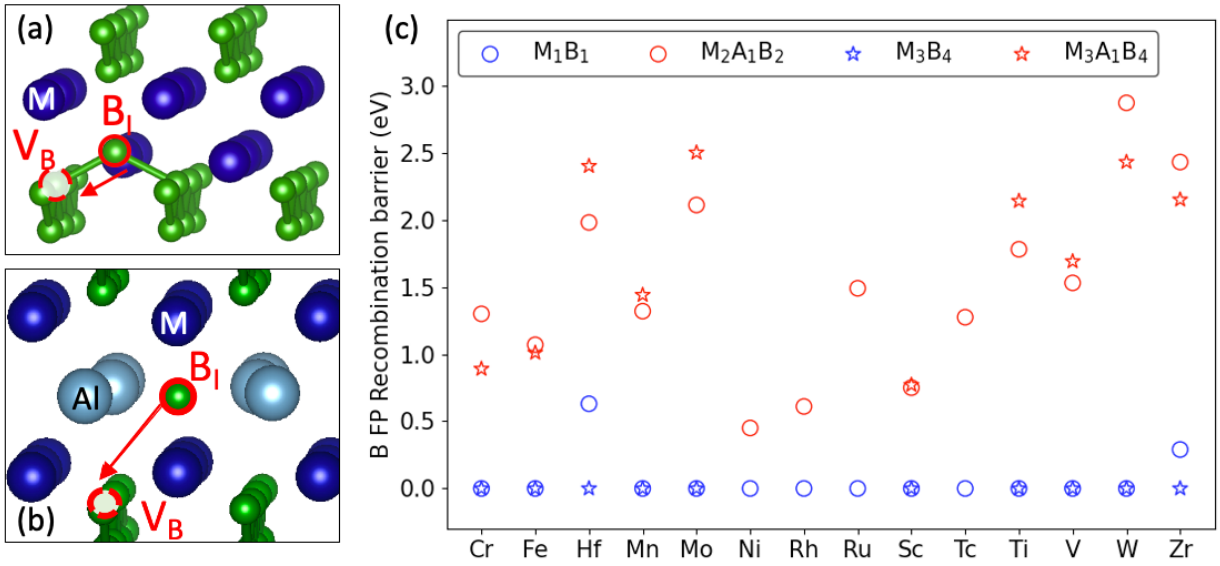

Figure 6.4 Configuration of B FPs (a) in M_1B_1 and M_3B_4 and (b) in $M_2A_1B_2$ and $M_3A_1B_4$, with the red arrow indicating the recombination path. (c) Recombination barriers of B FPs in M_1B_1, M_3B_4, $M_2A_1B_2$, and $M_3A_1B_4$.

6.3.3 Absence of Al layers (M_3B_4) vs. presence of Al layers ($M_3A_1B_4$)

In Chapter 5, I also compared Cr_3B_4 and Cr_3AlB_4, in which the B networks form B rings, and looked into the effects of Al layers on the defect recovery processes. As reported in Table 5.1 and Table 5.2, the absence of Al layers in Cr_3B_4 helps the B FP recombination by removing the recombination barrier (i.e., barrierless), whereas the barrier is 0.9 eV in Cr_3AlB_4. Based on the finding I hypothesized that the recombination barriers of B FPs in M_3B_4 are lower compared with those in $M_3A_1B_4$. I tested the hypothesis by calculating the B FP recombination barriers in M_3B_4 and $M_3A_1B_4$ with M = Cr, Fe, Hf, Mn, Mo, Sc, Ti, V, W, Zr and plotted the results in Fig. 6.4(c). The same principle we discussed in 6.3.2 (M_1B_1 vs. $M_2A_1B_2$) applies here as well. M_3B_4 shares with M_1B_1 the local environment where B FPs form and recombine (Fig. 6.4(a)), and $M_3A_1B_4$ shares with $M_2A_1B_2$ (Fig. 6.4(b)). As shown in Fig. 6.4(c), the recombination barriers of B FPs in M_3B_4 are all barrierless (star, blue) whereas the barriers in $M_3A_1B_4$ (star, red) are mostly higher than 1 eV. As discussed in M_1B_1 vs. $M_2A_1B_2$, this difference is attributed to the fact that B FPs in the binaries are close enough to recombine each other whereas B FPs in the ternaries are separated from each other by the M layers.

Unlike the B FP recombination processes, which are consistent in M_1B_1 vs. $M_2A_1B_2$ and M_3B_4 vs. $M_3A_1B_4$, the effects of Al layers on the migration of M_I in M_3B_4 vs. $M_3A_1B_4$ are different from M_1B_1 vs. $M_2A_1B_2$. In Chapter 5, I discussed the role of the Al layers in Cr_3B_4 and Cr_3AlB_4. In Cr_3B_4, the most stable Cr_I was found within B rings (Ⓑ in Fig. 6.5(a)) with the migration energy of 1.6 eV, and the second stable was found in the Cr layers (Ⓐ in Fig. 6.5(a)) with the migration energy of 0.1 eV. Their formation energy difference (ΔE_f) was calculated to be 0.7 eV, which necessitates to consider the second stable Cr_I as well as the most stable one. In Cr_3AlB_4, the most stable Cr_I was found in the Al layers (© in Fig. 6.5(b)) with the migration energy of 1.3 eV, and its formation energy is much lower ($\Delta E_f = 1.4$ eV) than the second stable interstitial found in B rings (Ⓓ in Fig. 6.5(b)). This suggests that when comparing M_3B_4 and $M_3A_1B_4$, one needs to take into account the formation of M_I within the B rings (Ⓑ and Ⓓ in Figs. 6.5(a) and (b), respectively) as well as within the M/A layers (Ⓐ and © in Figs. 6.5(a) and (b), respectively), which makes it difficult to define a general effect of the Al layers in M_3B_4 and $M_3A_1B_4$. Hence, I provide the migration energies of M_I in M_3B_4 and $M_3A_1B_4$ (M = Cr, Fe, Hf, Mn, Mo, Sc, Ti, V, W, Zr) to show the effect of the Al layers in each system, rather than trying to find a general trend in the effects of the Al layers. In Fig. 6.5(c), I plotted the migration energies of the most stable interstitials in M_3B_4 and $M_3A_1B_4$, and the migration energies of the second stable interstitials only if ΔE_f between the most and second stable interstitials is smaller than 0.7 eV. Note that in M_3B_4, depending on M, the most stable M_I could form in either Ⓐ or Ⓑ in Fig. 6.5(a), whereas in $M_3A_1B_4$, the most stable M_I is always found at © in Fig. 6.5(b). With M = Hf, Sc, Ti, V, W, Zr, the migration energies of M_I are lower in M_3B_4, i.e., the absence of Al layers help lower the migration energies of M_I. In contrast, with M = Cr, Fe, Mn, and Mo, the presence of Al layers helps the M_I migration process by lowering the migration energies. In M_3B_4 with M = Cr and Mo, although the second most stable M_I can migrate fast in their M layers (Ⓐ in Fig. 6.5(a)), the migration energies of the most stable interstitial formed in their B-ring layers (Ⓑ in Fig. 6.5(a)) are higher than in their corresponding MAB phases.

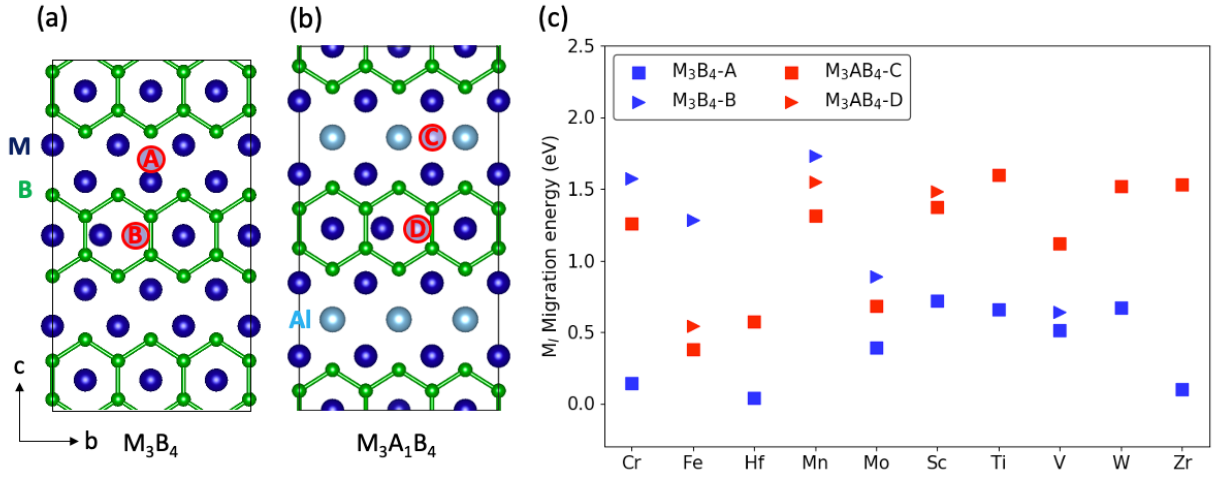

Figure 6.5 Locations of the most and the second stable M_I in (a) M_3B_4 and (b) $M_3A_1B_4$. (c) Migration energies of the stable M_I.

6.3.4 Effects of the type of transition metal elements

In my previous studies on Fe_2AlB_2 (Chapter 3) and Cr-Al-B MAB phases (Chapter 5), I found that in these systems, the weaker the M-B bonds the lower the B FP recombination barrier. I hypothesize that this trend is general. To test this hypothesis, I investigate the B FP recombination processes in MAB phases with different transition metal elements (and hence, different M-B bond strengths).

Specifically, I calculated the bond separation energies as a measure of the bond strengths in 24 MAB phases ($M_2A_1B_2$ and $M_3A_1B_4$) and then plotted the bond separation energy against the recombination barriers of B FPs. The results are shown in Fig. 6.6, where we considered the bond separation energies of the M-B bond (Fig. 6.6(a)), M-A bond (Fig. 6.6(c)), and B-B bond (Fig. 6.6(d)) in $M_2A_1B_2$ (closed circles) and $M_3A_1B_4$ (open circles). The best correlation of the B recombination barrier is found with the strength of the M-B bond. In Fig. 6.6(b), I explain this correlation with the B FP recombination processes in $M_2A_1B_2$ and $M_3A_1B_4$. When B_I is moving toward a V_B site to recombine, nearby atoms need to move aside to make room for the interstitial. During this process, the stronger (or stiffer) the bond, the higher the energy cost required to move the neighboring atoms, which makes the

recombination barrier higher. Therefore, it can be expected that MAB phases with weaker M-B bonds will likely have a lower recombination barrier of B FPs, as we found (e.g., Ni_2AlB_2 in Fig. 6.6(a)).

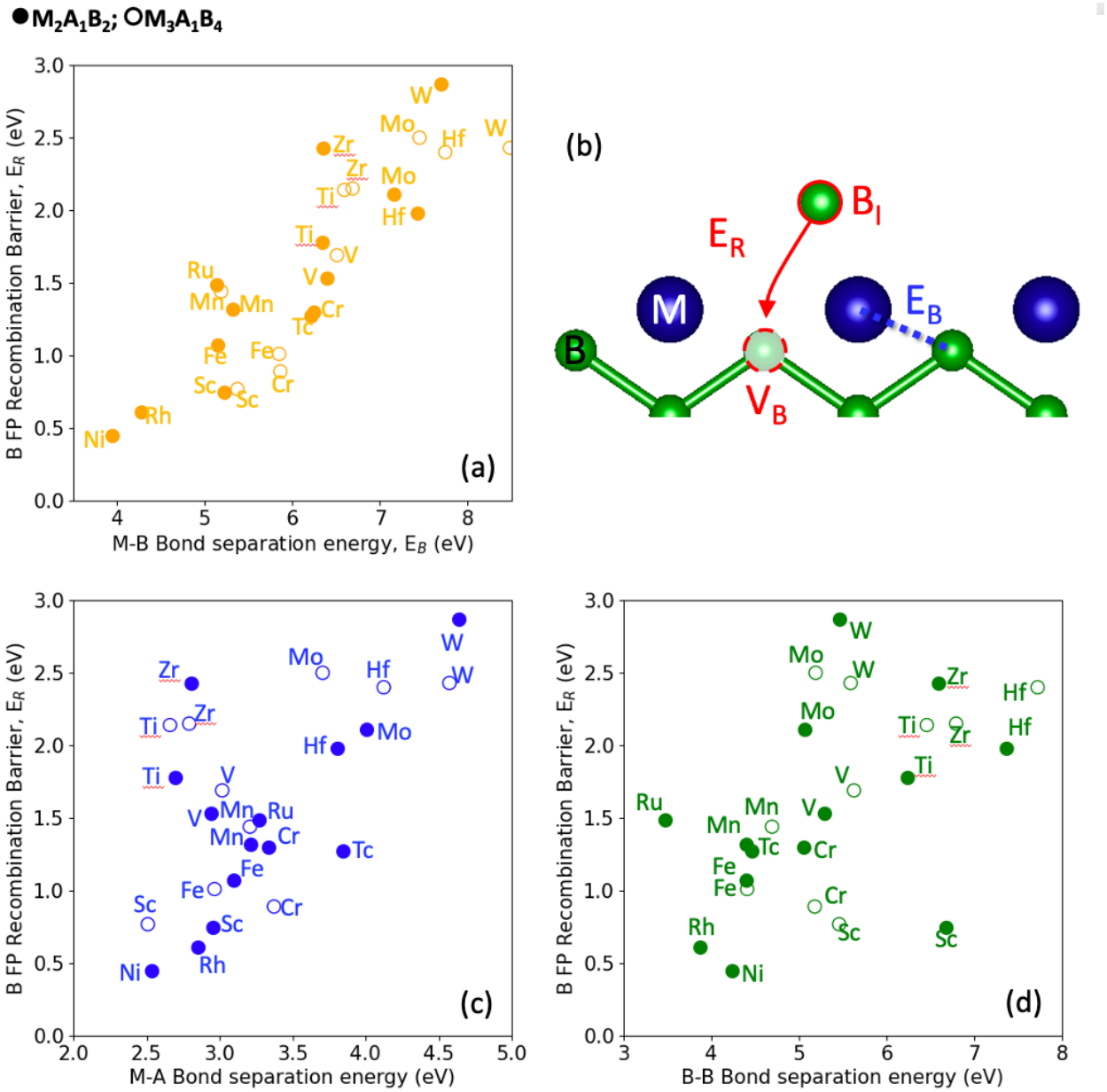

Figure 6.6 (a) B FP recombination barriers (E_R) versus M-B bond separation energies (E_B), (b) schematic picture of B FP recombination process in $M_2A_1B_2$ and $M_3A_1B_4$, (c) E_R versus M-A bond separation energies, and (d) E_R versus B-B bond separation energies.

6.3.5 TMBs in nuclear reactor applications

I have so far discussed the hypotheses regarding the defect recovery processes in binary TMBs (M_1B_1, M_3B_4) and ternary TMBs ($M_1A_1B_1$, $M_2A_1B_2$, $M_3A_1B_4$). It is interesting to consider how the defect recovery processes could be related to applications of the TMBs. In nuclear reactor applications, where defects are induced by radiation, the defects have to be recovered in order to maintain the crystalline structure and the properties of materials that depend on defect densities. Here, based on the kinetic data, I consider possibility of M_1B_1, M_3B_4, $M_2A_1B_2$ and $M_3A_1B_4$ as materials for nuclear reactor applications. I exclude $M_1A_1B_1$ because of the clear impact (i.e., unstable M_I) of the two-Al-atomic layers in $M_1A_1B_1$ discussed in 6.3.1. In Fig. 6.7, I plotted the defect kinetics data discussed in this Chapter: the migration energies of M_I and the recombination barriers of B FPs. Note that the migration energy of M_I and the recombination barrier of B FPs are likely the key factors controlling the defect recovery processes, as discussed in 6.3.2 and 6.3.3.

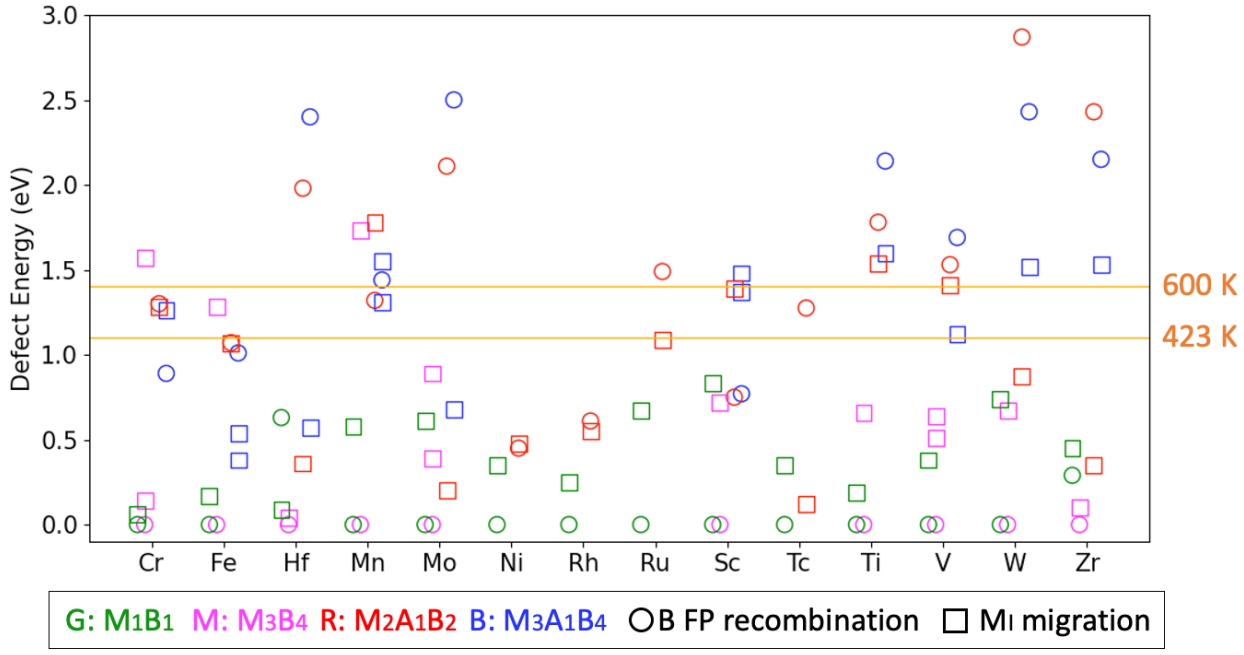

Figure 6.7 Summary of the defect kinetics values that control the recovery processes of radiation-induced defects in the TMBs: M_1B_1 (green), M_3B_4 (magenta), $M_2A_1B_2$ (red), and $M_3A_1B_4$ (blue).

Based on Fig. 6.7, in Table 6.1 I tabulated the systems where the FPs are expected to recover at typical temperatures of nuclear reactors (e.g., supercritical water-cooled reactor, light water reactor) in operation. In order to determine whether a defect is able to be recovered at a given temperature, I calculated the hopping rate with the pre-exponential factor of 10^{13} s^{-1} assuming that it has to move at least 1 nm over a reasonable time period (here assumed to be 60 s), and I indicate the temperatures next to the corresponding energies in Fig. 6.7. For instance, at 423 K, FPs in CrB are likely recombined, since Cr FPs can be removed by the fast Cr_I migration and B FPs are allowed to recombine due to the low B recombination barrier. On the other hand, in Cr_2AlB_2, Cr_I is immobile at 423 K and the B FP recombination barrier is too high to be overcome at the temperature. Although many of the binary TMBs and some of ternary TMBs are found promising in terms of their defect recovery processes, as shown in Table 6.1, one should consider not only the radiation-induced defect recovery processes but the oxidation resistance of materials for nuclear reactor applications. It is generally known that binary TMBs exhibit poor oxidation resistance, especially at high temperature compared with ternary MAB phases[143,161]. Therefore, I rather focus more on the ternaries in Table 6.1 where FPs are expected to easily recombine, which are Cr_2AlB_2, Cr_3AlB_4, Fe_2AlB_2, Fe_3AlB_4, Ni_2AlB_2, Rh_2AlB_2, Sc_2AlB_2, and Tc_2AlB_2. Considering the cost of the metals, Cr_2AlB_2, Cr_3AlB_4, Fe_2AlB_2, Fe_3AlB_4 and Ni_2AlB_2 would be most promising. In fact, in Chapter 3 and Chapter 5, Fe_2AlB_2 and Cr_3AlB_4 have been already experimentally found to have a good resistance to radiation-induced amorphization[144].

Table 6.1 Binary and ternary TMBs where FPs are expected to easily recombine at each temperature.

M	423 K	600 K
Cr	M_1B_1	M_1B_1, $M_2A_1B_2$, $M_3A_1B_4$
Fe	M_1B_1, $M_2A_1B_2$, $M_3A_1B_4$	M_1B_1, M_3B_4, $M_2A_1B_2$, $M_3A_1B_4$
Hf	M_1B_1, M_3B_4	M_1B_1, M_3B_4
Mn	M_1B_1	M_1B_1
Mo	M_1B_1, M_3B_4	M_1B_1, M_3B_4
Ni	M_1B_1, $M_2A_1B_2$	M_1B_1, $M_2A_1B_2$
Rh	M_1B_1, $M_2A_1B_2$	M_1B_1, $M_2A_1B_2$
Ru	M_1B_1	M_1B_1
Sc	M_1B_1, M_3B_4	M_1B_1, M_3B_4, $M_2A_1B_2$
Tc	M_1B_1	M_1B_1, $M_2A_1B_2$
Ti	M_1B_1, M_3B_4	M_1B_1, M_3B_4
V	M_1B_1, M_3B_4	M_1B_1, M_3B_4
W	M_1B_1, M_3B_4	M_1B_1, M_3B_4
Zr	M_1B_1, M_3B_4	M_1B_1, M_3B_4

6.4 Conclusions

I investigated the defect recovery processes in binary and ternary TMBs considering the four topics: (1) the effects of the number of Al layers on the stability of M_I, the effects of Al layers on the migration energies of M_I and the recombination processes of B FPs (2) in M_1B_1 vs. $M_2A_1B_2$ and (3) in M_3B_4 vs. $M_3A_1B_4$, and (4) the effects of the type of M on the recombination barriers of B FPs. My DFT calculations showed that MAB phases with two-Al-atomic layers (i.e., $M_1A_1B_1$) cannot accommodate M_I, which immediately transform to an antisite (M_A), whereas MAB phases with one-Al-atomic layers (e.g., $M_2A_1B_2$) can accommodate M_I in the Al layers. I also found that M_I migrate slower and the recombination barriers of B FPs are higher in $M_2A_1B_2$ than in the corresponding binary (M_1B_1). In M_3B_4 and $M_3A_1B_4$, the impact of Al layers on the migration energies of M_I varies depending on the type of M, while the recombination barriers of B FPs in M_3B_4 are always lower than those in $M_3A_1B_4$. Based on the correlation between the M-B bond and the recombination barrier of B FP in $M_2A_1B_2$ and $M_3A_1B_4$, I found that having weaker M-B bonds is beneficial for the recombination processes of B FPs in the MAB phases. Finally, I analyzed the defect kinetics data to find TMBs promising for nuclear reactor applications in terms of defect recovery processes. Based on this analysis, MAB phases will have defect recovery

processes efficient enough to be considered for nuclear reactor applications. Combined with their good oxidation resistance, MAB phases will be promising for nuclear reactor applications. My study on the impacts of the transition metal and the structures on the defect recovery processes will be helpful in designing TMBs for applications where defect recovery processes are important.

CHAPTER 7

CHARGE-STATE TRANSITION LEVELS OF DEFECTS

The experimental part in this chapter was carried out by Dr. Łukasz Gelczuk and Daria Hlushchenko.

7.1 Introduction

Transition metal dichalcogenides (TMDs) have been extensively studied for semiconductor device applications, due to the direct bandgaps of two-dimensional (2D) TMDs with the general formula of MX_2 (M = Mo or W; X = S, Se, or Te). Specifically, 2D TMDs are considered to be promising for a variety of electronic, photonic, energy and sensing device applications that are more efficient than cutting edge silicon-based devices[76,79,83,177]. In addition, depending on their chemical compositions and structural configuration, TMDs can cover a wide range of bandgaps through the proper selection of metal and chalcogen species. Also, TMDs are easily combined with other 2D materials such as hexagonal boron nitride or graphene to form van der Waals (vdW) heterostructures, revealing unique properties such as large in-plane stability and enabling novel applications such as flexible electronics[178–181].

To critically assess TMDs for device applications, it is necessary to consider defects in these materials because a finite number of defects is always present and influences material properties and the performances of devices. For instance, Liu et al. reported an enhanced mobility of MoS_2-based field effect transistors when MoS_2 is annealed in sulfur[84], and it was expected that the improved device performance results from the removal of V_S[85]. In addition, when present in high concentration, defects significantly affect the electrical properties of materials in that free charge carriers trapped at defect levels cause Fermi level pinning at the contacts and affect the type of doping[182–184]. Also, Qiu et al. reported that the charge transport mechanism of MoS_2 in the low carrier density regime is caused by nearest-neighbor

hopping through V_S-induced localized gap states[185]. Therefore, to properly design TMD-based applications, it is critical to accurately determine the properties of defects in TMDs, including charge-state transition levels (CTLs).

The CLTs of defects in TMDs have been studied experimentally[85,186–196] and computationally[86–88,182,183,197], mostly focusing on MoS_2. Among various defects, V_S has been found to be the most stable intrinsic defect[85–87] in both bulk and 2D MoS_2, and computational studies have focused on the CTLs of V_S[86–88]. For example, in a density functional theory (DFT) based study, Komsa et al.[87] reported the defect chemistry and the CTLs of point defects in bulk and 2D MoS_2, and they found that the CTLs of V_S are similar in bulk and 2D MoS_2. More recently, Tan et al.[88] calculated the CTLs of V_S in bulk and 2D MoS_2, utilizing the electrostatic correction for 2D systems developed by Freysoldt and Neugebauer[198,199], which is considered as the most accurate electrostatic correction to date. However, none of the previous studies has used a method that accurately describes the bandgap to determine the CTLs, leading to difficulty in comparing with experimental CTLs, because experimental methods such as deep level transient spectroscopy (DLTS) provide information on CTLs referenced to the conduction band minimum (CBM). Moreover, considering the importance of the vdW interactions between the layers of bulk TMDs, it is critical to carefully choose an approach that is capable of well describing the vdW interactions within DFT. Especially, since the structural parameters, largely influenced by the vdW interactions, play a key role in determining the electronic structure and CTLs, use of the most accurate approach is expected to yield the best results. Recently, Tran et al.[104] found that rev-vdW-DF2 functional is highly accurate for weakly bound solids including TMDs. Overall, although theoretical CTLs have been reported, as we will show later, there have been discrepancies in the reported values and in many cases the predictions have not been validated experimentally. There is thus still room for improving the accuracy and reliability by combining state-of-the-art computational methods: selection of an optimized functional, electrostatic correction, and use of the correct bandgap[87].

Experimentally, the characterization of defects in TMDs has focused mostly on the intrinsic structural properties of MoS_2 at the atomic scale using high-resolution transition electron microscopy (HR

TEM)[85,86,185] or scanning tunneling microscopy (STM)[85,186–188]. Experimental investigations on the structures are often supported by first-principles calculations, which can help identify the nature of the defects. Indeed, systematic joint experimental-theoretical investigations have provided distinct evidences that V_S exists in MoS_2 and introduces CTLs inside the bandgap[85,86,185]. While STM is capable of studying both the structural and electronic properties of various types of defects on the surface of TMDs, TEM can only visualize the defect structure without providing direct access to the electronic properties of individual defects[188], such as their activation energy (i.e., CTL) or capture cross-section. There is also distinct inconsistency on the defect types revealed from STM and TEM experiments[85,86,185]. These problems arise mostly from the unclear differentiation of the STM contrast between the metal and chalcogen sublattices and the complicated convolution of electronic and geometric structures[188], as well as very limited capability in detecting defects beneath the surface[196]. Meanwhile, optical spectroscopic techniques, e.g., Raman or photoluminescence (PL) spectroscopy are also widely used to characterize defects in 2D layered materials, such as graphene or TMDs[189–193]. Because the change of Raman features with increase in the defect density is less sensitive in TMDs than in graphene, PL spectroscopy appears to be a more reliable and sensitive way to examine CTLs in TMDs. For example, Tongay et al. found a sub-bandgap emission peak in low-temperature PL spectra of 2D MoS_2 after α-particle irradiation, which the authors attributed to the emission from the CTLs of V_S[190]. Defect-related PL emissions were also observed in 2D WSe_2[191] and WS_2[192,193], attributed by the authors to the recombination of excitons bound to different types of native defects, mostly the chalcogen vacancies. Electrical characterization of defects has been limited as well, mainly due to the difficulties in getting good quality electrical contacts to 2D TMDs with reduced contact resistance[182,183,200]. Recently, significant progress has been made in creating high-quality electrical contacts, including use of metallic 2D materials as electrical contacts to semiconducting TMDs[200]. For example, in MoS_2/graphene heterojunction transistors, Kwak et al. found a deep donor level using the I-V measurement and related its origin to intrinsic or extrinsic donor sources such as V_S[194].

Despite many previous efforts, CTLs in 2D TMDs are still experimentally unknown or there are significant discrepancies between reports. Moreover, the reported experimental studies are mostly devoted to V_S in MoS_2, and the issue of other native defects (e.g., interstitials, antisites, and/or impurities) in other TMDs is generally neglected. To increase the usability of TMDs in device applications, the nature and the energy levels of defects should be well documented for better understanding, as it has been done for conventional semiconductors. Much better compatibility between theoretically predicted and experimentally determined CTLs of defects can be obtained from a direct measurement such as DLTS. It is technically challenging to apply DLTS to either bulk or 2D TMDs, owing to many known issues, such as requirement of good quality metal-semiconductor junction, high leakage currents, low series resistance, and a sufficient width of the depletion region[182–184,195,196]. We have recently reported a successful usage of DLTS for the direct probing of deep-level defects in bulk MoS_2 vdW crystal[195]. Standard DLTS temperature spectra revealed a single deep-level trap with the energy position inside the bandgap (~0.35 eV below from the CBM, very close to the values previously reported for V_S[86,190,193]). More recently, Ci et al. have also reported the results of DLTS and current transient spectroscopic (CTS) studies of deep levels in exfoliated multilayer MoS_2, WS_2 and their alloys, such as $Mo_{1-x}W_xS_2$[196]. For MoS_2 the authors found two DLTS peaks of majority carrier traps at ~0.3 eV and ~0.4 eV. By combining the DLTS/CTS results with DFT calculations and STEM imaging or photoconductivity measurements, the authors identified one trap as V_S and another as a metastable DX center[196].

In this chapter, we study the CTLs of native point defects in 2H-MX_2 (M = Mo or W; X = S, Se, or Te) experimentally and computationally in a consistent fashion. By combining state-of-the-art computational methods (which include optimized functional, electrostatic correction, and band alignment), we establish an accurate method to predict the CTLs of native point defects in the bulk MX_2. Simultaneously, we experimentally measure the defect levels using DLTS, which is a high-frequency capacitance transient technique, considered as a direct and accurate way to measure the CTLs of defects in semiconductors[201]. Finally, with the use of the computational methods validated by the DLTS

experiments in the bulk TMDs, we predict the CTLs of native point defects in the 2D TMDs and compare the results with the calculated CTLs in the bulk systems.

7.2 Methods

The bulk TMDs used in this chapter were commercially available vdW crystals (supplied by HQ Graphene), except for MoS_2 (obtained from 2D Semiconductors). Multilayer (~ 200μm thick) MoS_2, $MoSe_2$, $MoTe_2$, WS_2, and WSe_2 have a typical lateral size of about 5 mm, parallel to the hexagonal lattice plane. For DLTS and other temperature-dependent electrical measurements, the samples were mounted on a high quality (~0.8mm thick) printed circuit board holder with copper tracks, designed specifically for our cryostats. Au and Ni circular contacts (~0.1 mm^2 area), deposited on the top of each sample through a shadow mask in vacuum by electrolithography, were used as a Schottky barrier contact, and a large area (10-12 mm^2) Au bottom electrode was used as an ohmic contact. The ohmic contact was additionally annealed at 350 °C in Ar atmosphere to ensure nonrectifying electrical conductivity through the metal-semiconductor junction (i.e., ohmic-like behavior).

We used a hand-made Laplace DLTS system, designed to measure electrical characteristics (i.e., LDLTS, DLTS, I-V, and C-V curves) of semiconductors in a wide temperature range. The samples were mounted in a liquid-nitrogen-cooled Janis VPF-475 cryostat, where the temperature is precisely tuned by Lakeshore 331 temperature controller within the range of 80K to 480K. High-frequency capacitance transients were measured by means of Boonton 7200 capacitance bridge, operating at the frequency of 1 MHz and the AC voltage with the amplitude of ~30mV superimposed onto the DC reverse bias. In turn, the current-voltage characteristics were measured by 2601 A Keithley source measure unit instrument.

For consistency, the DLTS measurements were performed at the same bias conditions (i.e., the steady-state small reverse bias $V_R = -1$ V and the filling pulse voltage (V_P)), which reduces the reverse bias to 0V and allows the traps to be filled with free electrons. Next, the capacitance transients related to the emission of majority carriers from the deep-level traps in the depletion region were recorded. The width of the filling pulse (t_P) was set to 1 ms and the emission rate window (RW) was equal to 50 sec^{-1}.

For such measurement conditions, the capacitance difference within the specified RW (i.e., DLTS signal) reaches the maximum at a specific temperature. In our DLTS system, a positive signal indicates that all the visible peaks correspond to the majority carrier traps with the energy levels measured from the CBM.

The energy position (E_T) of a CTL in relation to the CBM (E_C), called activation energy ($E_a = E_C - E_T$), and the apparent capture cross-section (σ_n) can be determined on the basis of the detailed balance equation[201,202]:

$$e_n = \sigma_n V_{th} N_C \exp\left(\frac{E_C - E_T}{k_B T}\right), \tag{7.1}$$

where e_n stands for the thermal emission rate of electrons from a deep-level into the conduction band at temperature T, v_{th} is the thermal velocity of the electrons, N_C is the effective density of states in the conduction band, and k_B is the Boltzmann's constant. Considering $v_{th} \propto T^{1/2}$ and $N_C \propto T^{3/2}$ and assuming the temperature independence of the capture cross section, Eq. 7.1 becomes a linear equation in the coordinate of $\ln(e_{n,p}/T^2)$ vs. $1/T$:

$$\ln\left(\frac{e_n}{T^2}\right) = \left(\frac{E_C - E_T}{k_B}\right)\frac{1}{T} + \ln(K\sigma_n), \tag{7.2}$$

where K is a known constant dependent on the electron effective mass. In the standard approach, this type of Arrhenius equation can be plotted by measuring a shift in the DLTS temperature peak position as a function of a thermal emission rate. Therefore, to construct the Arrhenius plots and to calculate the parameters of deep-level defects, the DLTS temperature spectra were measured in different rate windows with the range of 5 sec^{-1} to 2000 sec^{-1} under the same bias conditions. Ultimately, according to Eq. 7.2 and from the slope of the Arrhenius plots, one can obtain the activation energy of a deep-level defect, while its capture cross section is obtained from the intercept with the ordinate axis.

We performed DFT calculations using the Vienna Ab-initio Simulation Package[110] with the projector augmented wave method[127]. To optimize the geometry of the six TMDs (MoS_2, $MoSe_2$, $MoTe_2$, WS_2, WSe_2, WTe_2), different functionals were tested to find the one that most accurately describes the experimental lattice constants of the six TMDs. The tested functionals were PBE+D3[102], SCAN+rVV10[203], rev-vdW-DF2[106], PBE+rVV10L[204], PBEsol+rVV10s[205], optB88-vdW[206], and vdW-DF-

cx[207]. We set the plane-wave cutoff energy of 500 eV and Γ-centered Monkhorst-Pack *k*-point mesh of 10×10×2 with the energy tolerance of 1 meV/atom[128]. From the test of the different functionals, rev-vdW-DF2 was shown to exhibit the smallest error as compared with the experimentally determined values and, therefore, was selected as the functional of choice for the geometry optimization and the total energy calculations. Due to the well-known bandgap underestimation problem, for the band structures, we also performed hybrid functional calculations using Heyd, Scuseria, and Ernzerhof (HSE)[99] with the fraction of exact exchange adjusted such that the calculated bandgap agreed with the experimental bandgap. The total energies of pure systems and defective systems were calculated in 5×5×1 supercells with the *k*-point mesh size of 2×2×2. Spin orbit coupling was included for all the calculations in this chapter. For 2D calculations, all the computational methods were kept the same as in the bulk calculations in order to achieve results consistent with the bulk calculations, only with the *k*-point mesh reduced to 1 point in the direction perpendicular to the layer. The layers were separated by 25 Å of vacuum to prevent interactions between their periodic images.

The formation energy, $E^f[X^q](E_\mathrm{F})$, of a point defect *X* with the charge *q* was calculated as a function of Fermi energy E_F using the following equation,

$$E^f[X^q](E_\mathrm{F}) = E_\mathrm{tot}[X^q] - E_\mathrm{tot}[\mathrm{pure}] - \sum n_i\mu_i + q(E_\mathrm{VBM}[\mathrm{pure}] + E_\mathrm{F}) + E_\mathrm{EC} \quad (7.3)$$

where E_tot and E_VBM are the total energy and the valence band maximum (VBM) from the DFT calculation, respectively, n_i is the number of atoms added or removed as a defect, μ_i is the chemical potential of the defect element, and E_EC is the electrostatic correction term for the interaction of the defect with the periodic images, for which we used the scheme developed by Freysoldt et al.[198,199].

After calculating the formation energies, a modified band alignment method[208,209] was applied to correctly locate the CTLs using the following equation, along with the rev-vdW-DF2 calculated energies and the HSE calculated band structure,

$$E^d_\mathrm{MBA} = E^d + E_\mathrm{shift} + \beta\left(E_\mathrm{g} - E^d\right) \quad (7.4)$$

where E^d_{MBA} is the corrected CTL, E^d is the CTL obtained from Eq. 7.3, E_{shift} is the VBM difference between the rev-vdW-DF2 and HSE calculations, E_{g} is the HSE bandgap, and β is –0.14 as determined by Polak et al.[209].

7.3 Results and discussion

7.3.1 CTLs in bulk TMDs

Our successful prediction of the CTLs is attributed to the combination of state-of-the-art computational methods: (1) the selection of the optimized functional, (2) the electrostatic correction, and (3) the band alignment. In order to find a functional that best describes the six TMD systems, we tested the different functionals. Since vdW interactions play a key role in establishing the interplanar separation in bulk TMDs, it is expected that functionals that can describe those interactions correctly would perform best. The lattice constants of the six TMDs calculated with rev-vdW-DF2 agree best with the previously reported experimental lattice constants[104,210–215] and are tabulated along with the dielectric constants and the bandgaps in Table 7.1. Although SCAN+rVV10 has yielded accurate results as well[104] and has been used to study the CTLs of defects in MoS_2[88], when it comes to the six TMDs studied here, we found that rev-vdW-DF2 (mean absolute error (MAE): 0.49 %) is slightly better than SCAN+rVV10 (MAE: 0.64 %). The lattice constants calculated using the other functionals are provided in 7.5.1. Note that, as expected, the rev-vdW-DF2 calculations underestimated the bandgaps. The HSE functional was used to calculate the bandgaps, as it is regarded as the most suitable for calculating bandgaps. To allow the most accurate comparison with our experimental measurements, the fraction of exact exchange used in HSE was adjusted to precisely reproduce the experimentally observed values of the bandgaps: 0.16 (MoS_2), 0.13 ($MoSe_2$), 0.25 ($MoTe_2$), 0.187 (WS_2), 0.18 (WSe_2), and 0.18 (WTe_2). For WTe_2, we used the average of the five other systems, since the experimental bandgap of 2H-WTe_2 is not known.

Table 7.1 Lattice constants (a and c), dielectric constants ($\varepsilon_\perp$ and $\varepsilon_\parallel$), bandgaps (E_g) calculated using rev-vdW-DF2; bandgaps obtained from the HSE calculations; and previously reported experimental bandgaps (Exp). The bulk lattice and dielectric constants were used for 2D calculations as well.

a, c in Å E_g in eV	MoS_2	$MoSe_2$	$MoTe_2$	WS_2	WSe_2	WTe_2
a	3.17	3.30	3.54	3.17	3.30	3.54
c	12.4	13.0	14.1	12.4	13.1	14.1
$\varepsilon_\perp$	6.56	7.92	10.7	6.10	7.46	9.80
$\varepsilon_\parallel$	15.3	16.9	20.2	13.9	15.4	18.9
$E_{g,bulk}$ (rev-vdW-DF2)	0.86	0.82	0.69	0.98	0.93	0.65
$E_{g,bulk}$ (HSE)	1.23	1.09	1.00	1.35	1.20	0.97
$E_{g,bulk}$ (Exp)[216,217]	1.23	1.09	1.00	1.35	1.20	-
$E_{g,2D}$ (rev-vdW-DF2)	1.65	1.38	0.97	1.61	1.28	0.77
$E_{g,2D}$(HSE)	1.90	1.57	1.10	2.01	1.63	1.15
$E_{g,2D}$ (Exp)	1.87-1.92	1.52-1.58	1.10	1.98-2.05	1.62-1.66	1.15

The electrostatic interaction of the defect with its periodic images was corrected using the correction scheme developed by Freysoldt *et al.*[198,199], which has been considered the best to date[218]. Recently, the scheme developed by Freysoldt *et al.* has been extended to the electrostatic interactions in 2D systems, and it has been applied to 2D MoS_2[88]. Because of the documented performance of this scheme and the fact that it allows the correction of the electrostatic interaction consistently both in bulk and 2D TMDs, we adopted this scheme to study the CTLs of defects.

Next, the underestimation of the bandgaps caused by the use of rev-vdW-DF2 was remedied by applying a modified band alignment method[209], which is modification of the conventional band alignment method[208]. In this approach, the positions of CTLs as well as the VBM and CBM are shifted based on the relative positions of band edges calculated with rev-vdW-DF2 and hybrid functionals (HSE here), with an additional bandgap-dependent correction. The computationally determined CTLs aligned with the different band alignment methods are tabulated in 7.5.2 for all the levels experimentally found in this study. Overall, the modified band alignment provides the best matches to the CTLs found in our experiments.

The formation energies of intrinsic point defects in the six bulk TMDs calculated at the chalcogen-rich condition are shown in Fig. 7.1. It has been reported that the most stable defect in MoS_2 is V_S[87]. The same qualitative trend is found in our results not only of MoS_2 but also for the other systems,

where the chalcogen vacancy is the defect with the lowest formation energy. In Fig. 7.1 we also show the CTLs of intrinsic point defects in the six bulk TMDs, and in Table 7.2, we tabulate the values of the CTLs referenced to the CBM, since these are the quantities that are directly comparable to the values measured by DLTS. For V_S, only the $0/-1$ transitions were found to be inside the bandgap in the bulk systems. Note that all the $0/-1$ transitions were found close to the CBM. In addition, we found that the location of the $0/-1$ transition with respect to the CBM is virtually unaffected by the selection of the metal (M = Mo, W): MS_2 (0.34-0.36 eV below the CBM), MSe_2 (0.12-0.13 eV below the CBM), and MTe_2 (0.22 eV below the CBM). The metal vacancy, found to be the second most stable over the broad range of Fermi energy in each of the six systems, has three CTLs inside the bandgap: $0/-1$, $-1/-2$, and $-2/-3$ in all the systems. None of the CTLs of chalcogen interstitial were found inside the bandgap in MoS_2, $MoSe_2$, and WSe_2.

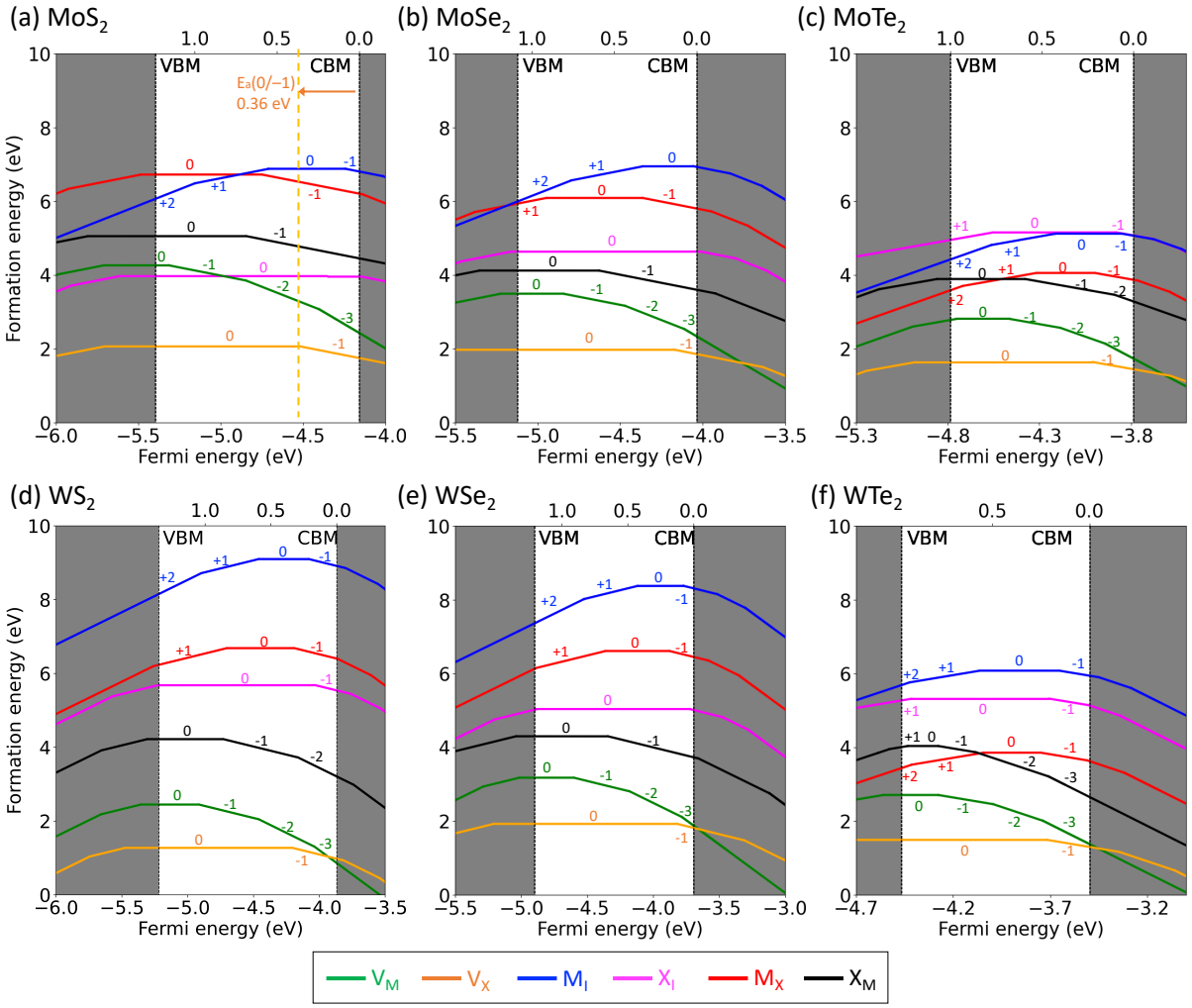

Figure 7.1 Defect formation energies and CTLs calculated at the chalcogen-rich condition as a function of Fermi energy in bulk (a) MoS_2, (b) $MoSe_2$, (c) $MoTe_2$, (d) WS_2, (e) WSe_2, and (f) WTe_2.

Table 7.2 CTLs of defects identified in Fig. 7.1 (M = Mo, W; X = S, Se, Te). The levels are referenced to the CBM.

Defect	MoS_2	$MoSe_2$	$MoTe_2$	WS_2	WSe_2	WTe_2
V_M	1.16 (0/−1) 0.69 (−1/−2) 0.24 (−2/−3)	0.8 (0/−1) 0.44 (−1/−2) 0.08 (−2/−3)	0.68 (0/−1) 0.40 (−1/−2) 0.15 (−2/−3)	1.05 (0/−1) 0.59 (−1/−2) 0.17 (−2/−3)	0.91 (0/−1) 0.49 (−1/−2) 0.09 (−2/−3)	0.78 (0/−1) 0.50 (−1/−2) 0.24 (−2/−3)
V_X	0.36 (0/−1)	0.13 (0/−1)	0.22 (0/−1)	0.34 (0/−1)	0.12 (0/−1)	0.22 (0/−1)
M_I	1.0 (+2/+1) 0.55 (+1/0) 0.08 (0/−1)	0.76 (+2/+1) 0.33 (+1/0)	0.78 (+2/+1) 0.43 (+1/0) 0.06 (0/−1)	1.03 (+2/+1) 0.59 (+1/0) 0.21 (0/−1)	0.83 (+2/+1) 0.43 (+1/0) 0.08 (0/−1)	0.93 (+2/+1) 0.57 (+1/0) 0.15 (0/−1)
X_I	None	None	0.77 (+1/0) 0.09 (0/−1)	0.16 (0/−1)	None	0.92 (+1/0) 0.21 (0/−1)
M_X	0.59 (0/−1)	0.91 (+1/0) 0.33 (0/−1)	0.93 (+2/+1) 0.53 (+1/0) 0.21 (0/−1)	0.84 (+1/0) 0.32 (0/−1)	0.67 (+1/0) 0.18 (0/−1)	0.92 (+2/+1) 0.55 (+1/0) 0.25 (0/−1)
X_M	0.68 (0/−1)	0.59 (0/−1)	0.59 (0/−1) 0.10 (−1/−2)	0.86 (0/−1) 0.29 (−1/−2)	0.65 (0/−1)	0.94 (+1/0) 0.78 (0/−1) 0.60 (−1/−2) 0.21 (−2/−3)

In our experiments, high quality synthetic TMD bulk crystals (2H phases) were analyzed with DLTS. Only WTe_2 was not considered for further electrical measurements, because the crystal exhibited native semi-metallic properties with the typical charge carrier density of $\sim 10^{20} cm^{-3}$ [215,219]. All the other samples were *n*-type semiconductors, and their Schottky barrier devices were fabricated in order to perform DLTS experiments. The quality of the Schottky diodes has been initially checked by temperature-dependent current-voltage (I-V) and capacitance-voltage (C-V) characteristics (provided in 7.5.3).

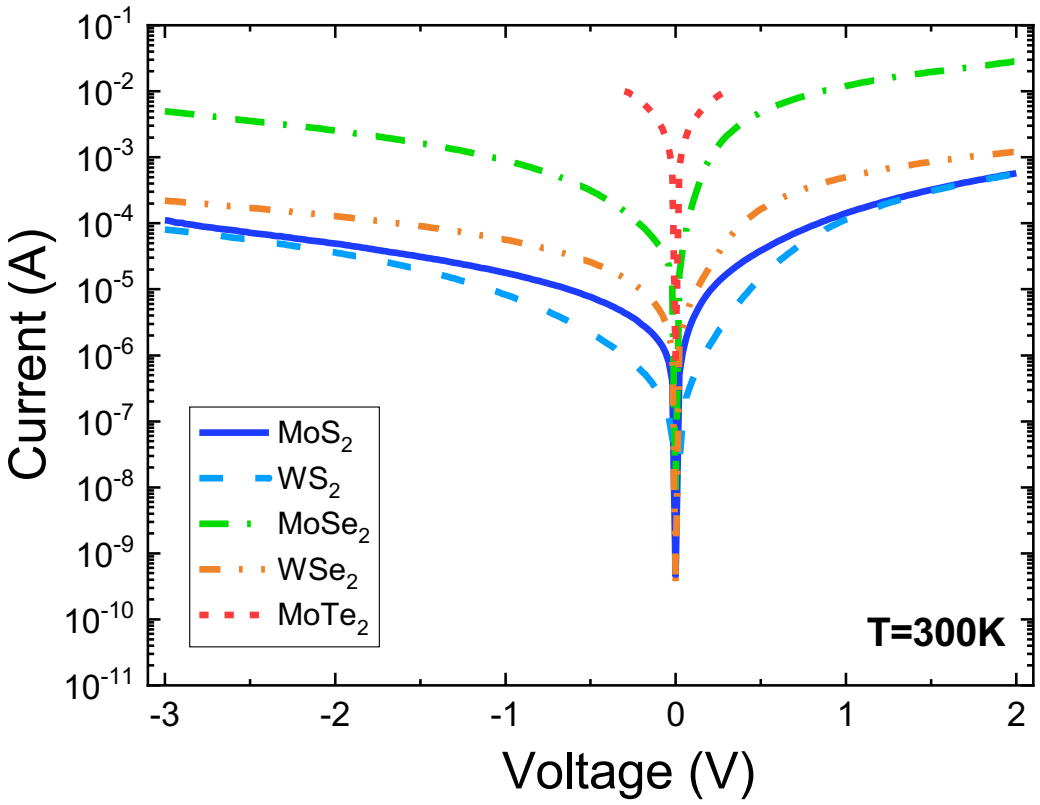

Figure 7.2 I-V characteristics for the investigated TMDs bulk crystals recorded at 300 K.

Representative examples of the I-V curves of the five TMD-based devices recorded at 300 K are shown in Fig. 7.2. The measurements were performed in the voltage ranging from −3V to +2V with the current limit of 10 mA. The results confirm the presence of Schottky-ohmic contacts with *n*-type conductivity in MoS_2, WS_2, $MoSe_2$, and Wse_2. Only $MoTe_2$ exhibited high current flow in both directions, indicating ohmic-ohmic behavior, which is due to the very high carrier concentration in the material, far above 10^{17} cm^{-3} (provided in 7.5.3). At the end, after the rejection of $MoTe_2$ (ohmic properties) and WTe_2 (semi-metallic), the remaining four TMDs showed reasonable rectifying properties, which makes them fully amenable to further studies of deep-level defects by means of a space charge technique (i.e., DLTS here). As the studied samples are *n*-type, the detected defects are deep donors.

Figures 7.3(a)-(d) show the standard DLTS temperature spectra of MoS_2, WS_2, $MoSe_2$, and WSe_2. As shown in Fig. 7.3, single positive peaks dominate the DLTS spectra of MoS_2 and WS_2. These peaks

are labelled as A1 and B1, respectively. Their activation energies are very close to each other, indicating the same origin of both traps. On the other hand, at least three overlapping peaks, labelled as C1-C3 and D1-D3, were revealed in $MoSe_2$ and WSe_2. In order to clearly determine the accurate number of peaks composing the DLTS signal, we used a standard curve fitting procedure of multiple peaks with a Gaussian function (marked with colored solid lines in Fig. 7.3).

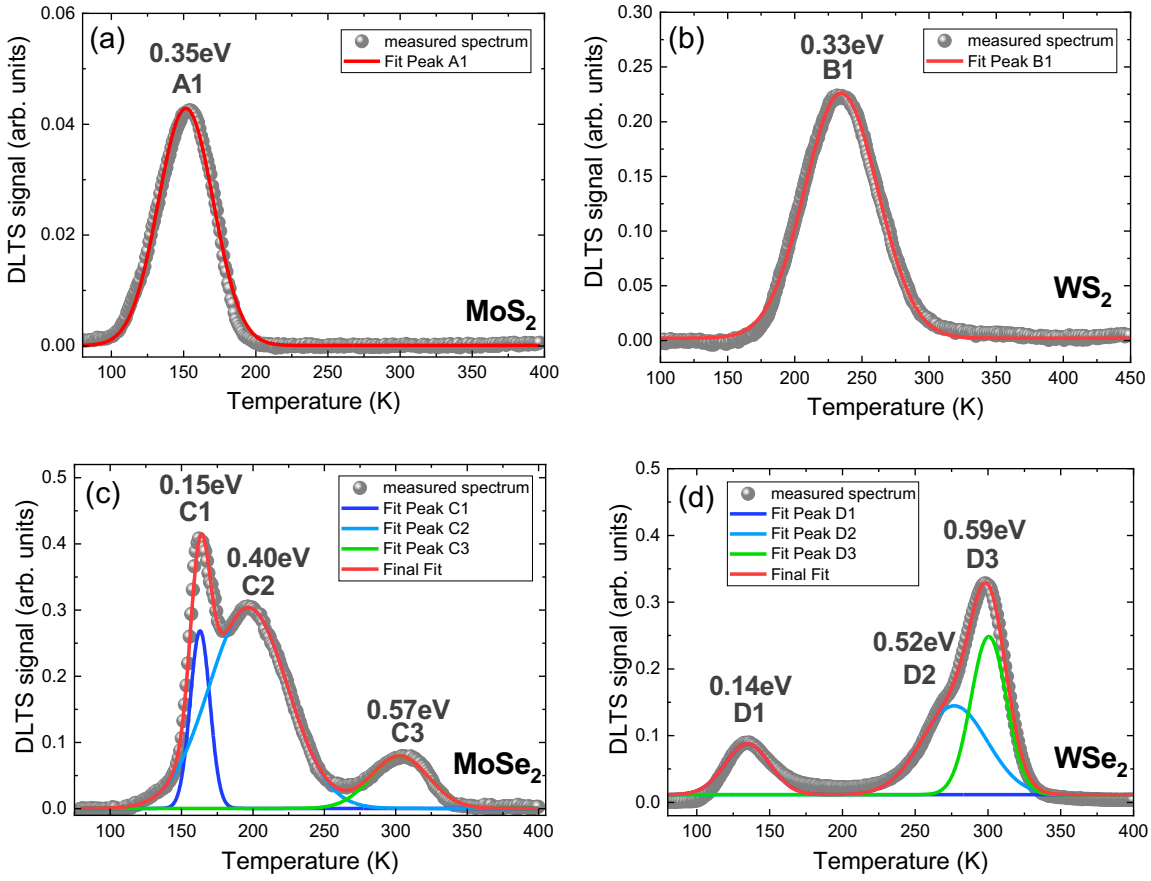

Figure 7.3 Standard DLTS spectra of (a) MoS_2, (b) WS_2, (c) $MoSe_2$, and (d) WSe_2. The solid lines represent the individual peak contribution obtained by the Gaussian fitting, and the numbers indicate the obtained energy positions of the CTLs referenced to the CBM.

There have been a number of previously reported theoretical studies on the CTLs in TMDs[85–88,182–185,197]. The CTLs of V_S (0/−1) in bulk MoS_2 referenced to vacuum obtained from the previous studies are approximately −4.75 eV and −4.77 eV[87] and −4.6 eV[88]. The same values referenced to the

CBM, as is most convenient for comparison with the DLTS results, are 0.31 eV and 0.77 eV[87] and 0.28-0.38 eV[88]. The authors of Reference[87] note that they arrive at two very different values due to the use of two different calculation methods. These two values curiously coincide with experimental studies where a deep donor level was found at about 0.27 eV below the CBM in MoS_2/graphene heterojunction transistors obtained by using the temperature-dependent I-V measurement[194], whereas the combination of STM and STS methods have revealed a donor level in bulk MoS_2 at 0.7 eV below the CBM [186]. This suggests that a certain level of ambiguity is still present in both theoretical and experimental literatures. Our result of -4.53 eV and 0.36 for V_S $(0/-1)$ (referenced to vacuum and the CBM, respectively) generally agrees with the values from Reference[88] and one of the approaches used in Reference[87], although here we paid particular attention to account for the experimental bandgaps as well, and therefore expect higher reliability of the obtained values than from the other methods. A more convincing argument for the accuracy of our calculations is presented further as follows, where we compare the computational results with our DLTS experiments and find a very good agreement.

Only a few of the previously calculated defects were confirmed experimentally[190–196]. Because of its popularity, most of the experimental evidences has focused on the native point defects in MoS_2[190,194–196] and much less has been devoted to defects in other TMDs, such as WSe_2[191] and WS_2[192,193]. Moreover, in most cases the reported CTLs of defects were obtained from indirect measurements, such as PL[190–193], I-V[194] or STS[186], with two exceptions of direct studies performed by DLTS[195,196]. Especially, PL has been extensively used[190–193], but the PL estimated CTLs are very diversified and it is difficult to unambiguously assign the detected signal to specific defect states.

Finally, DLTS and CTS techniques were successfully used for direct probing of deep-level defects in TMDs. By analyzing standard DLTS temperature spectra we found a single deep level at 0.36 eV in bulk MoS_2 crystal (~200 μm), which was attributed to V_S[195]. Another work, performed by Ci et al.[196], also revealed a single deep energy level below the CBM in the range of 0.25-0.31 eV in mechanically exfoliated multilayer (~50 nm) flakes of $Mo_{1-x}W_xS_2$ ($x = 0$, 0.4, 0.7, 1). The energy positions of the deep level measured by DLTS and CTS in different samples agree well with the previous

DFT calculated V_S levels[86–88]. The authors found also another deep-level defect at about 0.4-0.47 eV in a few of the studied samples, which exhibited DX center[196].

As explained above, most of the previous studies considered only chalcogen vacancies when establishing the origin of the defect-related properties. Moreover, most of the experimental values given in the previous studies were obtained with methods that do not directly measure the CTLs of defects and therefore there is still lack of reliable data to directly validate the computational results. Therefore, direct and accurate experimental determination of the position of CTLs, performed consistently across the entire family of TMDs, would be of great value. Here, our computational predictions of CTLs agree very well with our DLTS results, which validates our computational approach and provides understanding of the origin of the DLTS results.

Comparison of data in Table 7.2 and Fig. 7.3 reveals that our calculations predict the DLTS results very well. Specifically, in MoS_2, the DLTS signal labeled as A1 found at 0.35 eV below the CBM (Fig. 7.3(a)) clearly corresponds to the CTL of V_S (0/−1), computationally found at 0.36 eV below the CBM. Also, this result agrees well with a previous DFT study[87]. In WS_2, a single DLTS peak B1 was found with the activation energy of 0.33 eV (Fig. 7.3(b)), which again agrees well with the CTL of V_S (0/−1) found in our calculations at 0.34 eV below the CBM. For $MoSe_2$ and WSe_2, three deep levels were found experimentally. As shown in Fig. 7.3(c), the DLTS signals C1 (0.15 eV), C2 (0.40 eV), and C3 (0.57 eV) found in $MoSe_2$ likely originate from V_{Se} (0/−1), V_{Mo} (−1/−2), and Se_{Mo} (0/−1) with the levels of 0.13 eV, 0.44 eV, and 0.59 eV, respectively. Similarly, for WSe_2 the DLTS spectra revealed three peaks, labeled D1 (0.14 eV), D2 (0.52 eV), and D3 (0.59 eV) as shown in Fig. 7.3(d). These peaks correspond, respectively, to the computationally found CTLs of V_{Se} (0/−1), V_W (−1/−2), and Se_W (0/−1), positioned at 0.12 eV, 0.49 eV, and 0.65 eV below the CBM.

It is worth noting that some of the native defects are not observed in DLTS measurements but in general such defects are expected in TMD samples. The activation energies of these defects obtained in the DFT calculations should be very reliable considering the agreement between the experiments and the

calculations for those that were observed experimentally. Such defects can be observed in TMDs obtained under different growth conditions or samples bombarded with alpha particles.

Table 7.3 Comparison between the theoretically predicted and the experimentally measured CTLs of native point defects in bulk MoS_2, $MoSe_2$, WS_2, and WSe_2, with the corresponding defect natures identified by the DFT calculations. The energy values are referenced to the CBM.

eV	CTLs (DFT)	CTLs (DLTS)	Defect origin
MoS_2	0.36	0.35	V_S $(0/-1)$
	0.13	0.15	V_{Se} $(0/-1)$
$MoSe_2$	0.44	0.40	V_{Mo} $(-1/-2)$
	0.59	0.57	Se_{Mo} $(0/-1)$
WS_2	0.34	0.33	V_S $(0/-1)$
	0.12	0.14	V_{Se} $(0/-1)$
WSe_2	0.49	0.52	V_W $(-1/-2)$
	0.65	0.59	Se_W $(0/-1)$

The summary of our experimental and computational results is shown in Table 7.3. In our DLTS experiments, we measured the CTLs of defects in MX_2 ($M = $ Mo or W; $X = $ S or Se), which agree well with our DFT calculations. The good agreement between our computational prediction and the results obtained from DLTS, a direct and accurate experimental method for determining CTLs, suggests high reliability of our computational approach.

7.3.2 CTLs in 2D TMDs

We now use the same computational method validated on the bulk TMDs to predict defect properties in 2D TMDs, which cannot be measured by DLTS. In Fig. 7.4, we plotted the formation energies of vacancies (metal and chalcogen) in the six 2D MX_2 (solid) and bulk MX_2 (dashed) calculated using the DLTS-validated method at the chalcogen-rich condition. In Table 7.4, we tabulated the CTLs of vacancies in the six 2D MX_2 identified from Fig. 7.4. For the metal and chalcogen vacancies, the only type of transition found inside the bandgaps is $0/-1$ in MoS_2, $MoSe_2$, WS_2, and WSe_2, whereas in $MoTe_2$ and WTe_2 the only transition found inside the bandgaps is $+1/0$. For MoS_2, our results are in good

agreement with earlier computational studies. Specifically, Tan et al.[88] reported the CTLs of V_S in bulk and 2D MoS_2, which are approximately −4.6 eV and −4.5 eV referenced to vacuum, respectively (read off the plot in the study[88]). The aforementioned values agree well with our results, which are −4.53 eV and −4.52 eV for V_S in bulk and 2D MoS_2, respectively.

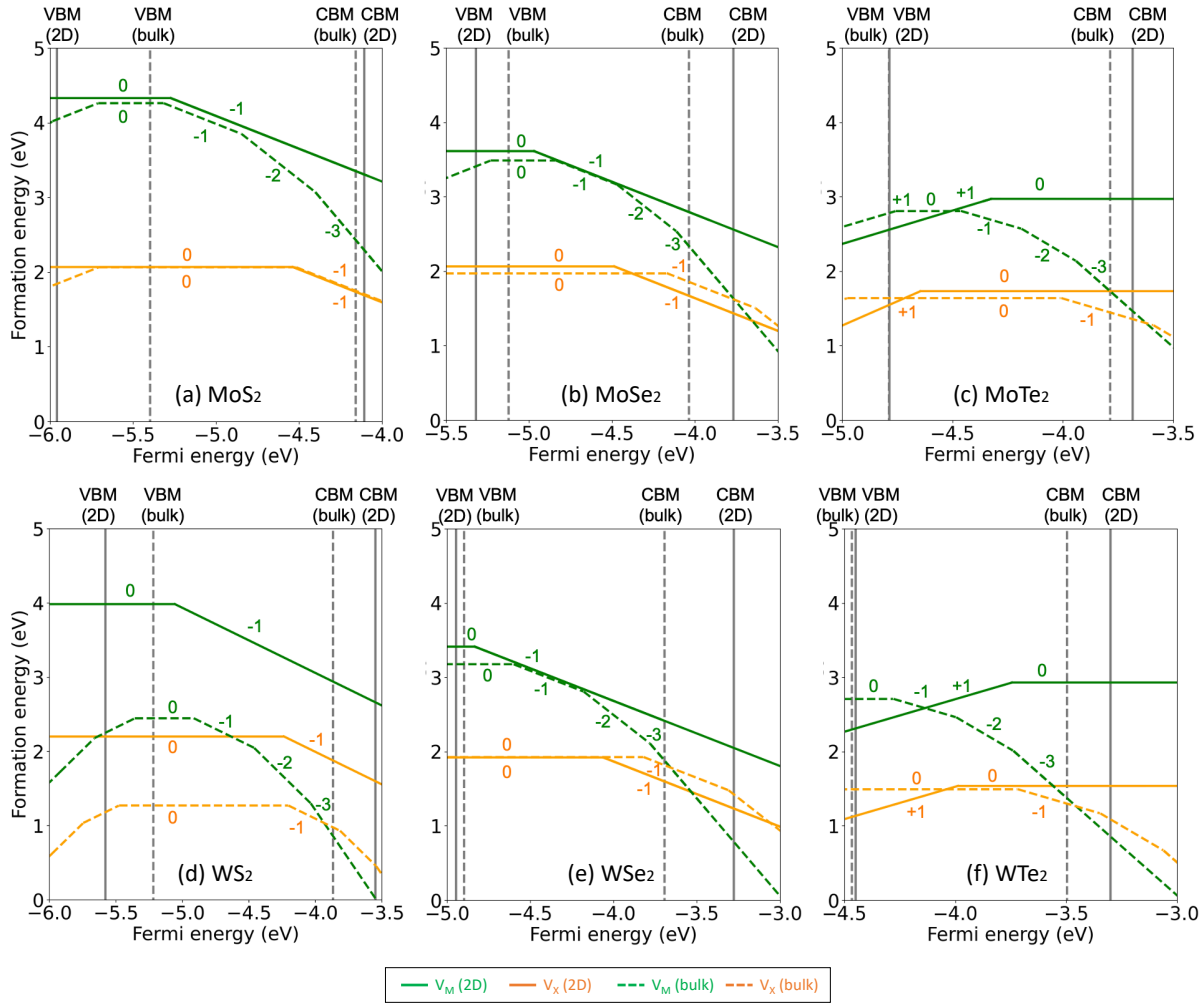

Figure 7.4 Defect formation energies and CTLs of metal and chalcogen vacancies calculated at the chalcogen-rich condition as a function of Fermi energy in 2D (solid) and bulk (dashed) (a) MoS_2, (b) $MoSe_2$, (c) $MoTe_2$, (d) WS_2, (e) WSe_2, and (f) WTe_2.

Table 7.4 Identified CTLs of defects from Fig. 7.4 (M = Mo, W; X = S, Se, Te). The levels are referenced to the CBM.

Defect	MoS_2	$MoSe_2$	$MoTe_2$	WS_2	WSe_2	WTe_2
V_M	1.16 (0/−1)	1.20 (0/−1)	0.66 (+1/0)	1.51 (0/−1)	1.56 (0/−1)	0.44 (+1/0)
V_X	0.43 (0/−1)	0.64 (0/−1)	0.96 (+1/0)	0.69 (0/−1)	0.79 (0/−1)	0.66 (+1/0)

It is very instructive to compare the calculated CTLs of defects in the bulk and 2D TMDs, given the effects of the reduction in dimensionality on the bandgaps (i.e., indirect bandgaps of bulk transitioned to direct bandgaps of 2D in the TMDs). First of all, we found that, unlike the bulk systems where the metal vacancies have many CTLs inside their bandgaps, in the 2D systems the metal vacancies create only a single CTL inside the bandgap. Secondly, previous computational studies by Komsa et al.[87] and Tan et al.[88] reported that the CTL of V_S (0/−1) is similar in bulk and 2D MoS_2, but the study was carried out only for MoS_2. Our calculations agree with their results (the CTL of V_S (0/−1) in both bulk and 2D MoS_2 is around −4.5 eV, referenced to vacuum), and we also found the same trend from V_S in WS_2 (−4.20 eV for the bulk and −4.24 eV for the 2D). However, we found that this conclusion is not general as the agreement between bulk and 2D CTLs is not found in the other TMDs (see Fig. 7.4).

Data shown in Fig. 7.4 and Table 7.4 clearly demonstrates that the reduction in the dimensionality of TMDs from bulk to 2D has a significant impact on both the formation energies and the CTLs of native defects in relation to vacuum as well as in relation to the CBM. The significant differences in formation energies and CTLs of the same type of defects in bulk and 2D TMDs may explain why epitaxially grown samples (i.e., grown as 2D material) and samples exfoliated from bulk crystals (i.e., 2D material obtained from a sample grown as bulk) exhibit different optical properties, with the former usually exhibiting worse optical and electrical properties[193,220,221].

7.4 Conclusions

In this chapter, we reported the CTLs of native point defects in TMDs, MX_2 (M = Mo or W; X = S, Se, or Te) using state-of-the-art computational methods, including DFT calculations with the optimized

functional, electrostatic correction, and band alignment. We also measured the CTLs directly by means of DLTS experiments, which agreed well with the computational predictions. We found that the chalcogen vacancy, the most stable defect in each of the six bulk TMDs, creates the 0/−1 charge transition inside the bandgap and that the selection of transition metal has only little effect on the position of the 0/−1 charge transition. The very good agreement of experimental and computational results validated the computational approach and allowed the identification of the origin of the experientially found defect levels. The same computational approach was then used to calculate the CTLs of defects in 2D TMDs. Our computational results shed light on the defect properties in 2D TMDs, which is experimentally not feasible. In addition, by comparing the bulk and 2D TMDs data, we found the significant differences in the trends of the CTLs of defects in the bulk and 2D TMDs. This joint computational and experimental work provides the validated and consistent data regarding the CTLs of defects in bulk and 2D TMDs and their chemical trends, and it also suggests a relatively inexpensive computational strategy for accurately determining the CTLs of defects in TMDs. This work may aid in properly designing and fabricating TMD-based applications.

7.5 Supplementary Information

7.5.1 Optimized lattice parameters calculated using different functionals

Table 7.S1 Lattice parameters (Å) calculated using the different functionals and the experimental lattice parameters from references [104,210–215]. The average error of the calculated lattice constants compared with the experiments is in parenthesis. *z* indicates the vertical distance between M and X within a MX_2 layer.

		MoS_2	$MoSe_2$	$MoTe_2$	WS_2	WSe_2	WTe_2
Experiments	*a*	3.15	3.29	3.52	3.15	3.28	3.60
	c	12.30	12.93	13.96	12.32	12.96	14.18
	z	1.57	1.67	1.80	1.57	1.67	
optB88-vdW (MAE: 1.80 %)	*a*	3.19	3.33	3.57	3.19	3.33	3.61
	c	12.44	13.17	14.25	12.52	13.23	14.60
	z	1.57	1.68	1.81	1.58	1.53	1.82
PBE+D3 (MAE: 1.01 %)	*a*	3.14	3.27	3.49	3.15	3.28	3.50
	c	12.08	12.72	13.66	12.11	12.78	13.76
	z	1.57	1.68	1.82	1.58	1.69	1.83
PBE+rVV10L (MAE: 1.75 %)	*a*	3.12	3.24	3.46	3.12	3.25	3.46
	c	11.87	12.58	13.57	11.97	12.64	13.64
	z	1.57	1.69	1.83	1.59	1.70	1.84
PBEsol+rVV10s (MAE: 3.02 %)	*a*	3.08	3.20	3.40	3.08	3.20	3.40
	c	11.56	12.24	13.28	11.62	12.34	13.33
	z	1.57	1.68	1.83	1.58	1.70	1.84
rev-vdW-DF2 (MAE: 0.49 %)	*a*	3.16	3.30	3.54	3.17	3.30	3.54
	c	12.35	13.04	14.05	12.42	13.06	14.11
	z	1.57	1.67	1.81	1.57	1.68	1.82
SCAN+rVV10 (MAE: 0.64 %)	*a*	3.16	3.29	3.50	3.16	3.28	3.49
	c	12.22	13.02	14.06	12.20	13.05	14.10
	z	1.55	1.68	1.81	1.58	1.69	1.82
vdW-DF-cx (MAE: 2.34 %)	*a*	3.22	3.36	3.61	3.21	3.36	3.61
	c	12.85	13.45	14.58	12.77	13.50	14.64
	z	1.57	1.68	1.81	1.58	1.69	1.82
HSE (MAE: 3.52 %)	*a*	3.15	3.28	3.51	3.15	3.28	3.51
	c	13.44	14.03	15.14	13.83	14.39	14.89
	z	1.55	1.65	1.79	1.56	1.66	1.80

7.5.2 Adjustment of the CTLs using the band alignment methods

Table 7.S2 CTLs (in eV, below the CBM) with respect to the different band alignment methods for the experimentally found levels, along with the DLTS result for comparison.

	MoS_2	WS_2		$MoSe_2$			WSe_2	
Band alignment	V_S (0/−1)	V_S (0/−1)	V_{Se} (0/−1)	V_{Mo} (−1/−2)	Se_{Mo} (0/−1)	V_{Se} (0/−1)	V_W (−1/−2)	Se_W (0/−1)
Not aligned	0.45	0.45	0.21	0.48	0.62	0.25	0.57	0.71
Conventional	0.30	0.27	0.10	0.37	0.51	0.09	0.41	0.55
Modified	0.36	0.34	0.13	0.44	0.59	0.12	0.49	0.65
DLTS	0.35	0.33	0.15	0.40	0.57	0.14	0.52	0.59

7.5.3 Temperature-dependent I-V characteristics

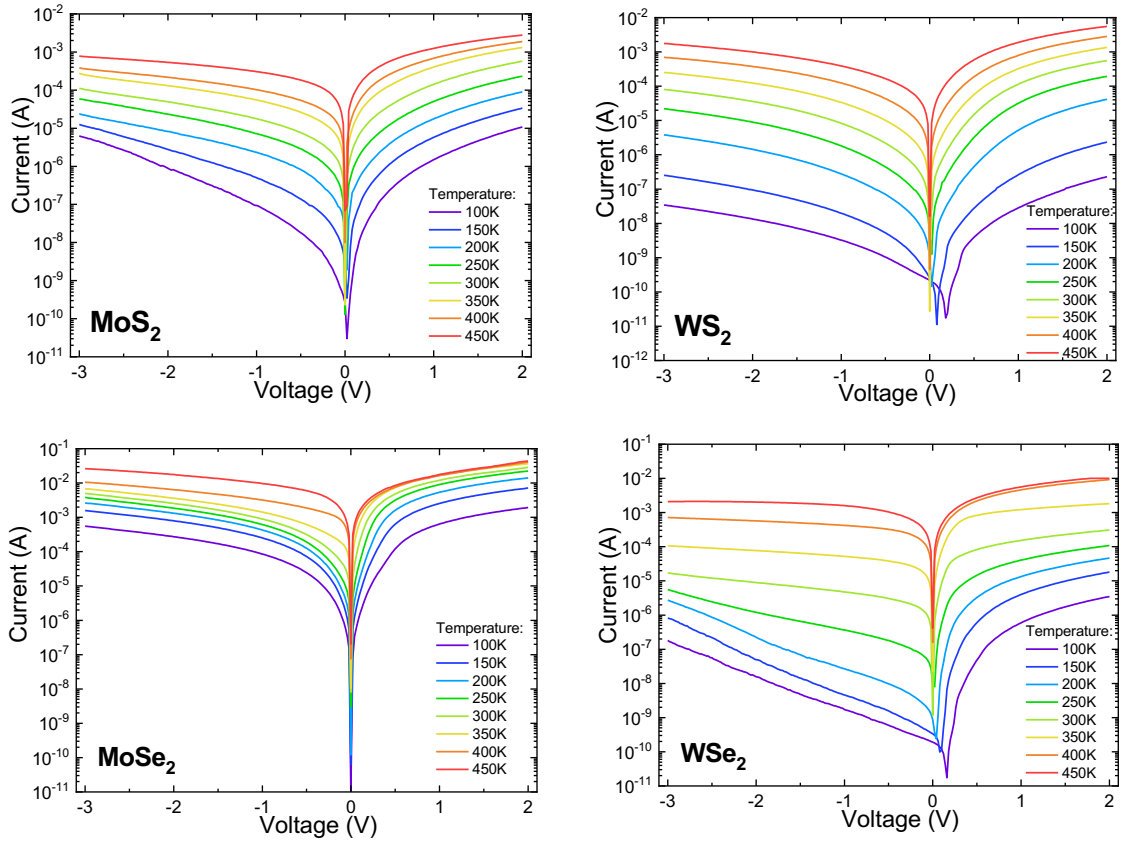

Figure 7.S1 I-V characteristics of MoS_2, WS_2, $MoSe_2$, and WSe_2 recorded at the temperature ranging from 100K to 450K.

Table 7.S3 Main electrical parameters obtained from the I-V-T characteristics at selected temperatures.

	Temperature (K)	MoS_2	$MoSe_2$	WS_2	WSe_2
Ideality factor n (a.u.)	*100*	6.55	4.25	2.23	3.46
	200	3.90	2.59	3.45	2.94
	300	2.03	2.15	4.07	2.79
	400	1.56	1.96	4.24	2.14
Series resistance R_s (Ω)	*100*	98.1k	642	569.5k	310.3k
	200	13.1k	106.5	30.1k	27.8k
	300	2.4k	57.5	2.1k	5.5k
	400	822.2	40.7	466.7	173.9
Schottky barrier height *SBH* (eV)	*100*	0.26	0.19	0.30	0.26
	200	0.43	0.38	0.49	0.45
	300	0.61	0.53	0.66	0.60
	400	0.77	0.65	0.80	0.69

CHAPTER 8

SUMMARY AND FUTURE WORKS

8.1 Transition metal borides

I discussed the defect behavior in transition metal borides (TMBs), focusing on the key energies that control the defect recovery processes, based on the results of density functional theory (DFT) calculations. In Chapter 3, Fe_2AlB_2 was experimentally found to be more tolerant to radiation-induced amorphization than MoAlB. I rationalized the experimental results based on the defect stability and its impact on the defect recovery processes. In MoAlB, which has two-Al-atomic layers, Mo interstitials are not stable in the Al layers and immediately transform to antisites that are not mobile and do not easily react with other defects, which are detrimental for the defect recovery processes. In Fe_2AlB_2, which has one-Al-atomic layers, Fe interstitials are stable and mobile in the Al layers and easily recombine with Fe vacancies, contributing to the efficient defect recovery processes. In Chapter 4, I introduced the Cr-based binary TMBs (CrB, Cr_3B_4, Cr_2B_3) and the ternary MAB phases (Cr_2AlB_2, Cr_3AlB_4, Cr_4AlB_6), wherein the type of B networks and the presence/absence of the Al layers play a key role in the defect recovery processes. I found that increasing the number of B rings in the B networks leads to lower formation energies and higher concentrations of Frenkel pairs (FPs). The result is attributed to the weakening of Cr-B bonds with increasing the number of B rings, leading to the reduction in the formation energies of Cr and B vacancies. I also discussed the tolerance to radiation-induced amorphization of the Cr-based TMBs in Chapter 5. In our experiments, the order of the tolerance to radiation-induced amorphization was, from high to low, CrB, Cr_3AlB_4, Cr_3B_4, Cr_4AlB_6, and Cr_2AlB_2 at 150 °C and 0.5 dpa, and Cr_3AlB_4, CrB, Cr_3B_4, Cr_4AlB_6, and Cr_2AlB_2 at 300 °C and 1.0 dpa. I explained the experimental results based on the structure-dependent defect recovery processes. I found that in MAB phases, B FP recombination is largely dependent on the type of B networks, with the most efficient recombination found in the one-B-ring

structure. I also found that the Al layers in MAB phases prevent B FPs from recombining, whereas the effect of the Al layers on the Cr FP recombination differs by the type of the B networks. In Chapter 6, I generalized the findings from the studies on MoAlB, Fe_2AlB_2, Cr-B and Cr-Al-B systems and developed the design rules by testing the different types of TMBs with different metal elements. In $M_1A_1B_1$, which has two-Al-atomic layers, M interstitials are unstable and form antisites that are detrimental for the defect recovery processes, whereas in $M_2A_1B_2$, which has one-Al-atomic layers, M interstitials are stable in the Al layers. The absence of Al layers in the binary TMBs (i.e., M_1B_1, M_3B_4) helps the recombination of B FPs by lowering the recombination energy barriers. As for the effects on the recombination of M FPs, the absence of Al layers helps lower the migration energies of M interstitials when TMBs have one-B-chain layers (i.e., M_1B_1 and $M_2A_1B_2$), whereas the effects of the Al layers depend on the type of transition metals when TMBs have B-ring layers. I also found the correlation that the weaker the M-B bonds, the lower the B FP recombination barriers in $M_2A_1B_2$ and $M_3A_1B_4$. My studies suggest that MAB phases will be promising in applications that involve radiation, while providing the design rules for TMBs with efficient defect recovery processes.

Based on the set of the studies on the TMBs, I propose future studies on the design of TMBs for extreme environment applications (e.g., radiation, high temperature, and/or oxidation). The general trends found in the TMBs can be applied to the design of high entropy borides (HEBs). HEBs are a type of layered ultra-high temperature ceramics and consist of several mixing transition metal elements bonded to the B networks. Among the types of HEBs discovered[222,223], hexagonal layered HEBs with the general formula of MB_2 (M indicates mixing transition metal elements here; B = B) are of particular interest in that their hardness and oxidation resistance are found to be generally higher or better than the average performance of the individual metal diborides[223]. The key design strategy I propose here is the selection of different transition metal elements, each of which possesses its own outstanding properties and collectively contribute to the overall properties of the designed HEB. For instance, considering desirable properties of materials for nuclear reactor applications, HEBs may be designed with a set of transition metal elements that collectively exhibit stability at high temperature, efficient defect recovery processes,

and good oxidation resistance. The stability at high temperature would be likely achieved by including transition metal elements expected to form strong M-B bonds (e.g., Ti, Zr, Hf). Including transition metal elements expected to form weak M-B bonds (e.g., Ni) would likely contribute to efficient defect recovery processes of the HEBs. In addition, adding elements known for outstanding oxidation resistance (e.g., Ta) would be beneficial for the oxidation resistance of the designed HEBs.

8.2 Transition metal dichalcogenides

I discussed the defect properties in transition metal dichalcogenides (TMDs), focusing on the formation energies and the charge-state transition levels (CTLs) of native point defects in MX_2 (M = Mo, W; X = S, Se, or Te). I applied a joint experimental and computational strategy to accurately determine the CTLs in two-dimensional (2D) MX_2 using deep level transient spectroscopy (DLTS) and DFT calculations with the optimized functional, electrostatic correction, and band alignment. I calculated the CTLs and the formation energies of defects in bulk MX_2 and compared them with the results of DLTS experiments. The very good agreement between the experimental and computational results validated the computational approach and allowed the identification of the nature of the experimentally found CTLs. The validated computational approach was then used to determine the CTLs in 2D MX_2, for which DTLS is very challenging. By comparing the bulk and 2D MX_2 data, I found the considerable effects of the reduction in the dimensionality (i.e., bulk to 2D) on the CTLs in MX_2. My study provides the validated and consistent data regarding the CTLs of native point defects in bulk and 2D MX_2 and their chemical trends, and it also suggests a reliable computational strategy for accurately determining the CTLs in 2D MX_2. This work may aid in properly designing and fabricating TMD-based applications.

BIBLIOGRAPHY

1. Lévy, F. *Intercalated layered materials*. (Springer, Netherlands, 1979).
2. Matkovich, V. I. *Boron and refractory borides*. (Springer, Berlin, 1977).
3. Lundstrom, T. Structure, defects and properties of some refractory borides. *Pure and Applied Chemistry* **57**, 1383–1390 (1985).
4. Dickinson, R. G. & Pauling, L. The crystal structure of molybdenite. *Journal of the American Chemical Society* **45**, 1466–1471 (1923).
5. Frindt, R. F. & Yoffe, A. D. Physical properties of layer structures: optical properties and photoconductivity of thin crystals of molybdenum disulphide. *Proceedings of the Royal Society of London. Series A. Mathematical and Physical Sciences* **273**, 69–83 (1963).
6. Joensen, P., Frindt, R. F. & Morrison, S. R. Single-layer MoS_2. *Materials Research Bulletin* **21**, 457–461 (1986).
7. Wuchina, E., Opila, E., Opeka, M., Fahrenholtz, B. & Talmy, I. UHTCs: ultra-high temperature ceramic materials for extreme environment applications. *The Electrochemical Society Interface* **16**, 30–36 (2007).
8. Munro, R. G. Material properties of a sintered α-SiC. *Journal of Physical and Chemical Reference Data* **26**, 1195–1203 (1997).
9. Sairam, K. *et al.* Reaction spark plasma sintering of niobium diboride. *International Journal of Refractory Metals and Hard Materials* **43**, 259–262 (2014).
10. Castle, E., Csanádi, T., Grasso, S., Dusza, J. & Reece, M. Processing and properties of high-entropy ultra-high temperature carbides. *Scientific Reports* **8**, 8609 (2018).
11. Tului, M. *et al.* Effects of heat treatments on oxidation resistance and mechanical properties of ultra high temperature ceramic coatings. *Surface and Coatings Technology* **202**, 4394–4398 (2008).
12. Hu, Y. *et al.* Two-dimensional transition metal dichalcogenide nanomaterials for biosensing applications. *Materials Chemistry Frontiers* **1**, 24–36 (2017).
13. Okada, S. *et al.* Single-crystal growth and properties of CrB, Cr_3B_4, Cr_2B_3 and CrB_2 from high-temperature aluminum solutions. *Journal of Crystal Growth* **166**, 429–435 (1996).
14. Zhang, X., Luo, X., Han, J., Li, J. & Han, W. Electronic structure, elasticity and hardness of diborides of zirconium and hafnium: first principles calculations. *Computational Materials Science* **44**, 411–421 (2008).
15. Lawson, J. W., Daw, M. S. & Bauschlicher, C. W. Lattice thermal conductivity of ultra-high temperature ceramics ZrB_2 and HfB_2 from atomistic simulations. *Journal of Applied Physics* **110**, 083507 (2011).
16. Zhang, G.-J., Guo, W.-M., Ni, D.-W. & Kan, Y.-M. Ultra-high temperature ceramics (UHTCs) based on ZrB_2 and HfB_2 systems: powder synthesis, densification and mechanical properties. *Journal of Physics: Conference Series* **176**, 012041 (2009).
17. Murthy, T. S. R. Ch. *et al.* Effect of CrB_2 addition on densification, properties and oxidation resistance of TiB_2. *International Journal of Refractory Metals and Hard Materials* **27**, 976–984 (2009).
18. Guo, F. *et al.* A class of metal diboride electrocatalysts synthesized by a molten salt-assisted reaction for the hydrogen evolution reaction. *Chemical Communications* **55**, 8627–8630 (2019).
19. Li, H. *et al.* Earth-abundant iron diboride (FeB_2) nanoparticles as highly active bifunctional electrocatalysts for overall water splitting. *Advanced Energy Materials* **7**, 1700513 (2017).
20. Okada, S., Kudou, K. & Lundström, T. Preparations and some properties of W_2B, δ-WB and WB_2 crystals from high-temperature metal solutions. *Japanese Journal of Applied Physics* **34**, 226–231 (1995).
21. Peshev, P. & Bliznakov, G. On the borothermic preparation of titanium, zirconium and hafnium diborides. *Journal of the Less Common Metals* **14**, 23–32 (1968).

22. Xinghong, Z. Self-propagating high temperature combustion synthesis of TiC/TiB_2 ceramic–matrix composites. *Composites Science and Technology* **62**, 2037–2041 (2002).
23. Wang, Y., Ma, B., Li, L. & An, L. Oxidation behavior of ZrB_2-SiC-TaC ceramics. *Journal of the American Ceramic Society* **95**, 374–378 (2012).
24. Monteverde, F. & Bellosi, A. Efficacy of HfN as sintering aid in the manufacture of ultra-high temperature metal diborides-matrix ceramics. *Journal of Materials Research* **19**, 3576–3585 (2004).
25. Zhao, H., Wang, J., Zhu, Z., Pan, W. & Wang, J. In situ synthesis mechanism of ZrB_2–ZrN composite. *Materials Science and Engineering: A* **452–453**, 130–134 (2007).
26. Curtis, c. e. & Johnson, J. R. Properties of thorium oxide ceramics. *Journal of the American Ceramic Society* **40**, 63–68 (1957).
27. Ade, M. & Hillebrecht, H. Ternary borides Cr_2AlB_2, Cr_3AlB_4, and Cr_4AlB_6: the first members of the series $(CrB_2)_nCrAl$ with n = 1, 2, 3 and a unifying concept for ternary borides as MAB-phases. *Inorganic Chemistry* **54**, 6122–6135 (2015).
28. Barsoum, M. W. $M_{n+1}AX_n$ phases: a new class of solids; thermodynamically stable nanolaminates. *Progress in Solid State Chemistry* **28**, 201–281 (2000).
29. Magnuson, M. & Mattesini, M. Chemical bonding and electronic-structure in MAX phases as viewed by X-ray spectroscopy and density functional theory. *Thin Solid Films* **621**, 108–130 (2017).
30. Bingchu, M., Ming, Y., Jiaoqun, Z. & Weibing, Z. Preparation of TiAl/Ti_2AlC composites with Ti/Al/C powders by in-situ hot pressing. *Journal of Wuhan University of Technology-Material Science Edition* **21**, 14–16 (2006).
31. Hanaor, D. A. H. *et al.* Compressive performance and crack propagation in Al alloy/Ti_2AlC composites. *Materials Science and Engineering: A* **672**, 247–256 (2016).
32. Barsoum, M. W. & El-Raghy, T. Synthesis and characterization of a remarkable ceramic: Ti_3SiC_2. *Journal of the American Ceramic Society* **79**, 1953–1956 (1996).
33. Goto, T. & Hirai, T. Chemically vapor deposited Ti_3SiC_2. *Materials Research Bulletin* **22**, 1195–1201 (1987).
34. Whittle, K. R. *et al.* Radiation tolerance of $M_{n+1}AX_n$ phases, Ti_3AlC_2 and Ti_3SiC_2. *Acta Materialia* **58**, 4362–4368 (2010).
35. Xiao, J., Yang, T., Wang, C., Xue, J. & Wang, Y. Investigations on radiation tolerance of $M_{n+1}AX_n$ phases: study of Ti_3SiC_2, Ti_3AlC_2, Cr_2Al_C, Cr_2GeC, Ti_2AlC, and Ti_2AlN. *Journal of the American Ceramic Society* **98**, 1323–1331 (2015).
36. Middleburgh, S. C., Lumpkin, G. R. & Riley, D. Accommodation, accumulation, and migration of defects in Ti_3SiC_2 and Ti_3AlC_2 MAX phases. *Journal of the American Ceramic Society* **96**, 3196–3201 (2013).
37. Mann, D. K. *et al.* Electrocatalytic water oxidation over $AlFe_2B_2$. *Chemical Science* **10**, 2796–2804 (2019).
38. Alameda, L. T., Holder, C. F., Fenton, J. L. & Schaak, R. E. Partial etching of Al from MoAlB single crystals to expose catalytically active basal planes for the hydrogen evolution reaction. *Chemistry of Materials* **29**, 8953–8957 (2017).
39. Shi, O. *et al.* Synthesis and oxidation resistance of MoAlB single crystals. *Ceramics International* **45**, 2446–2450 (2019).
40. Kota, S. *et al.* Isothermal and cyclic oxidation of MoAlB in air from 1100 °C to 1400 °C. *Journal of The Electrochemical Society* **164**, C930–C938 (2017).
41. Zhang, W. *et al.* Synthesis and properties of MoAlB composites reinforced with SiC particles. *Journal of Advanced Ceramics* **11**, 495–503 (2022).
42. Liu, C., Hou, Z., Jia, Q., Liu, X. & Zhang, S. Low temperature synthesis of phase pure MoAlB powder in molten NaCl. *Materials* **13**, 785 (2020).

43. Tan, X., Chai, P., Thompson, C. M. & Shatruk, M. Magnetocaloric effect in $AlFe_2B_2$: toward magnetic refrigerants from earth-abundant elements. *Journal of the American Chemical Society* **135**, 9553–9557 (2013).
44. Du, Q. *et al.* Magnetic properties of $AlFe_2B_2$ and $CeMn_2Si_2$ synthesized by melt spinning of stoichiometric compositions. *Japanese Journal of Applied Physics* **54**, 053003 (2015).
45. Barua, R. *et al.* Anisotropic magnetocaloric response in $AlFe_2B_2$. *Journal of Alloys and Compounds* **745**, 505–512 (2018).
46. Cedervall, J. *et al.* Magnetic structure of the magnetocaloric compound $AlFe_2B_2$. *Journal of Alloys and Compounds* **664**, 784–791 (2016).
47. Hirt, S., Yuan, F., Mozharivskyj, Y. & Hillebrecht, H. $AlFe_{2-x}Co_xB_2$ (x = 0-0.30): T_C tuning through Co substitution for a promising magnetocaloric material realized by spark plasma sintering. *Inorganic Chemistry* **55**, 9677–9684 (2016).
48. Xiang, H., Feng, Z., Li, Z. & Zhou, Y. Theoretical investigations on mechanical and dynamical properties of MAlB (M = Mo, W) nanolaminated borides at ground-states and elevated temperatures. *Journal of Alloys and Compounds* **738**, 461–472 (2018).
49. Li, X., Chagas da Silva, M. & Salahub, D. R. First-principles calculations of the structural, mechanical, electronic and bonding properties of $(CrB_2)_nCrAl$ with n = 1, 2, 3. *Journal of Alloys and Compounds* **698**, 291–303 (2017).
50. Dai, F.-Z., Feng, Z. & Zhou, Y. Easily tiltable B-Al-B linear chain: the origin of unusual mechanical properties of nanolaminated MAB phases $(CrB_2)_nCrAl$. *Journal of Alloys and Compounds* **723**, 462–466 (2017).
51. Rastogi, A., Rajpoot, P. & Verma, U. P. First principle study of UHTC ternary diboride, Cr_2AlB_2. *AIP conference proceedings* **1942**, 090005 (2018).
52. Li, X.-H., Xing, C.-H., Cui, H.-L. & Zhang, R.-Z. Elastic and acoustical properties of Cr_3AlB_4 under pressure. *Journal of Physics and Chemistry of Solids* **126**, 65–71 (2019).
53. Wei, J., Zhang, L. & Liu, Y. First-principles calculations study the mechanical and thermal properties of Cr–Al–B ternary borides. *Solid State Communications* **326**, 114182 (2021).
54. Zhou, Y., Xiang, H., Dai, F. Z. & Feng, Z. Electrical conductive and damage-tolerant nanolaminated MAB phases Cr_2AlB_2, Cr_3AlB_4 and Cr_4AlB_6. *Materials Research Letters* **5**, 440–448 (2017).
55. Liu, Y. Z. *et al.* Anisotropic elastic, thermal properties and electronic structures of M_2AlB_2 (M = Fe, Cr, and Mn) layer structure ceramics. *Ceramics International* **47**, 1421–1428 (2021).
56. Li, X. H., Cui, H. L. & Zhang, R. Z. Electronic, optical and thermal properties of Cr_3AlB_4 by first-principles calculations. *Vacuum* **145**, 234–240 (2017).
57. Li, X.-H., Cui, H.-L. & Zhang, R.-Z. Structural, optical, and thermal properties of MAX-phase Cr_2AlB_2. *Frontiers of Physics* **13**, 136501 (2018).
58. Rastogi, A., Rajpoot, P. & Verma, U. P. Study of structural, electronic, optical and thermal properties of refractory material (CrAlB). *Materials Chemistry and Physics* **211**, 242–248 (2018).
59. Verger, L., Kota, S., Roussel, H., Ouisse, T. & Barsoum, M. W. Anisotropic thermal expansions of select layered ternary transition metal borides: MoAlB, Cr_2AlB_2, Mn_2AlB_2, and Fe_2AlB_2. *Journal of Applied Physics* **124**, 20 (2018).
60. Kota, S. *et al.* Elastic properties, thermal stability, and thermodynamic parameters of MoAlB. *Physical Review B* **95**, 1–11 (2017).
61. Kota, S. *et al.* Synthesis and characterization of the atomic laminate Mn_2AlB_2. *Journal of the European Ceramic Society* **38**, 5333–5340 (2018).
62. Khazaei, M. *et al.* Novel MAB phases and insights into their exfoliation into 2D MB. *Nanoscale* **11**, 11305–11314 (2019).
63. Wang, Y. *et al.* Molten salt synthesis of orthorhombic CrB and Cr_2AlB_2 ceramics. *Ceramics International* **47**, 31772–31779 (2021).
64. Hanner, L. A., Kota, S. & Barsoum, M. W. Formation mechanisms of Cr_2AlB_2, Cr_3AlB_4, and Fe_2AlB_2 MAB phases. *Materials Research Letters* **9**, 323–328 (2021).

65. Wang, Y. *et al.* Ternary-layered Cr_2AlB_2 synthesized from Cr, Al, and B powders by a molten salt-assisted method. *Powder Technology* **387**, 354–362 (2021).
66. Zhang, H., Dai, F., Xiang, H., Zhang, Z. & Zhou, Y. Crystal structure of Cr_4AlB_4: a new MAB phase compound discovered in Cr-Al-B system. *Journal of Materials Science & Technology* **35**, 530–534 (2019).
67. Bai, Y. *et al.* Phase stability and weak metallic bonding within ternary-layered borides CrAlB, Cr_2AlB_2, Cr_3Al_4, and Cr_4AlB_6. *Journal of the American Ceramic Society* **102**, 3715–3727 (2019).
68. Dai, F.-Z., Xiang, H., Sun, Y. & Zhou, Y. $M_2M'AlB_4$ (M = Mn, Fe, Co, M' = Cr, Mo, W): theoretical predicted ordered MAB phases with Cr_3AlB_4 crystal structure. *Journal of Materials Science & Technology* **35**, 1432–1438 (2019).
69. Natu, V., Kota, S. S. & Barsoum, M. W. X-ray photoelectron spectroscopy of the MAB phases, MoAlB, M_2AlB_2 (M = Cr, Fe), Cr_3AlB_4 and their binary monoborides. *Journal of the European Ceramic Society* **40**, 305–314 (2020).
70. Lu, J., Kota, S., Barsoum, M. W. & Hultman, L. Atomic structure and lattice defects in nanolaminated ternary transition metal borides. *Materials Research Letters* **5**, 235–241 (2017).
71. Geim, A. K. & Novoselov, K. S. The rise of graphene. *Nature Materials* **6**, 183–191 (2007).
72. Kawaguchi, M., Kuroda, S. & Muramatsu, Y. Electronic structure and intercalation chemistry of graphite-like layered material with a composition of BC_6N. *Journal of Physics and Chemistry of Solids* **69**, 1171–1178 (2008).
73. Naguib, M., Mochalin, V. N., Barsoum, M. W. & Gogotsi, Y. 25th anniversary article: MXenes: a new family of two-dimensional materials. *Advanced Materials* **26**, 992–1005 (2014).
74. Jiang, Z., Wang, P., Jiang, X. & Zhao, J. MBene (MnB): a new type of 2D metallic ferromagnet with high Curie temperature. *Nanoscale Horizons* **3**, 335–341 (2018).
75. Jakubczak, M., Szuplewska, A., Rozmysłowska-Wojciechowska, A., Rosenkranz, A. & Jastrzębska, A. M. Novel 2D MBenes - synthesis, structure, and biotechnological potential. *Advanced Functional Materials* **31**, 2103048 (2021).
76. Splendiani, A. *et al.* Emerging photoluminescence in monolayer MoS_2. *Nano Letters* **10**, 1271–1275 (2010).
77. Barua, S., Dutta, H. S., Gogoi, S., Devi, R. & Khan, R. Nanostructured MoS_2-based advanced biosensors: a review. *ACS Applied Nano Materials* **1**, 2–25 (2018).
78. Syu, Y.-C., Hsu, W.-E. & Lin, C.-T. Review - field-effect transistor biosensing: devices and clinical applications. *ECS Journal of Solid State Science and Technology* **7**, Q3196–Q3207 (2018).
79. Radisavljevic, B., Radenovic, A., Brivio, J., Giacometti, V. & Kis, A. Single-layer MoS_2 transistors. *Nature Nanotechnology* **6**, 147–150 (2011).
80. Lopez-Sanchez, O., Lembke, D., Kayci, M., Radenovic, A. & Kis, A. Ultrasensitive photodetectors based on monolayer MoS_2. *Nature Nanotechnology* **8**, 497–501 (2013).
81. Sundaram, R. S. *et al.* Electroluminescence in single layer MoS_2. *Nano Letters* **13**, 1416–1421 (2013).
82. Manzeli, S., Ovchinnikov, D., Pasquier, D., Yazyev, O. v. & Kis, A. 2D transition metal dichalcogenides. *Nature Reviews Materials* **2**, 17033 (2017).
83. Choi, W. *et al.* Recent development of two-dimensional transition metal dichalcogenides and their applications. *Materials Today* **20**, 116–130 (2017).
84. Liu, K.-K. *et al.* Growth of large-area and highly crystalline MoS_2 thin layers on insulating substrates. *Nano Letters* **12**, 1538–1544 (2012).
85. Hong, J. *et al.* Exploring atomic defects in molybdenum disulphide monolayers. *Nature Communications* **6**, 6293 (2015).
86. Zhou, W. *et al.* Intrinsic structural defects in monolayer molybdenum disulfide. *Nano Letters* **13**, 2615–2622 (2013).
87. Komsa, H. P. & Krasheninnikov, A. V. Native defects in bulk and monolayer MoS_2 from first principles. *Physical Review B - Condensed Matter and Materials Physics* **91**, 125304 (2015).

88. Tan, A. M. Z., Freysoldt, C. & Hennig, R. G. Stability of charged sulfur vacancies in 2D and bulk MoS_2 from plane-wave density functional theory with electrostatic corrections. *Physical Review Materials* **4**, 64004 (2020).
89. Born, M. & Oppenheimer, R. Zur quantentheorie der molekeln. *Annals of Physics* **389**, 457–484 (1927).
90. Hartree, D. R. The wave mechanics of an atom with a non-Coulomb central field. Part I. theory and methods. *Mathematical Proceedings of the Cambridge Philosophical Society* **24**, 89–110 (1928).
91. Fock, V. Näherungsmethode zur lösung des quantenmechanischen mehrkörperproblems. *Zeitschrift für Physik* **61**, 126–148 (1930).
92. Sholl, D. S. & Steckel, J. A. *Density functional theory*. (John Wiley & Sons, Inc., 2009).
93. Møller, Chr. & Plesset, M. S. Note on an approximation treatment for many-electron systems. *Physical Review* **46**, 618–622 (1934).
94. Matczak, P. & Wojtulewski, S. Performance of Møller-Plesset second-order perturbation theory and density functional theory in predicting the interaction between stannylenes and aromatic molecules. *Journal of Molecular Modeling* **21**, 41 (2015).
95. Hohenberg, P. & Kohn, W. Inhomogeneous electron gas. *Physical Review* **136**, B864–B871 (1964).
96. Kohn, W. & Sham, L. J. Self-consistent equations including exchange and correlation effects. *Physical Review* **140**, A1133–A1138 (1965).
97. Perdew, J. P., Burke, K. & Wang, Y. Generalized gradient approximation for the exchange-correlation hole of a many-electron system. *Physical Review B* **54**, 16533–16539 (1996).
98. Martin, R. M. *Electronic structure*. (Cambridge University Press, 2004).
99. Perdew, J. P., Burke, K. & Ernzerhof, M. Generalized gradient approximation made simple. *Physical Review Letters* **77**, 3865–3868 (1996).
100. Neumann, M. A. & Perrin, M.-A. Energy ranking of molecular crystals using density functional theory calculations and an empirical van der Waals correction. *The Journal of Physical Chemistry B* **109**, 15531–15541 (2005).
101. Grimme, S. Accurate description of van der Waals complexes by density functional theory including empirical corrections. *Journal of Computational Chemistry* **25**, 1463–1473 (2004).
102. Grimme, S., Antony, J., Ehrlich, S. & Krieg, H. A consistent and accurate *ab initio* parametrization of density functional dispersion correction (DFT-D) for the 94 elements H-Pu. *The Journal of Chemical Physics* **132**, 154104 (2010).
103. Grimme, S. Semiempirical GGA-type density functional constructed with a long-range dispersion correction. *Journal of Computational Chemistry* **27**, 1787–1799 (2006).
104. Tran, F., Kalantari, L., Traoré, B., Rocquefelte, X. & Blaha, P. Nonlocal van der Waals functionals for solids: choosing an appropriate one. *Physical Review Materials* **3**, 063602 (2019).
105. Klimeš, J., Bowler, D. R. & Michaelides, A. van der Waals density functionals applied to solids. *Physical Review B* **83**, 195131 (2011).
106. Hamada, I. van der Waals density functional made accurate. *Physical Review B - Condensed Matter and Materials Physics* **89**, 121003 (2014).
107. Bagayoko, D. Understanding density functional theory (DFT) and completing it in practice. *AIP Advances* **4**, 127104 (2014).
108. Heyd, J., Peralta, J. E., Scuseria, G. E. & Martin, R. L. Energy band gaps and lattice parameters evaluated with the Heyd-Scuseria-Ernzerhof screened hybrid functional. *The Journal of Chemical Physics* **123**, 174101 (2005).
109. Heyd, J., Scuseria, G. E. & Ernzerhof, M. Hybrid functionals based on a screened Coulomb potential. *The Journal of Chemical Physics* **118**, 8207–8215 (2003).
110. Kresse, G. & Furthmüller, J. Efficient iterative schemes for ab initio total-energy calculations using a plane-wave basis set. *Physical Review B - Condensed Matter and Materials Physics* **54**, 11169–11186 (1996).

111. Henkelman, G., Uberuaga, B. P. & Jónsson, H. Climbing image nudged elastic band method for finding saddle points and minimum energy paths. *Journal of Chemical Physics* **113**, 9901–9904 (2000).
112. Su, R., Zhang, H., Meng, X., Shi, L. & Liu, C. Synthesis of Cr_2AlC thin films by reactive magnetron sputtering. *Fusion Engineering and Design* **125**, 562–566 (2017).
113. Lu, X., Li, S., Zhang, W., Yu, W. & Zhou, Y. Thermal shock behavior of a nanolaminated ternary boride: MoAlB. *Ceramics International* **45**, 9386–9389 (2019).
114. Liu, J. *et al.* Thermal stability and thermal shock resistance of Fe_2AlB_2. *Ceramics International* **44**, 16035–16039 (2018).
115. Barsoum, M. W. Oxidation of $Ti_{n+1}AlX_n$ (n = 1-3 and X = C, N). *Journal of The Electrochemical Society* **148**, C544 (2001).
116. Clark, D. W., Zinkle, S. J., Patel, M. K. & Parish, C. M. High temperature ion irradiation effects in MAX phase ceramics. *Acta Materialia* **105**, 130–146 (2016).
117. Wang, J., Liu, B., Wang, J. & Zhou, Y. Theoretical investigation of thermodynamic stability and mobility of the intrinsic point defects in Ti_3AC_2 (A = Si, Al). *Physical Chemistry Chemical Physics* **17**, 8927–8934 (2015).
118. Zhao, S., Xue, J., Wang, Y. & Huang, Q. Ab initio study of irradiation tolerance for different $M_{n+1}AX_n$ phases: Ti_3SiC_2 and Ti_3AlC_2. *Journal of Applied Physics* **115**, 023503 (2014).
119. Su, R., Zhang, H., Shi, L. & Wen, H. Formation of nanostructures in Ti_2AlC induced by high-temperature helium irradiation. *Journal of the European Ceramic Society* **39**, 1993–2002 (2019).
120. Li, N. *et al.* Rapid synthesis, electrical, and mechanical properties of polycrystalline Fe_2AlB_2 bulk from elemental powders. *Journal of the American Ceramic Society* **100**, 4407–4411 (2017).
121. Windsor, C. G. *et al.* Design of cemented tungsten carbide and boride-containing shields for a fusion power plant. *Nuclear Fusion* **58**, 7 (2018).
122. Murthy, T. S. R. C., Sonber, J. K., Sairam, K., Bedse, R. D. & Chakarvartty, J. K. Development of refractory and rare earth metal borides & carbides for high temperature applications. *Materials Today: Proceedings* **3**, 3104–3113 (2016).
123. Larionov, A. S., Chekushina, L. V. & Suslov, E. E. Development and investigation of high-strength neutron-absorbing composite coatings based on borides of metals. *Materials Science Forum* **945 MSF**, 660–664 (2018).
124. Su, R. *et al.* Deposition and characterization of Ti_2AlC MAX phase and Ti_3AlC thin films by magnetron sputtering. *Materials Letters* **179**, 194–197 (2016).
125. Stoller, R. E. *et al.* On the use of SRIM for computing radiation damage exposure. *Nuclear Instruments and Methods in Physics Research, Section B: Beam Interactions with Materials and Atoms* **310**, 75–80 (2013).
126. Luo, H. *et al.* Plasticity without dislocations in a polycrystalline intermetallic. *Nature Communications* **10**, 1–8 (2019).
127. Joubert, D. From ultrasoft pseudopotentials to the projector augmented-wave method. *Physical Review B - Condensed Matter and Materials Physics* **59**, 1758–1775 (1999).
128. Monkhorst, H. J. & Pack, J. D. Special points for Brillouin-zone integrations. *Physical Review B* **13**, 5188–5192 (1976).
129. Qi, Q. *et al.* Damage accumulation and recovery in C+-irradiated Ti_3SiC_2. *Acta Materialia* **66**, 317–325 (2014).
130. Tallman, D. J. *et al.* Effect of neutron irradiation on defect evolution in Ti_3SiC_2 and Ti_2AlC. *Journal of Nuclear Materials* **468**, 194–206 (2016).
131. Zhang, H., Su, R., Shi, L., O'Connor, D. J. & Wen, H. Structural changes of Ti_3SiC_2 induced by helium irradiation with different doses. *Applied Surface Science* **434**, 1210–1216 (2018).
132. Liu, J. *et al.* Rapid synthesis and characterization of a nanolaminated Fe_2AlB_2 compound. *Journal of Alloys and Compounds* **766**, 488–497 (2018).
133. Xi, J., Liu, B., Zhang, Y. & Weber, W. J. Ab initio study of point defects near stacking faults in 3C-SiC. *Computational Materials Science* **123**, 131–138 (2016).

134. Cheremisin, S. M., Dudkin, A. Y. & Matveev, I. V. Temperature-dependent amorphization of iron boride Fe_3B under neutron irradiation. *Nuclear Instruments and Methods in Physics Research* **84**, 102–104 (1994).
135. Krainy, A. G., Ogorodnikov, V. V., Grinik, E. U., Chirko, L. I. & Shinakov, A. A. Swelling and fracturing of borides under neutron irradiation. *Specialist Meeting on Erosion and Corrosion of Nuclear Power Plant Materials* **28**, 3 (1994).
136. Swaminathan, N., Morgan, D. & Szlufarska, I. Role of recombination kinetics and grain size in radiation-induced amorphization. *Physical Review B - Condensed Matter and Materials Physics* **86**, 214110 (2012).
137. Xu, D. & Wirth, B. D. Spatially dependent rate theory modeling of thermal desorption spectrometry of helium-implanted iron. *Fusion Science and Technology* **56**, 1064–1068 (2009).
138. Xu, D., Wirth, B. D., Li, M. & Kirk, M. A. Combining in situ transmission electron microscopy irradiation experiments with cluster dynamics modeling to study nanoscale defect agglomeration in structural metals. *Acta Materialia* **60**, 4286–4302 (2012).
139. Katoh, Y., Snead, L. L., Szlufarska, I. & Weber, W. J. Radiation effects in SiC for nuclear structural applications. *Current Opinion in Solid State and Materials Science* **16**, 143–152 (2012).
140. Wang, C. *et al.* Irradiation-induced structural transitions in Ti_2AlC. *Acta Materialia* **98**, 197–205 (2015).
141. Zhang, H. *et al.* The damage evolution of He irradiation on Ti_3SiC_2 as a function of annealing temperature. *Journal of the European Ceramic Society* **38**, 1253–1264 (2018).
142. Fahrenholtz, W. G. & Hilmas, G. E. Ultra-high temperature ceramics: materials for extreme environments. *Scripta Materialia* **129**, 94–99 (2017).
143. Zhang, H., Xiang, H., Dai, F. Z., Zhang, Z. & Zhou, Y. Oxidation behavior and thermal stability of Cr_2AlB_2 powders. *Corrosion Science* **176**, 108941 (2020).
144. Zhang, H. *et al.* Defect behavior and radiation tolerance of MAB phases (MoAlB and Fe_2AlB_2) with comparison to MAX phases. *Acta Materialia* **196**, 505–515 (2020).
145. Alameda, L. T., Moradifar, P., Metzger, Z. P., Alem, N. & Schaak, R. E. Topochemical deintercalation of Al from MoAlB: stepwise etching pathway, layered intergrowth structures, and two-dimensional MBene. *Journal of the American Chemical Society* **140**, 8833–8840 (2018).
146. Jung, D. H. et al. Metalline of semiconductor device having a diffuson barrier including Cr_xB_y and method for forming the same. *United States Patent* **US 7875979** (2011).
147. Kluge, M. & Schober, H. R. Isotope effect of diffusion in a simple liquid. *Physical Review E - Statistical Physics, Plasmas, Fluids, and Related Interdisciplinary Topics* **62**, 597–600 (2000).
148. Kota, S. *et al.* Magnetic properties of Cr_2AlB_2, Cr_3AlB_4, and CrB powders. *Journal of Alloys and Compounds* **767**, 474–482 (2018).
149. M.W. Chase Jr. NIST-JANAF themochemical tables, fourth edition. *Journal of Physical and Chemical Reference Data* (1998).
150. Van De Walle, C. G. & Neugebauer, J. First-principles calculations for defects and impurities: applications to III-nitrides. *Journal of Applied Physics* **95**, 3851–3879 (2004).
151. Xu, H. *et al.* Stability of intrinsic defects and defect clusters in $LiNbO_3$ from density functional theory calculations. *Physical Review B - Condensed Matter and Materials Physics* **78**, 174103 (2008).
152. Kohan, A., Ceder, G., Morgan, D. & Van de Walle, C. G. First-principles study of native point defects in ZnO. *Physical Review B - Condensed Matter and Materials Physics* **61**, 15019–15027 (2000).
153. Xi, J., Xu, H., Zhang, Y. & Weber, W. J. Strain effects on oxygen vacancy energetics in $KTaO_3$. *Physical Chemistry Chemical Physics* **19**, 6264–6273 (2017).
154. Zhang, F. X. *et al.* Local structure and defects in ion irradiated $KTaO_3$. *Journal of Physics Condensed Matter* **30**, 145401 (2018).
155. Togo, A. & Tanaka, I. First principles phonon calculations in materials science. *Scripta Materialia* **108**, 1–5 (2015).

156. Grieshammer, S. & Martin, M. Entropies of defect association in ceria from first principles. *Physical Chemistry Chemical Physics* **19**, 29625–29628 (2017).
157. Ágoston, P. & Albe, K. Formation entropies of intrinsic point defects in cubic In_2O_3 from first-principles density functional theory calculations. *Physical Chemistry Chemical Physics* **11**, 3226–3232 (2009).
158. Okada, S., Atoda, T. & Higashi, I. Structural investigation of Cr_2B_3, Cr_3B_4, and CrB by single-crystal diffractometry. *Journal of Solid State Chemistry* **68**, 61–67 (1987).
159. Zhang, H., Su, R., Szlufarska, I., Shi, L. & Wen, H. Helium effects and bubbles formation in irradiated Ti_3SiC_2. *Journal of the European Ceramic Society* **41**, 252–258 (2021).
160. Li, S. *et al.* Pushing the limit of thermal conductivity of MAX borides and MAB. *Journal of Materials Science & Technology* **97**, 79–88 (2022).
161. Kota, S. *et al.* Synthesis and characterization of an alumina forming nanolaminated boride: MoAlB. *Scientific Reports* **6**, 26475 (2016).
162. Shen, C. *et al.* Designing of magnetic MAB phases for energy applications. *Journal of Materials Chemistry A* **9**, 8805–8813 (2021).
163. Rosli, N. F. *et al.* MAX and MAB Phases: two-dimensional layered carbide and boride nanomaterials for electrochemical applications. *ACS Applied Nano Materials* **2**, 9, 6010–6021 (2019).
164. Wang, X. *et al.* Radiation-induced segregation in a ceramic. *Nature Materials* **19**, 992–998 (2020).
165. Zhang, H. *et al.* Enhancing the phase stability of ceramics under radiation via multilayer engineering. *Science Advances* **7**, eabg7678 (2021).
166. L'vov, S. N., Nemchenko, V. F., Kislyi, P. S., Verkhoglyadova, T. S. & Kosolapova, T. Ya. The electrical properties of chromium borides, carbides, and nitrides. *Soviet Powder Metallurgy and Metal Ceramics 1964 1:4* **1**, 243–247 (1962).
167. Kislyi, P. S., L'vov, S. N., Nemchenko, V. F. & Samsonov, G. V. Physical properties of the boride phases of chromium. *Soviet Powder Metallurgy and Metal Ceramics 1964 1:6* **1**, 441–443 (1962).
168. Luo, H., Zhang, H., Sheng, H., Liu, J. P. & Szlufarska, I. Amorphous shear bands in $SmCo_5$. *Materials Science and Engineering A* **785**, 21 (2020).
169. Su, R., Zhang, H., Liu, L., Shi, L. & Wen, H. Reversible phase transformation in Ti_2AlC films during He radiation and subsequent annealing. *Journal of the European Ceramic Society* **41**, 6309–6318 (2021).
170. Zheng, M. J., Swaminathan, N., Morgan, D. & Szlufarska, I. Energy barriers for point-defect reactions in 3C-SiC. *Physical Review B - Condensed Matter and Materials Physics* **88**, 054105 (2013).
171. Lundström, T. Transition metal borides. In: Matkovich, V. I. *Boron and refractory borides*. (Springer, Berlin, 1977).
172. Opeka, M. M., Talmy, I. G. & Zaykoski, J. A. Oxidation-based materials selection for 2000 °C + hypersonic aerosurfaces: theoretical considerations and historical experience. *Journal of Materials Science* **39**, 5887–5904 (2004).
173. Lonergan, J. M., Fahrenholtz, W. G. & Hilmas, G. E. Zirconium diboride with high thermal conductivity. *Journal of the American Ceramic Society* **97**, 1689–1691 (2014).
174. Neuman, E. W., Hilmas, G. E. & Fahrenholtz, W. G. Strength of zirconium diboride to 2300 °C. *Journal of the American Ceramic Society* **96**, 47–50 (2013).
175. Wang, B., Li, X., Wang, Y. X. & Tu, Y. F. Phase stability and physical properties of manganese borides: a first-principles study. *Journal of Physical Chemistry C* **115**, 21429–21435 (2011).
176. Miao, N., Sa, B., Zhou, J. & Sun, Z. Theoretical investigation on the transition-metal borides with Ta_3B_4-type structure: a class of hard and refractory materials. *Computational Materials Science* **50**, 1559–1566 (2011).
177. Das, S., Chen, H. Y., Penumatcha, A. V. & Appenzeller, J. High performance multilayer MoS_2 transistors with scandium contacts. *Nano Letters* **13**, 100–105 (2013).

178. Lee, G. H. *et al.* Flexible and transparent MoS_2 field-effect transistors on hexagonal boron nitride-graphene heterostructures. *ACS Nano* **7**, 7931–7936 (2013).
179. Geim, A. K. & Grigorieva, I. V. van der Waals heterostructures. *Nature* **499**, 419–425 (2013).
180. Li, M. Y., Chen, C. H., Shi, Y. & Li, L. J. Heterostructures based on two-dimensional layered materials and their potential applications. *Materials Today* **19**, 322–335 (2016).
181. Velický, M. & Toth, P. S. From two-dimensional materials to their heterostructures: an electrochemist's perspective. *Applied Materials Today* **8**, 68–103 (2017).
182. Guo, Y., Liu, D. & Robertson, J. Chalcogen vacancies in monolayer transition metal dichalcogenides and Fermi level pinning at contacts. *Applied Physics Letters* **106**, 173106 (2015).
183. Liu, D., Guo, Y., Fang, L. & Robertson, J. Sulfur vacancies in monolayer MoS_2 and its electrical contacts. *Applied Physics Letters* **103**, 183113 (2013).
184. McDonnell, S., Addou, R., Buie, C., Wallace, R. M. & Hinkle, C. L. Defect-dominated doping and contact resistance in MoS_2. *ACS Nano* **8**, 2880–2888 (2014).
185. Qiu, H. *et al.* Hopping transport through defect-induced localized states in molybdenum disulphide. *Nature Communications* **4**, 1–6 (2013).
186. Lu, C. P., Li, G., Mao, J., Wang, L. M. & Andrei, E. Y. Bandgap, mid-gap states, and gating effects in MoS_2. *Nano Letters* **14**, 4628–4633 (2014).
187. Vancsó, P. *et al.* The intrinsic defect structure of exfoliated MoS_2 single layers revealed by scanning tunneling microscopy. *Scientific Reports* **6**, 1–7 (2016).
188. Barja, S. *et al.* Identifying substitutional oxygen as a prolific point defect in monolayer transition metal dichalcogenides. *Nature Communications* **10**, 1–8 (2019).
189. Wu, Z. & Ni, Z. Spectroscopic investigation of defects in two-dimensional materials. *Nanophotonics* **6**, 1219–1237 (2017).
190. Tongay, S. *et al.* Defects activated photoluminescence in two-dimensional semiconductors: interplay between bound, charged, and free excitons. *Scientific Reports* **3**, 2657 (2013).
191. Wu, Z. *et al.* Defect activated photoluminescence in WSe_2 monolayer. *Journal of Physical Chemistry C* **121**, 12294–12299 (2017).
192. Chow, P. K. *et al.* Defect-induced photoluminescence in monolayer semiconducting transition metal dichalcogenides. *ACS Nano* **9**, 1520–1527 (2015).
193. McCreary, A. *et al.* Distinct photoluminescence and Raman spectroscopy signatures for identifying highly crystalline WS_2 monolayers produced by different growth methods. *Journal of Materials Research* **31**, 931–944 (2016).
194. Kwak, J. Y. *et al.* Electrical characteristics of multilayer MoS_2 FETs with MoS_2/graphene heterojunction contacts. *Nano Letters* **14**, 4511–4516 (2014).
195. Gelczuk, Ł. *et al.* Probing defects in MoS_2 van der Waals crystal through deep-level transient spectroscopy. *Physica Status Solidi - Rapid Research Letters* **14**, 12 (2020).
196. Ci, P. *et al.* Chemical trends of deep levels in van der Waals semiconductors. *Nature Communications* **11**, 5373 (2020).
197. Noh, J.-Y., Kim, H. & Kim, Y.-S. Stability and electronic structures of native defects in single-layer MoS_2. *Physical Review B* **89**, 205417 (2014).
198. Freysoldt, C., Neugebauer, J. & Van De Walle, C. G. Fully ab initio finite-size corrections for charged-defect supercell calculations. *Physical Review Letters* **102**, 016402 (2009).
199. Freysoldt, C., Neugebauer, J. & Van de Walle, C. G. Electrostatic interactions between charged defects in supercells. *Physica Status Solidi (B) Basic Research* **248**, 1067–1076 (2011).
200. Allain, A., Kang, J., Banerjee, K. & Kis, A. Electrical contacts to two-dimensional semiconductors. *Nature Materials* **14**, 1195–1205 (2015).
201. Lang, D. V. Deep-level transient spectroscopy: a new method to characterize traps in semiconductors. *Journal of Applied Physics* **45**, 3023–3032 (1974).
202. Blood, P. & Orton, J. W. *The electrical characterization of semiconductors: majority carriers and electron states*. (Academic Press, London, 1992).

203. Peng, H., Yang, Z. H., Perdew, J. P. & Sun, J. Versatile van der Waals density functional based on a meta-generalized gradient approximation. *Physical Review X* **6**, 041005 (2016).
204. Peng, H. & Perdew, J. P. Rehabilitation of the Perdew-Burke-Ernzerhof generalized gradient approximation for layered materials. *Physical Review B* **95**, 081105 (2017).
205. Terentjev, A. V., Constantin, L. A. & Pitarke, J. M. Dispersion-corrected PBEsol exchange-correlation functional. *Physical Review B* **98**, 214108 (2018).
206. Klimeš, J., Bowler, D. R. & Michaelides, A. Chemical accuracy for the van der Waals density functional. *Journal of Physics Condensed Matter* **22**, 022201 (2010).
207. Berland, K. & Hyldgaard, P. Exchange functional that tests the robustness of the plasmon description of the van der Waals density functional. *Physical Review B - Condensed Matter and Materials Physics* **89**, 035412 (2014).
208. Alkauskas, A., Broqvist, P. & Pasquarello, A. Defect energy levels in density functional calculations: alignment and band gap problem. *Physical Review Letters* **101**, 046405 (2008).
209. Maciej P. Polak, Robert Kudrawiec, Ryan Jacobs, Izabela Szlufarska, D. M. Modified band alignment method to obtain hybrid functional accuracy from standard DFT: application to defects in highly mismatched III-V:Bi alloys. *Physical Review Materials* **5**, 124601 (2021).
210. Wakabayashi, N., Smith, H. G. & Nicklow, R. M. Lattice dynamics of hexagonal MoS_2 studied by neutron scattering. *Physical Review B* **12**, 659–663 (1975).
211. Schutte, W. J., De Boer, J. L. & Jellinek, F. Crystal structures of tungsten disulfide and diselenide. *Journal of Solid State Chemistry* **70**, 207–209 (1987).
212. James, P. B. & Lavik, M. T. The crystal structure of $MoSe_2$. *Acta Crystallographica* **16**, 1183–1183 (1963).
213. Puotinen, D. & Newnham, R. E. The crystal structure of $MoTe_2$. *Acta Crystallographica* **14**, 691–692 (1961).
214. Dawson, W. G. & Bullett, D. W. Electronic structure and crystallography of $MoTe_2$ and WTe_2. *Journal of Physics C: Solid State Physics* **20**, 6159–6174 (1987).
215. Li, S. *et al.* Synthesis of semiconducting 2H-phase WTe_2 nanosheets with large positive magnetoresistance. *Inorganic Chemistry* **59**, 11935–11939 (2020).
216. Kam, K. K. & Parkinson, B. A. Detailed photocurrent spectroscopy of the semiconducting group VIB transition metal dichalcogenides. *The Journal of Physical Chemistry* **86**, 463–467 (1982).
217. Böker, T. *et al.* Band structure of MoS_2, $MoSe_2$, and α−$MoTe_2$: angle-resolved photoelectron spectroscopy and ab initio calculations. *Physical Review B - Condensed Matter and Materials Physics* **64**, 235305 (2001).
218. Komsa, H. P., Rantala, T. T. & Pasquarello, A. Finite-size supercell correction schemes for charged defect calculations. *Physical Review B - Condensed Matter and Materials Physics* **86**, 045112 (2012).
219. Li, P. *et al.* Evidence for topological type-II Weyl semimetal WTe_2. *Nature Communications* **8**, 2150 (2017).
220. Jin, C. *et al.* On optical dipole moment and radiative recombination lifetime of excitons in WSe_2. *Advanced Functional Materials* **27**, 1601741 (2017).
221. Kim, J. *et al.* Observation of ultralong valley lifetime in WSe_2/MoS_2 heterostructures. *Science Advances* **3**, 1700518 (2017).
222. Qin, M., Yan, Q., Liu, Y. & Luo, J. A new class of high-entropy M_3B_4 borides. *Journal of Advanced Ceramics* **10**, 166–172 (2021).
223. Gild, J. *et al.* High-entropy metal diborides: a new class of high-entropy materials and a new type of ultra-high temperature ceramics. *Scientific Reports* **6**, 37946 (2016).

VITA

Jun Young Kim was born and raised in Bucheon, Republic of Korea, and he attended Kyung Hee University, Seoul, to study physics for his bachelor's degree. After graduating in 2012, he worked as a student researcher specializing in nanophotonics at the Korea Institute of Science and Technology, Seoul, while studying for his master's degree at Kyung Hee University. From 2014 to 2017, he fulfilled his military service as a Republic of Korea Army officer at the Korea Military Academy, Seoul, where he was appointed as an assistant professor and taught physics to cadets. In September 2017, he joined the Electrical and Computer Engineering program at the University of Wisconsin–Madison. He studied semiconductor physics under Prof. Robert M. Farrell (2017-2019) and studied computational materials science under Prof. Izabela A. Szlufarska (2019-2022). Jun Young Kim received the degree of Doctor of Philosophy in May 2022.